RICE UNIVERSITY

Novel Spin-orbit Coupling in Cold Atoms

by

Chuanzhou Zhu

A Thesis Submitted
in Partial Fulfillment of the
Requirements for the Degree

Doctor of Philosophy

Approved, Thesis Committee:

Dr. Han Pu, Chair
Professor of Physics and Astronomy

Dr. Randall G. Hulet
Fayez Sarofim Professor of Physics

Dr. Fenglin Niu
Professor of Earth Science

Houston, Texas

January, 2020

ABSTRACT

Novel Spin-orbit Coupling in Cold Atoms

by

Chuanzhou Zhu

In cold atom, the coupling between "spin" (atomic internal hyperfine states) and "orbit" (atomic center-of-mass motion) can be induced by Raman transition, where different hyperfine states are coupled by a pair of Raman lasers. In recent years, this synthetic spin-orbit coupling has received tremendous attention, as it leads to a variety of novel quantum phenomena in precisely controllable cold atom systems.

In this thesis, we first present a comprehensive analysis of one-, two- and many-particle physics of harmonically trapped atoms with spin-orbit coupling, followed by the study of "novel spin-orbit coupling" in two different systems: (1) cold atom spinor mixtures and (2) cold atoms in an optical cavity. In the first system, we consider a spinor mixture consisting of two species of cold atoms, where the spin-orbit coupling can be transmitted from one species to the other, and we discuss novel topological properties and the supersolid stripe phase in this mixture. In the second system, we consider the coupling among three parts: the cavity photon field, the atomic internal hyperfine states, and the atomic external center-of-mass motion, and we discuss how this coupling affects familiar quantum optical phenomena, such as Rabi oscillation and Dicke superradiance phase transition. Our novel systems contribute new and practical platforms for the research field of synthetic spin-orbit coupling in cold atoms.

Publications

I hereby declare that except where specific reference is made to the work of others, the contents of this thesis are original and have not been submitted in whole or in part for consideration for any other degree or qualification in this, or any other university.

The following journal publications are (co-)authored and extensively reproduced by the Ph.D. candidate, **Chuanzhou Zhu**, in this dissertation:

[1] **Chuanzhou Zhu**, Li Chen, Hui Hu, Xia-ji Liu, and Han Pu,
"Spin-exchange-induced exotic superfluids in a Bose-Fermi spinor mixture",
Physical Review A, **100** 031602(R), (2019).

[2] Li Chen, **Chuanzhou Zhu**, Yunbo Zhang, and Han Pu,
"Spin-exchange-induced spin-orbit coupling in a superfluid mixture",
Physical Review A, **97** 031601(R), (2018).

[3] **Chuanzhou Zhu**, Lin Dong, and Han Pu,
"Dynamical Spin-Orbit Coupling in Cold Atoms Induced by Cavity Field",
Chapter **7** in the Book "Synthetic Spin-Orbit Coupling in Cold Atoms" (2018).

[4] **Chuanzhou Zhu**, Lin Dong, and Han Pu,
"Effects of spin-orbit coupling on Jaynes-Cummings and Tavis-Cummings models",
Physical Review A, **94** 053621, (2016).

[5] **Chuanzhou Zhu**, Lin Dong, and Han Pu,
"Harmonically trapped atoms with spin-orbit coupling",
Journal of Physics B: Atomic, Molecular and Optical Physics, **49** 145301, (2016).

[6] Lin Dong, **Chuanzhou Zhu**, and Han Pu,
"Photon-Induced Spin-Orbit Coupling in Ultracold Atoms inside Optical Cavity",
Atoms, **3**, 2, pp. 182194, (2015).

This work is dedicated to my wife Yingzhe Zhang, for her hard work with baby delievery and bring us a new life to enrich our family.

Acknowledgments

First and foremost, I would like to thank my adviser, Dr. Han Pu, for leading me into a variety of fantastic research projects in the field of cold-atom and quantum-optical physics, guiding me step by step to complete whole projects, and encouraging me to find a postdoc job in the frontier of Physics. Every time I lost my direction in research, he can always smartly point me out a correct solution and keep me going.

I would like to thank my closest peer collaborators, Dr. Li Chen, Dr. Lin Dong, and Dr. Shuwei Song, for their enlightening ideas and hard working in our collaborations, and their long-term beneficial discussions with me. I would also like to thank all the other current, previous, and visiting members in our group, including Li Yang, Youjiang Xu, Shah Saad Alam, Sagarika Basak, Ramachandhran Balasubramanian, Wen wen, and Liming Guan, for their firm supports to my research.

I would like to thank Dr. Randy Hulet for thoroughly reading this thesis and providing detailed advices, and kindly instructing me during my annual committee report in each year. In addition, I would like to thank Dr. Randy Hulet, Dr. Fenglin Niu, and Dr. Peter Nordlander for being my committee members.

I would like to thank our graduate coordinator Rosa Almendarez for her firm support to my academic career at Rice. I would like to thank all my family members for their firm support to my completion of the PhD program.

Contents

Illustrations

Chapter 1

Introduction and Outline

1.1 Introduction

Spin-orbit (SO) coupling in quantum physics is defined as the coupling between a particle's spin and its momentum. The intrinsic SO coupling of an electron is resulted from the relativistic Dirac equation, and it gives rise to the atomic fine structure. In condensed matters, SO coupling of electron is a key for the quantum spin Hall effect [1] and topological insulators [2]. Although SO coupling is ubiquitous in a variety of physical systems, the SO coupling in cold atoms had not been experimentally realized until 10 years ago.

The SO coupling in cold atoms was first experimentally realized in 2010 by Dr. Spielman's group in University of Maryland, through coupling different atomic spin (hyperfine) states by a pair of Raman lasers in a ^{87}Rb atomic Bose-Einstein condensate [3]. After this initial experiment, SO coupling has been realized in both Bose-Einstein condensates and ultracold Fermi gases in several groups, and a variety of novel physical phenomena have been experimentally observed and theoretically predicted.

In SO coupled Bose-Einstein condensate (BEC) of ^{87}Rb, Dr. Spielman's group measured two degenerate energy minima and observed a mixed phase, where the condensate wave function can be a superposition of the two degenerate state [3]. This mixed phase was soon theoretically identified as the so-called "supersoild stripe phase", where the condensate density profile was predicted to show striped modulations in real space [4]. Recently, Dr. Ketterle's group in MIT observed the predicted density modulation of this stripe phase using Bragg reflection [5], and Dr. Engels's group in Washington State University realized a long-lived striped BEC through employing a weak optical lattice to induce momentum-space hopping between two spin-orbit band minima [6]. In addition, Dr. Pan's group in University of Science and Technology of China realized two-dimensional SO coupling for BEC, based on a optical Raman lattice scheme [7], and measured finite-temperature phase diagram [8].

The SO coupled ultracold Fermi gas was realized in 2012 in Dr. Zhang's group in Shanxi University with ^{40}K [9] and Dr. Zwierlein's group in MIT with ^{6}Li [10], and obeserved through momentum-resolved radio-frequency spectroscopy and spin-injection spectroscopy, respectively. In each of these experiments, an asymmetric, spinful, and gapped energy-momentum dispersion was measured and regarded as a hallmark of SO coupling for fermions. Recently, Dr. Lev's group in Stanford University experimentally created a long-lived SO coupled Fermi gas through using the most magnetic fermionic element ^{161}Dy, and measured SO-coupling modified Rabi oscillation [11]. In addition, Dr. Ye's group in University of Colorado Boulder made an optical lattice clock based on SO-coupled ^{87}Sr fermions [12].

The theory of SO coupling in cold atoms are nicely summarized in two review articles in refs. [13] and [14]. For SO coupled bosons, the phase diagram with the spatially modulated stripe phase is theoretically presented in ref. [4], through a simple variational theory in the mean-field approximation. For SO coupled fermions, the topological bands, topological superfluids, and Majorana edge states are theoretically predicted in ref. [15], based on Bogoliubov-de-Gennes formalism. The above theoretical articles, together with basic models in quantum optics textbooks [16] (i.e.

Jaynes-Cummings and Tavis-Cummings Models), form all the theoretical basis of this thesis.

One of the important reasons why SO coupling in cold atoms has received tremendous attention is that it provides a precisely controllable and clean platform to simulate the SO-coupling induced topological phenomena in condensed matter systems, which has been predicted in numerous theories but are difficult to observe in condensed matter experiments. The system of SO coupled cold atoms not only has unprecedented controllability of dimensionality, geometry, interaction strength, and statistics, etc., but also has minimal thermal noise from external environment. In addition, compare to the long-range Coulomb interactions in condensed matters, the controllable short-range Van Der Waals interactions in cold atoms greatly reduce the noise from particle-particle interactions and is beneficial for the observations of essential physical properties.

In this thesis, we go beyond this basic ”simulation purpose” and the previous theories in this research field. We explore the novel SO coupling in unique cold-atom mixtures and optical cavities, and hence our novel SO coupling is completely new and without any counter parts in condensed matter physics. Our novel spin-orbit coupling effects are induced by spin-exchange interactions in cold-atom mixtures and assisted by quantized photons in optical cavities.

1.2 Outline

In this Chapter, we first provide a brief introduction to the research field of spin-orbit coupling in cold atoms in Sec. 1.1, followed by an outline of the thesis in this Section.

In Chapter 2, we consider harmonically trapped atoms subjected to the spin-orbit coupling induced by Raman transition. In this Chapter, we first present the wave function and the degeneracy of the single-particle ground state, followed by a study of two weakly interacting bosons or fermions. For the two-particle ground state, we focus on the effects of the interaction on the degeneracy, the spin density profiles, and the density-density correlation functions. Furthermore, we show how the two-boson ground state helps us understand the many-body properties of the spin-orbit coupled Bose-Einstein condensate.

In Chapter 3, we discuss many-body properties of a dual-species mixture of spin-1/2 cold atoms, which can be either Bose-Fermi or Bose-Bose mixture. In such a mixture, we assume that only the first species of the atoms is subjected to the spin-orbit coupling induced by Raman laser beams, whereas the second species is not coupled to the Raman beams. We propose an efficient way to transmit the spin-orbit coupling from the first to the second species, and hence a promising way of obtaining spin-orbit coupled atoms without Raman-induced heating. In a Bose-Fermi mixture discussed in Sec. 3.1, we show that the long-sought topological Fermi superfluids and topological bands can be realized, and that the presence of fermions not only provides a new way to create the supersolid stripe phase of the bosons, but more strikingly it can also greatly increase the spatial period of the bosonic density stripes, and hence makes this phase directly observable in the experiment. In a Bose-Bose mixture discussed in Sec. 3.2, we present a very rich phase diagram, with many of the phases not present in a single-species condensate.

In Chapter 4, we consider cold atoms inside a ring optical cavity that supports a single plane-wave mode. The quantized cavity photon field, together with an external classical laser field, drives a two-photon Raman transition between two internal pseudo-spin (hyperfine) states of the atom. This scheme gives rise to the coupling among three degrees of freedom, which include the cavity photon field, the atomic internal pseudo-spin state, and the atomic external center-of-mass motion. We name such a coupling as ”cavity-assisted spin-orbit coupling”. In Sec. 4.1, we show how this spin-orbit coupling modifies the static and dynamic properties of the Jaynes-Cummings model, and the Dicke superradiance phase transition of the Tavis-Cummings Model. In Sec. 4.2, we consider the dissipative processes of the ring optical cavity, investigate the properties of this system by adopting a mean-field and a full quantum approach, and show that the interplay between the atomic dynamics and the cavity field gives rise to intriguing nonlinear phenomena.

Here, we would like to explicitly state that the author’s journal publications during his PhD period are reprinted in this thesis, where Chapter 2 is reprinted from Ref. [17], Chapter 3 is reprinted from Refs. [18,19], and Chapter 4 is reprinted from Refs. [20,21], except some minor add-ons, modifications and reorganizations.

Chapter 2

Harmonically Trapped Atoms with Spin-Orbit Coupling

For one-dimensional (1D) spin-orbit coupled systems in uniform space, the single-particle ground state [13] can be easily obtained, and the ground states of two-body [22, 23] and many-body [4] systems with zero-range contact interactions have been analytically calculated by scattering theory and by mean field approaches, respectively. Compared with investigating these systems in uniform space, it is more relevant and realistic to consider the systems in a harmonic trap, as a trapping potential is always present in cold atom experiment. This chapter introduces a systematic investigation of the harmonically trapped single-particle and two-particle ground states in 1D spin-orbit coupled systems, and discuss how they are related to the many-body physics.

In this chapter, we aim to present such a study. We systematically investigate the ground states of a single particle, two bosons, and two fermions confined in a 1D harmonic trap with Raman-induced spin-orbit coupling. For the single-particle ground state, which is presented in Sec. 2.1, we obtain the wave functions through imaginary time evolution and demonstrate how the Raman coupling strength and the trap frequency affect the degeneracy. In Sec. 2.2 we consider two weakly interacting bosons. The degeneracy, entanglement, density-density correlation functions, and spin density profiles of the ground state are studied by varying the spin-dependent contact interaction, Raman coupling strength, and two-photon detuning. Our results demonstrate that the spin-dependent interaction breaks the ground state degeneracy of this system, and also imprints a stripe pattern in the density-density correlation. In Sec. 2.2, we also discuss the connection between the behaviours of two-boson and many-boson ground states. In Sec. 2.4, we propose an experimental scheme to measure the energy gap between the ground state and the first excited state of the system through a resonance excitation process [24, 25]. To investigate the effect of quantum statistics, we then consider a system of two fermions in Sec. 2.3 and show how they differ from the system of two bosons.

Here, it needs to be explicitly stated that this Chapter is reprinted from Ref. [17], except some minor add-ons, modifications and reorganizations.

2.1 Single-particle Ground State

In this section, we consider a single spin-1/2 atom confined in a 1D harmonic trap with frequency ω, subjected to the Raman-induced spin-orbit coupling, with two-photon recoil momentum q_r, Raman coupling strength Ω, and two-photon detuning δ. The Hamiltonian then takes the form

$$h = \frac{\hat{p}^2}{2m} + \frac{1}{2}m\omega^2 x^2 + \frac{q_r \hat{p}}{m}\sigma_z + \frac{\Omega}{2}\sigma_x + \frac{\delta}{2}\sigma_z \,, \tag{2.1}$$

where σ_x and σ_z denote the x and z components of Pauli matrices, m is the atomic mass, $\hat{p} = -i\hbar\partial/\partial x$ is the momentum operator, and x is the position. The two spin states are defined as $\sigma_z|\uparrow\rangle = |\uparrow\rangle$ and $\sigma_z|\downarrow\rangle = -|\downarrow\rangle$, respectively. We mainly consider the case with $\delta = 0$, and the influence of finite δ will be briefly discussed.

We first briefly review the case when there is no trap [13], i.e., $\omega = 0$. For this case, the system possesses translational symmetry and thus the momentum p is a good quantum number. Figure 2.1 plots the single-particle energy dispersion for

$\delta = 0$, which is analytically give by

$$\epsilon_p = \frac{p^2}{2m} \pm \sqrt{\frac{q_r^2 p^2}{m^2} + \frac{\Omega^2}{4}}. \tag{2.2}$$

For $\Omega < 4E_r$ (where $E_r \equiv q_r^2/(2m)$ is the recoil energy), as shown in Fig. 2.1, ϵ_p displays two degenerate minima at $p = \pm k \equiv \pm q_r \sqrt{1 - (\Omega/4E_r)^2}$, corresponding to two orthogonal degenerate ground states

$$\langle x\sigma |\, g_1 \rangle = e^{ikx} \left[\cos\theta_k \quad -\sin\theta_k\right]^T, \tag{2.3}$$

$$\langle x\sigma |\, g_2 \rangle = e^{-ikx} \left[\sin\theta_k \quad -\cos\theta_k\right]^T, \tag{2.4}$$

where $\sigma = \uparrow (\downarrow)$ marks the spin up (down) state, and $\tan\theta_k = \frac{2}{\Omega}\left(\frac{q_r k}{m} + \sqrt{\frac{q_r^2 k^2}{m^2} + \frac{\Omega^2}{4}}\right)$. For $\Omega > 4E_r$, as shown in Fig. 2.1, the single particle dispersion has only a single minimum at $p = 0$ and the non-degenerate ground state takes the form

$$\langle x\sigma |\, g \rangle = \left[1/\sqrt{2} \quad -1/\sqrt{2}\right]^T. \tag{2.5}$$

The presence of a harmonic trap breaks the translational symmetry of the system, and we have to resort to numerical calculations to study the properties of the ground state. Using the finite difference method to discretize $\hat{p}$ and x, we obtain eigenenergies through the diagonalization of the single-particle Hamiltonian (2.1), and the ground-state wave function by imaginary time evolution. At $\delta = 0$, Hamiltonian (2.1) possesses the following symmetry: If $|\psi\rangle$ is an eigenstate of h, $|\psi'\rangle = \sigma_x K|\psi\rangle$, where K represents complex conjugate operator, is also an eigenstate with the same eigenenergy. However, unlike the time reversal symmetry of a spin-1/2 system which results in Kramer degeneracy, the current symmetry does not guarantee degenerate eigenstates. For a non-degenerate state $|\psi\rangle$, the above symmetry property necessarily requires $|\psi'\rangle = \sigma_x K|\psi\rangle$ to differ from $|\psi\rangle$ by at most an overall phase factor. In Fig. 2.2(a) we exhibit the low-lying energy spectrum for a trapped system with three

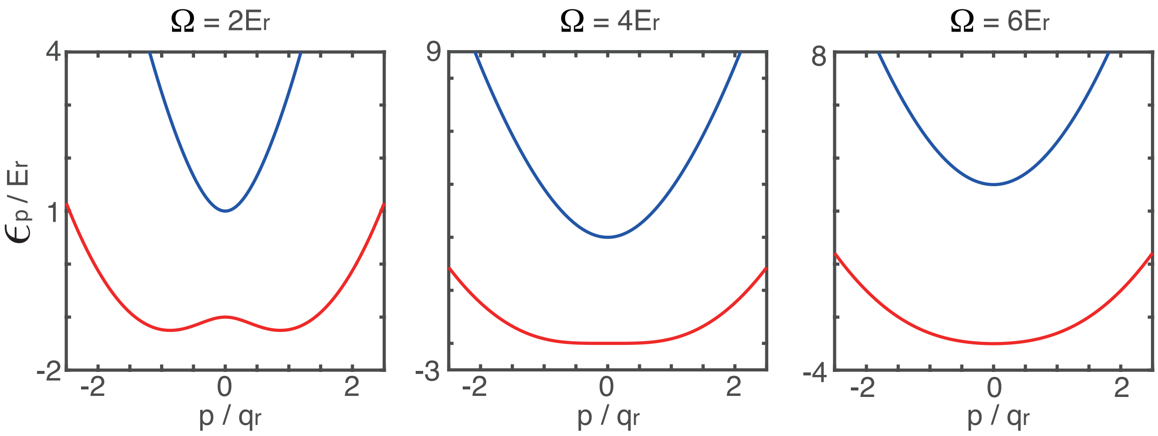

Figure 2.1 : Single-particle energy-momentum dispersions for different values of Ω in the homogeneous case with no trap, where the red and blue lines correspond to the dispersions with lower and higher energies, respectively.

different values of Raman coupling strength Ω. Each red (blue) dot represents the energy of a two-fold degenerate (non-degenerate) eigenstate. At $\Omega = 0$, we have two uncoupled spin states, and all the single-particle states must be trivially two-fold degenerate. As Ω increases, degeneracies of the high-energy states start to be lifted first. Eventually, at a critical coupling strength Ω_c, the degeneracy of the ground state is also lifted and all the single particle eigenstates become non-degenerate. The energy difference $\Delta\epsilon$ between the two lowest-lying states is shown in Fig. 2.2, as a function of Ω for various trap frequencies ω. For a fixed value of the trap frequency ω, with increasing Ω, $\Delta\epsilon$ changes from zero to finite when Ω exceeds Ω_c, signaling that the ground state changes from being two-fold degenerate to non-degenerate. The critical value Ω_c at which the ground state degeneracy is lifted is a decreasing function of the trap frequency ω, and in the limit $\omega \to 0$, $\Omega_c = 4E_r$ and we recover the result for the homogeneous system.

The degeneracy breaking of single-particle eigenstates at large Ω can be intuitively

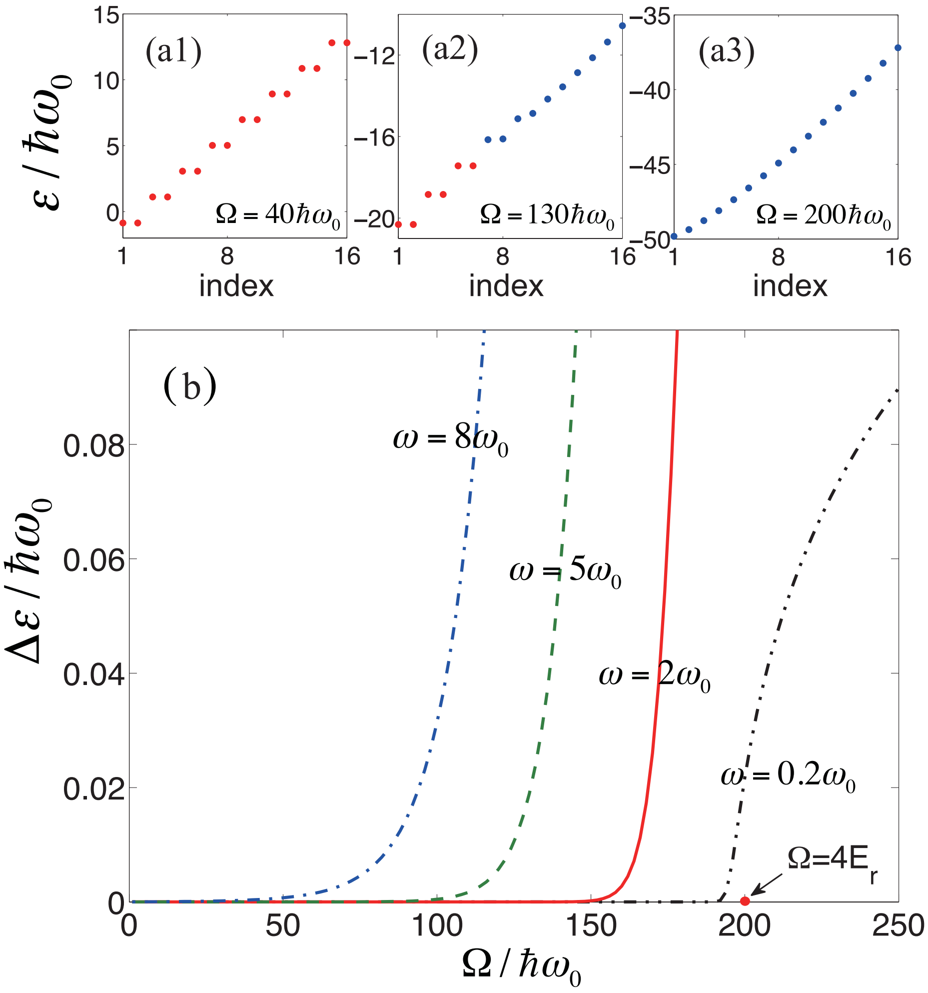

Figure 2.2 : (a$_1$)-(a$_3$) The first 16 single-particle eigenenergies with trap frequency $\omega = 2\omega_0$ for several different values of Raman coupling strength $\Omega/(\hbar\omega_0) = 40, 130, 200$. Red dots correspond to two-fold degenerate eigenstates and blue dots correspond to non-degenerate eigenstates. (b) Energy gap $\Delta\epsilon$ between the two lowest energy eigenstates as a function of Ω for different values of trap frequency. We consider $\delta = 0$ in this figure. Throughout this Chapter, we choose $\omega_0 = 2\pi \times 100\,\text{Hz}$ to be the unit for frequency and take m to be the mass of the ^{87}Rb atom. As typical values in experiments, we choose the recoil momentum $q_r = 10\sqrt{m\hbar\omega_0}$, and the trap frequency ω in the range of $0.1 \sim 10\,\omega_0$.

understood as follows. The Raman coupling term, $\Omega\sigma_x/2$, in the Hamiltonian (2.1) behaves like an effective Zeeman field in the x-direction. At large Ω, this effective Zeeman field is so strong that it polarizes the spin-1/2 particle by aligning its spin along the x-axis, and the particle essentially becomes a scalar particle as its spin degrees of freedom is frozen. It is a well known fact that, for a scalar particle, there is no degenerate bound state in 1D [26].

The two-component spinor wave function of a single particle can be written as $\begin{bmatrix} \phi_\uparrow(x) & \phi_\downarrow(x) \end{bmatrix}^T$, where $\phi_\sigma(x) = |\phi_\sigma(x)|\, e^{i\theta_\sigma(x)}$ is in general complex with phase angle $\theta_\sigma(x)$. In Fig. 2.3, we exhibit the ground state wave function for $\omega = 2\omega_0$ (which corresponds to the red solid line in Fig. 2.2(b)) and two different values of Ω.

When $\Omega = 130\hbar\omega_0$, the ground states are two-fold degenerate, and the two degenerate states are transformed to each other by the symmetry operation $\sigma_x K$. The spin density profiles for the two degenerate ground states are depicted in Fig. 2.3(a) and (c), with the corresponding phase angles plotted in Fig. 2.3(b) and (d), respectively. These plots suggest that we can approximately write down the ground state wave functions as

$$\langle x\sigma|\, g_1\rangle = e^{ikx}\begin{bmatrix} \phi_1(x) & -\phi_2(x) \end{bmatrix}^T, \tag{2.6}$$

$$\langle x\sigma|\, g_2\rangle = e^{-ikx}\begin{bmatrix} \phi_2(x) & -\phi_1(x) \end{bmatrix}^T, \tag{2.7}$$

where $\phi_{1(2)}(x)$ is real and $\left[\phi_{1(2)}(x)\right]^2$ is represented by the red solid (blue dashed) line in Fig. 2.3(a), and k is the slope of the phase angles in Fig. 2.3(b). The density profiles of both $|g_1\rangle$ and $|g_2\rangle$ depicted in Fig. 2.3(a) and (c) are smooth in real space. These two states can be regarded as the analogies of the degenerate ground states for the uniform system, see Eqs. (2.3) and (2.4). However, due to the degeneracy, any linear superposition of $|g_1\rangle$ and $|g_2\rangle$ represents a ground state of the system. Such

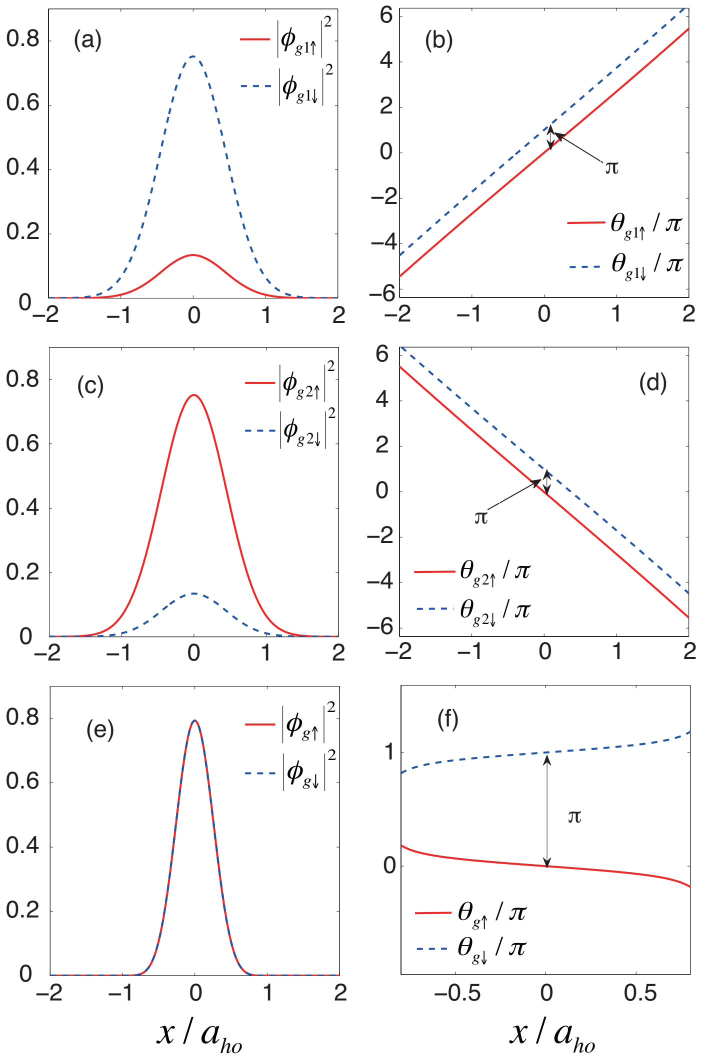

Figure 2.3 : Single-particle ground state wave functions with $\omega = 2\omega_0$, $q_r = 10\sqrt{m\hbar\omega_0}$, and $\delta = 0$. Red solid line and blue dashed line correspond to the spin-up component and the spin-down component, respectively. For two degenerate ground states at $\Omega = 130\hbar\omega_0$, (a)(c) are the real space probability profiles, and (b)(d) are the phase angles. For the non-degenerate ground state at $\Omega = 200\hbar\omega_0$, (e) is the real space probability profile, and (f) is the phase angle. We define $a_{\text{ho}} = \sqrt{\frac{\hbar}{m\omega_0}}$.

superposition state will exhibit a stripe pattern in its real space probability profile.

When $\Omega = 200\hbar\omega_0$, the ground state is non-degenerate. This state is depicted in Fig. 2.3(e) and (f). The symmetry property under the operation $\sigma_x K$ guarantees that, for a non-degenerate state, we must have $|\phi_\uparrow(x)| = |\phi_\downarrow(x)|$ and $\theta_\uparrow(x) + \theta_\downarrow(x) =$const. As can be seen from Fig. 2.3(e) and (f), these conditions are indeed satisfied by the non-degenerate ground state. Furthermore, the phase angles are almost uniform. As a result, this ground state can be approximately represented by

$$\langle x\sigma | g\rangle = \phi_0(x) \begin{bmatrix} 1/\sqrt{2} & -1/\sqrt{2} \end{bmatrix}^T , \tag{2.8}$$

where $\phi_0(x)$ is a real function and $[\phi_0(x)]^2/2$ is plotted in Fig. 2.3(e). This state is obviously the analogy of the non-degenerate ground state for the uniform system represented by Eq. (2.5).

Now we briefly discuss the case with finite δ. In this case, the single-particle state is always non-degenerate, possessing a non-vanishing magnetization $\langle\sigma_z\rangle$. In addition, the real-space wave packet of the ground state is always smooth.

2.2 Two-boson Ground State

The two-body physics of trapped particles with spin-orbit coupling has some non-trivial features. The research by D. Blume's group has investigated how the real-space spin structure [27] and the eigenenergy spectrum [28] depend on q_r, Ω, and the interaction strength (In those works, the interaction has SU(2) symmetry, i.e., the interaction between different spins are characterized by the same interaction strength). Here we investigate the system from a different perspective and focus on different parameter regimes. We study degeneracies, density-density correlations, and density profiles of the ground states, investigate connections between single-particle, two-particle, and many-particle ground states, and consider the parameters from current ^{87}Rb experiments with a spin-dependent interaction.

In this section, we consider two weakly interacting spin-orbit coupled bosons in a harmonic trap. To this end, we use the single-particle eigenstates discussed in the previous section to construct a set of two-body symmetric basis vectors for expanding the two-boson Hamiltonian. We label the single-particle eigenstates $|i\rangle$ with corresponding eigenenergies ϵ_i. Then states $|ii\rangle_b \equiv |i\rangle_1 |i\rangle_2$, and $|ij\rangle_b \equiv \frac{1}{\sqrt{2}} \left(|i\rangle_1 |j\rangle_2 + |j\rangle_1 |i\rangle_2 \right)$ for $i > j$ form the symmetric two-particle basis. Here $1, 2$ are particle indices and we take a cut-off for i, j in numerical calculation. Then the matrix elements of the two-particle Hamiltonian

$$H = h_1 + h_2 + \hat{V} \,, \tag{2.9}$$

with h_1 and h_2 being the single particle Hamiltonians and $\hat{V}$ the two-body contact interaction potential, can be written as

$$\langle ij| \left(h_1 + h_2 \right) |kl\rangle_b = \left(\epsilon_i + \epsilon_j \right) \delta_{ik} \delta_{jl} \,, \tag{2.10}$$

and

$$\langle ij| \hat{V} |kl\rangle_b = \sum_{\sigma_1 \sigma_2} g_{\sigma_1 \sigma_2} \int dx \, f^{ij}_{\sigma_1 \sigma_2} \left(x \right) \left[f^{kl}_{\sigma_1 \sigma_2} \left(x \right) \right]^* \,, \tag{2.11}$$

with $f^{ij}_{\sigma_1 \sigma_2} \left(x \right) =_b \langle ij| \, x\sigma_1 \rangle_1 |x\sigma_2\rangle_2$. Away from the confinement induced resonance, the quasi-1D interaction strength $g_{\sigma_1 \sigma_2}$ is related to the 3D interaction strength $g_{3D\sigma_1 \sigma_2}$ as $g_{\sigma_1 \sigma_2} = \frac{m\omega_\perp}{2\pi\hbar} g_{3D\sigma_1 \sigma_2}$, where $\omega_\perp$ is the strong transverse trap frequency [29]. In our calculation, we consider a spin symmetric interaction $g_{3D\uparrow\uparrow} = g_{3D\downarrow\downarrow} = 7.79 \times 10^{-12}$Hz cm^3, which is from current experiments in ^{87}Rb [13]. Accordingly, we take the quasi-1D interaction strength $g_{\uparrow\uparrow} = g_{\downarrow\downarrow} \equiv g$ with $g = 0.16\hbar\omega_0 a_{\text{ho}}$ where $a_{\text{ho}} = \sqrt{\hbar / \left(m\omega_0 \right)}$. In the scope of this Chapter, this interaction is relatively weak compared with center-of-mass motion energy and the spin-orbit-coupling energy, and hence the ground state of two interacting particles will not deviate much from the ground state in the non-interacting case. To characterize the properties of the ground state, we investigate the density-density correlation function which is defined as

$$\begin{aligned} C^{b}_{\sigma_1\sigma_2}\left(x_1,x_2\right) &\equiv \left\langle \Psi_g\right| \hat{n}_{\sigma_1}\left(x_1\right)\hat{n}_{\sigma_2}\left(x_2\right)\left|\Psi_g\right\rangle \\ &= 2\left|{}_1\left\langle x_1\sigma_1\right|{}_2\left\langle x_2\sigma_2\right| \Psi_g\rangle\right|^2 , \end{aligned} \tag{2.12}$$

and the density profile which is defined as

$$n^{b}_{\sigma}\left(x\right) \equiv \left\langle \Psi_g\right| \hat{n}_{\sigma}\left(x\right)\left|\Psi_g\right\rangle , \tag{2.13}$$

where $\hat{n}_\sigma\left(x\right)$ is the density operator of spin σ and $\left|\Psi_g\right\rangle$ represents the two-boson ground state in this section.

2.2.1 Two-boson Phase Diagram at $g_{\uparrow\downarrow} = 0.6g$

We obtain the low-lying eigenstates of the two-boson system by diagonalizing H after it has been expanded onto the symmetric two-particle basis states $|ij\rangle_b$. Here we still consider the case with $\delta = 0$. From the previous study of many-boson physics, we know that the stripe phase only appears with small δ, so this regime contains the most abundant many-boson physics. In the examples presented below, we choose the trap frequency to be $\omega = 2\omega_0$. We have checked that a different choice of ω does not lead to new quantum phases. In Fig. 2.4(a), we plot the energies of the three lowest eigenstates for several different values of Ω with $g_{\uparrow\downarrow} = 0.6g$. In Fig. 2.4(b), we plot ΔE_b, the energy difference between the two lowest energy states, as a function of Ω with several different values of $g_{\uparrow\downarrow}$. For now let us focus on the the case with $g_{\uparrow\downarrow} = 0.6g$ which is represented by the black solid line in Fig. 2.4(b). Depending on whether ΔE_b vanishes or not, the ground state then exhibits the following three phases as Ω varies:

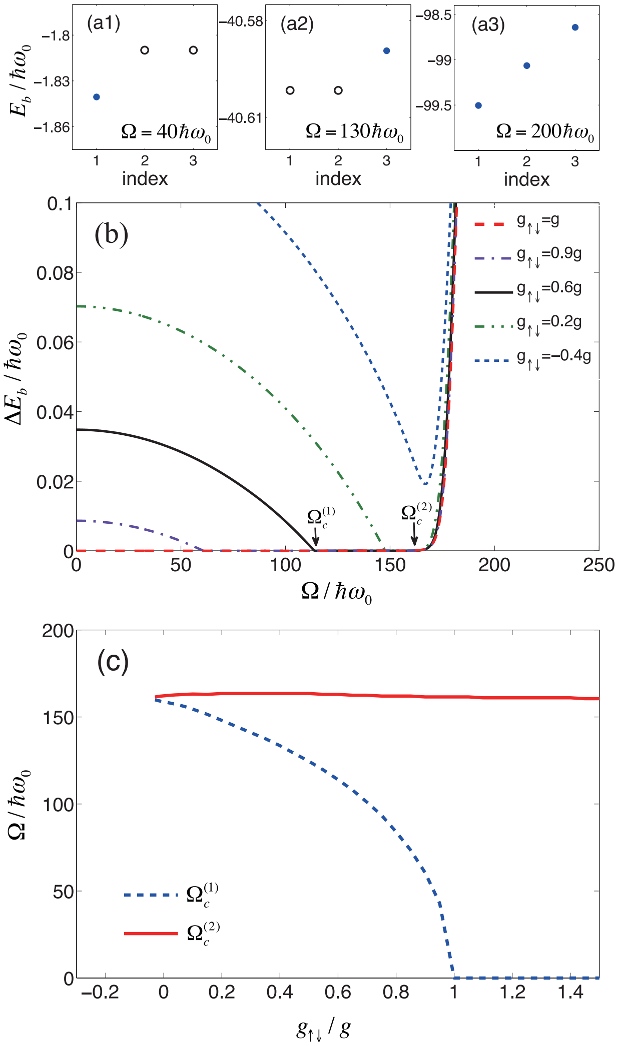

Figure 2.4 : (a) Energies of the lowest three two-boson eigenstates for $g_{\uparrow\downarrow}/g = 0.6$. Here solid and empty circles correspond to non-degenerate and degenerate states, respectively. (b) Energy difference between the two lowest energy states for the case of two weakly interacting bosons, as a function of Ω, for $g_{\uparrow\downarrow}/g = 1$, 0.9, 0.6, 0.2, -0.4. (c) $\Omega_c^{(1)}$ and $\Omega_c^{(2)}$ as functions of $g_{\uparrow\downarrow}$. The other parameters are: $\delta = 0$, $q_r = 10\sqrt{m\hbar\omega_0}$, $\omega = 2\omega_0$, $g = 0.16\hbar\omega_0 a_{\text{ho}}$. The 1D interaction strength g is calculated from 3D interaction parameter $g_{3D} = 7.79 \times 10^{-12}\text{Hz cm}^3$ with a transverse trapping frequency $\omega_\perp = 100\omega_0$.

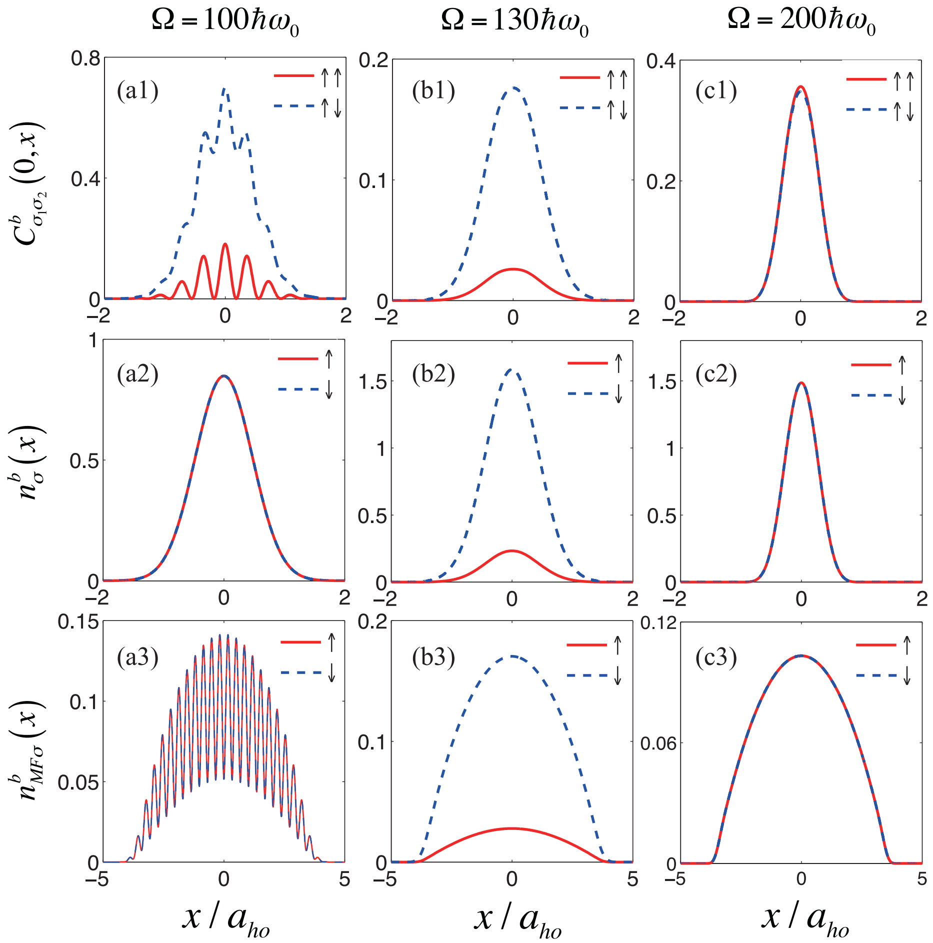

Figure 2.5 : (a1)-(c1) Density-density correlation functions of two-boson ground states. (a2)-(c2) Spin density profiles of two-boson ground states. (a3)-(c3) Mean-field ground state density profiles for a condensate of 1000 bosons. The figures are plotted for the cases with $\Omega/(\hbar\omega_0) = 100, 130, 200$, and $g_{\uparrow\downarrow} = 0.6g$, $\delta = 0$. At $\Omega = 130\hbar\omega_0$, the ground states are two-fold degenerate and the figures are for one of the degenerate states.

Phase I — When $\Omega < \Omega_c^{(1)} \approx 115\hbar\omega_0$, ΔE_b is finite, so the two-boson ground state is non-degenerate. In this regime, the single-particle ground state is two-fold degenerate and we label the two single-particle ground states as $|g_1\rangle$ and $|g_2\rangle$ (see discussion in Sec. 2.1). The ground state of the two boson system can then be approximately represented as

$$\left|\Psi_g^{\mathrm{I}}\right\rangle \approx |g_1 g_2\rangle_b \equiv \frac{1}{\sqrt{2}}\left(|g_1\rangle_1|g_2\rangle_2 + |g_2\rangle_1|g_1\rangle_2\right) . \tag{2.14}$$

Hence the two bosons each occupies one of the single-particle ground states. Due to the bosonic statistics, the two bosons are highly entangled. In Fig. 2.5(a1) and (a2), we plot the density-density correlation $C^b_{\sigma_1\sigma_2}(0,x)$ and the spin density profiles $n^b_\sigma(x)$, respectively. The two-boson ground state features a smooth density profile identical for the two spin components. However, the entanglement manifests itself in the oscillations (or stripes) in $C^b_{\sigma_1\sigma_2}(0,x)$. Given the two-boson ground state in Eq. (2.14) and the single-particle ground states in Eqs. (2.6) and (2.7), we can explicitly write down the density-density correlation functions and the spin density profiles as

$$\begin{aligned}
C^b_{\uparrow\uparrow}(x_1,x_2) = C^b_{\downarrow\downarrow}(x_1,x_2) &\approx A_1 + B\cos\left[2k\left(x_1 - x_2\right)\right] \; ; \\
C^b_{\uparrow\downarrow}(x_1,x_2) = C^b_{\downarrow\uparrow}(x_1,x_2) &\approx A_2 + B\cos\left[2k\left(x_1 - x_2\right)\right] \; , \\
n^b_\uparrow(x) = n^b_\downarrow(x) &\approx \phi_1^2(x) + \phi_2^2(x) \, ,
\end{aligned} \tag{2.15}$$

with

$$\begin{aligned}
A_1 &\equiv \phi_1^2\left(x_1\right)\phi_2^2\left(x_2\right) + \phi_1^2\left(x_2\right)\phi_2^2\left(x_1\right) ; \\
A_2 &\equiv \phi_1^2\left(x_1\right)\phi_1^2\left(x_2\right) + \phi_2^2\left(x_1\right)\phi_2^2\left(x_2\right) ; \\
B &\equiv 2\phi_1\left(x_1\right)\phi_2\left(x_2\right)\phi_1\left(x_2\right)\phi_2\left(x_1\right) .
\end{aligned} \tag{2.16}$$

being smooth functions of x_1 and x_2. The stripes in the density-density correlation arise from the sinusoidal terms in Eq. (2.15). We note in Fig. 2.4(a1) that in this phase, the first excited two-boson state is doubly degenerate. The two degenerate states roughly correspond to $|g_1 g_1\rangle_b$ and $|g_2 g_2\rangle_b$.

In order to connect the two-body physics to the many-body physics, we plot in Fig. 2.5(a3) the mean-field condensate density profile. The condensate wave function is obtained by minimizing the mean-field energy functional

$$\begin{aligned} E_{\mathrm{MF}} &= \int dx \left[N \left(\Phi_\uparrow^* \ \Phi_\downarrow^* \right) h \begin{pmatrix} \Phi_\uparrow \\ \Phi_\downarrow \end{pmatrix} \right. \\ &\quad \left. + \frac{N^2 g}{2} (|\Phi_\uparrow|^4 + |\Phi_\downarrow|^4) + N^2 g_{\uparrow\downarrow} |\Phi_\uparrow|^2 |\Phi_\downarrow|^2 \right] , \end{aligned} \tag{2.17}$$

where $\Phi_\uparrow$ and $\Phi_\downarrow$ are the condensate wave functions of the two spin components, and N is the total number of atoms, which we take to be 1000 in this calculation. Fig. 2.5(a3) shows that the condensate is in the so-called stripe phase where the density profile exhibits a stripe pattern. This stripe pattern can therefore be regarded as a manifestation of the stripes in the two-body correlation function shown in Fig. 2.5(a1), even though the two-body density profiles are smooth. Similar connection between the mean-field many-body calculation and the quantum few-body result is also found elsewhere [30, 31]. See Sec. 2.2.2 for a more detailed discussion.

Finally, let us consider the effect of finite two-photon detuning δ. A finite δ breaks the degeneracy of the single-particle ground state. Hence one may expect that for a large $|\delta|$, the ground state of the two weakly interacting bosons corresponds to an unentangled state with both bosons occupying the non-degenerate single-particle ground state. For this unentangled ground state, $C^b_{\sigma_1\sigma_2}(x_1, x_2)$ becomes smooth. However, for a sufficiently small $|\delta|$, the two-boson ground state still roughly takes the form

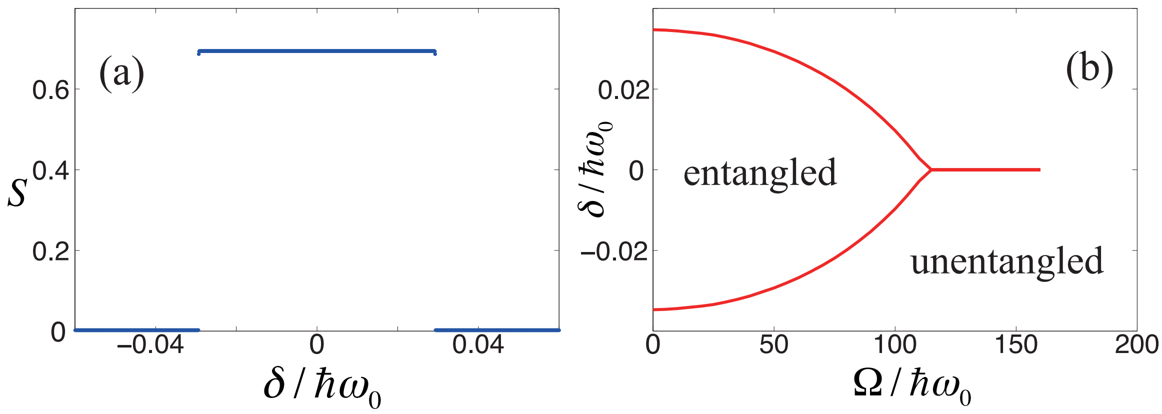

Figure 2.6 : (a) Von Neumann entanglement entropy of the two-boson ground state, as a function of δ. The figure is plotted for the case with $g_{\uparrow\downarrow} = 0.6g$ and $\Omega = 50\hbar\omega_0$. (b) The boundary of entangled and non-entangled ground states with $g_{\uparrow\downarrow} = 0.6g$, as a function of δ and Ω. In the "entangled" region , ground states are strongly entangled and thus exhibit stripes in density-density correlations. In the "unentangled" region, ground states are not entangled and show smooth density-density correlations. Other parameters: $q_r = 10\sqrt{m\hbar\omega_0}$, $\omega = 2\omega_0$, $g = 0.16\hbar\omega_0$.

of Eq. (2.14), with $|g_1\rangle$, $|g_2\rangle$ representing the ground and first excited single-particle states, and thus $C^b_{\sigma_1\sigma_2}(x_1, x_2)$ still exhibits stripes. To demonstrate the variation of the entanglement, we plot in Fig. 2.6(a) the entanglement entropy S of the two-boson ground state, where $S = -\mathrm{Tr}[\rho_1 \ln \rho_1]$ with $\rho_1 = \mathrm{Tr}_2[|\Psi_g\rangle\langle\Psi_g|]$ being the reduced density matrix for particle 1. The state represented by (2.14) is maximally entangled with $S = \ln 2$. Using the numerically obtained ground states with finite $|\delta|$, we find that S is very close to $\ln 2$ for $|\delta| < 0.03\hbar\omega_0$, and beyond this range, S quickly drops to 0, indicating an unentangled ground state. The range of δ within which the ground state is entangled is shown in Fig. 2.6(b) as a function of Ω. As Ω tends to $\Omega_c^{(1)}$, this range approaches zero. In Fig. 2.6(b), The "entangled" ("unentangled") region manifests itself in oscillating (smooth) density-density correlations.

Phase II — When $\Omega_c^{(1)} < \Omega < \Omega_c^{(2)}$, $\Delta E_b = 0$ indicates that the ground states have two-fold degeneracy. Here $\Omega_c^{(2)} \approx 160\hbar\omega_0$ is very close to the critical Raman coupling strength Ω_c at which the single-particle ground state changes from degenerate to non-degenerate. Our result shows that the two degenerate two-boson ground states can be approximately represented as

$$\begin{aligned} \left|\Psi_{g1}^{\mathrm{II}}\right\rangle &\approx \left|g_1 g_1\right\rangle_b \equiv \left|g_1\right\rangle_1 \left|g_1\right\rangle_2 \ , \\ \left|\Psi_{g2}^{\mathrm{II}}\right\rangle &\approx \left|g_2 g_2\right\rangle_b \equiv \left|g_2\right\rangle_1 \left|g_2\right\rangle_2 \ . \end{aligned} \tag{2.18}$$

Hence the two bosons occupy the same single-particle ground state. In Fig. 2.5(b1) and (b2), we plot $C_{\sigma_1\sigma_2}^b(0,x)$ and $n_\sigma^b(x)$ for $\left|\Psi_{g1}^{\mathrm{II}}\right\rangle$, respectively, whose explicit expressions in terms of the single-particle ground states are approximately given by:

$$\begin{aligned} C_{\uparrow\uparrow}^b(x_1,x_2) &\approx 2\phi_1^2(x_1)\phi_1^2(x_2)\,; \\ C_{\downarrow\downarrow}^b(x_1,x_2) &\approx 2\phi_2^2(x_1)\phi_2^2(x_2)\,; \\ C_{\uparrow\downarrow}^b(x_1,x_2) &\approx 2\phi_1^2(x_1)\phi_2^2(x_2)\,; \\ C_{\downarrow\uparrow}^b(x_1,x_2) &\approx 2\phi_1^2(x_2)\phi_2^2(x_1)\,, \\ n_\uparrow^b(x) &= 2\phi_1^2(x)\,; \\ n_\downarrow^b(x) &= 2\phi_2^2(x)\,. \end{aligned} \tag{2.19}$$

In this regime, both the density-density correlation functions and the spin density profiles are smooth functions of the position. In addition, the total magnetization $\mathbf{M} \equiv \int dx\,[n_\uparrow(x) - n_\downarrow(x)] \neq 0$ in this phase. The corresponding mean-field condensate density profiles are plotted in Fig. 2.5(b3). Here the condensate is in the so-called plane-wave phase and the density profiles for the two spin components are smooth. The condensate in this phase also exhibits finite magnetization.

Note that the two degenerate states $|\Psi_{g1}^{\mathrm{II}}\rangle$ and $|\Psi_{g2}^{\mathrm{II}}\rangle$ represented in Eq. (2.18) are unentangled states. However, due to the degeneracy, any superposition state of $|\Psi_{g1}^{\mathrm{II}}\rangle$

and $|\Psi_{g2}^{\mathrm{II}}\rangle$ is still a ground state of the two-body system, and such a superposition state is entangled. However, this entanglement is not robust against a finite two-photon detuning δ: any finite δ will force both atoms to occupy the same non-degenerate single-particle ground state, and hence destroy the entanglement and result in the smooth $C^b_{\sigma_1\sigma_2}(x_1, x_2)$. This represents an essential difference for the ground state entanglement property between Phase I and II.

In Phase II, we note that the first excited state is non-degenerate as shown in Fig. 2.4(a2) and roughly corresponds to $|g_1 g_2\rangle_b$. Hence the ground state of Phase I corresponds to the first excited state of Phase II, and vice versa. These two phases result from the competition between the following two factors: (1) The quantum statistical property of bosons favors identical bosons to occupy the same single-particle state; and (2) the smaller inter-species interaction ($g_{\uparrow\downarrow} < g$) favors the bosons to occupy different spin states, and the smaller Raman coupling strength Ω induces more difference between the spins of $|g_1\rangle$ and $|g_2\rangle$. We present in Sec. 2.2.3 a detailed and quantitative discussion on this.

Phase III — When $\Omega > \Omega_c^{(2)}$, the gap reopens as ΔE_b becomes finite again. In this regime, the single-particle ground state $|g\rangle$, whose wave function is given in Eq. (2.8), is also non-degenerate. The two-boson ground state can then be approximately represented by

$$\left|\Psi_g^{\mathrm{III}}\right\rangle \approx |gg\rangle_b \equiv |g\rangle_1 |g\rangle_2 \ , \tag{2.20}$$

which features a smooth $C^b_{\uparrow\uparrow}(0, x) \approx C^b_{\uparrow\downarrow}(0, x)$ and identical $n^b_\uparrow(x) = n^b_\downarrow(x)$, as shown in Fig. 2.5(c1) and (c2). The explicit expressions are approximately given by:

$$C^b_{\uparrow\uparrow}(x_1,x_2) = C^b_{\downarrow\downarrow}(x_1,x_2) \approx \tfrac{1}{2}\phi_0^2(x_1)\phi_0^2(x_2)\,; \tag{2.21}$$

$$C^b_{\uparrow\downarrow}(x_1,x_2) = C^b_{\downarrow\uparrow}(x_1,x_2) \approx \tfrac{1}{2}\phi_0^2(x_1)\phi_0^2(x_2)\,;$$

$$n^b_{\uparrow}(x) = n^b_{\downarrow}(x) \approx \phi_0^2(x)\,.$$

The corresponding mean-field condensate density profiles are plotted in Fig. 2.5(c3). As in the two-body case, the condensate is smooth and features identical density profiles for the two spin components.

In this Phase, all the two-boson eigenstates are non-degenerate, as well as all the single-particle eigenstates. The weak interaction only causes small shifts of the eigenenergies, but does not affect the degeneracies.

2.2.2 Two-boson versus Many-boson Results

One of the goals of our work is to bridge the two-body and the many-body physics. Most of the many-body properties of weakly interacting condensate can be well understood under the mean-field framework. In the mean-field approach, the underlying assumption is that all the atoms occupy the same single-particle state and quantum entanglement between atoms is neglected. The two-body ground states in Phase II and III studied in Sec. 2.2 are consistent with this assumption, and the connection between the two-body and many-body physics can be easily seen from the right two columns of Fig. 2.5. By contrast, Phase I requires some special attention.

In Phase I of the two-boson system, the single-particle ground states are two-fold degenerate and are denoted as $|g_1\rangle$ and $|g_2\rangle$, and the two-boson ground state is given in Eq. (2.14), which we rewrite here:

$$\left|\Psi_g^{\mathrm{I}}\right\rangle \approx |g_1 g_2\rangle_b \equiv \frac{1}{\sqrt{2}}\left(|g_1\rangle_1|g_2\rangle_2 + |g_2\rangle_1|g_1\rangle_2\right)\,. \tag{2.22}$$

State $\left|\Psi_g^{\mathrm{I}}\right\rangle$ is a maximally entangled state, hence is expected to be very different from the mean-field ground state. In fact, in this regime, in the language of second quantization the mean-field many-body ground state can be roughly represented as

$$|\Psi_{\mathrm{MF}}(\theta)\rangle = \frac{1}{\sqrt{2^N N!}}\left(e^{-i\theta/2}a_1^\dagger + e^{i\theta/2}a_2^\dagger\right)^N |0\rangle \,, \tag{2.23}$$

where $N \gg 1$ is the number of particles, $|0\rangle$ is the vacuum state with no atoms, and $a_i^\dagger$ is the creation operator that create an atom in single-particle state $|g_i\rangle$. This mean-field state corresponds to the situation where all atoms occupy the same single-particle state $(e^{-i\theta/2}|g_1\rangle + e^{i\theta/2}|g_2\rangle)/\sqrt{2}$ which is a coherent superposition of the two single-particle ground state, with θ being an arbitrary phase. This state possesses no quantum entanglement between different particles, but do give rise to the density stripe as shown in Fig. 2.5(a3).

We can draw an analogy from a different system: a system of many scalar bosons in a double-well potential, in which the operators $a_i^\dagger$ correspond to creation operator that creates a particle in the ith well ($i = 1,\ 2$). This system is analyzed in detail in Ref. [30]. The mean-field analysis yields a state similar to Eq. (2.23), but the quantum calculation produces a different result to the mean field.

The mean-field state $|\Psi_{\mathrm{MF}}(\theta)\rangle$ in Eq. (2.23) has, on average, $N/2$ atoms in both $|g_1\rangle$ and $|g_2\rangle$. However, the occupation number for each of these states possess large fluctuations. It is probably beyond anyone's capability to write down the full quantum many-body wavefunction for this system. However, we can still make some qualitative remarks with insights drawn from Ref. [30]. In quantum treatment, large number fluctuations, as included in the mean-field state $|\Psi_{\mathrm{MF}}(\theta)\rangle$, are in general not favored by interaction, which tends to drive the state into the Fock state:

$$|\Psi_{\mathrm{F}}\rangle = \frac{1}{(N/2)!}(a_1^\dagger)^{N/2}(a_2^\dagger)^{N/2}|0\rangle \,, \tag{2.24}$$

which is just the N-body analog of the two-body ground state $|\Psi_g^{\mathrm{I}}\rangle$. Furthermore, the Fock state $|\Psi_{\mathrm{F}}\rangle$ may be roughly regarded as a superposition of mean-field states averaged over the phase θ, i.e.,

$$|\Psi_{\mathrm{F}}\rangle \approx C \int_0^{2\pi} d\theta \, |\Psi_{\mathrm{MF}}(\theta)\rangle$$

where C is a normalization constant. Conversely, the mean-field state may be regarded as a broken-symmetry state with a random but fixed θ.

Therefore, we can establish the following connection between the two-body results and the mean-field many-body results for Phase I. The two-body ground state does not exhibit strips in the density profiles, as can be seen in Fig. 2.5(a2), but does contain quantum entanglement between the particles and exhibit oscillations in the correlation function, as shown in Fig. 2.5(a1). As the number of atoms increases and the mean-field limit is approached, quantum entanglement becomes more and more fragile, and is completely neglected in the mean-field treatment. The mean-field assumption is also consistent with the picture of spontaneous symmetry breaking, where a random but specific θ is selected and all the atoms are considered to be condensed into the linear superposition state of $|g_1\rangle$ and $|g_2\rangle$ with a phase difference θ. Such a state leads to the stripe pattern in the density profile, as shown in Fig. 2.5(a3). We can therefore state the following: For the system under current study, through spontaneous symmetry breaking, the oscillations in two-body correlation function become manifest in the stripes of mean-field density profiles.

We remark that this connection between few-body correlation function and mean-field density profile is not unique to our system. For example, Kanamoto *et al.* studied a system of attractive scalar bosons confined along a ring [31]. When the attractive interaction strength exceeds a critical value, the mean-field calculation shows that the density profile of the BEC becomes inhomogeneous and take the form of a bright soliton. However, the quantum calculation for a few-body system always gives a homogeneous density profile, but the second-order correlation function exhibit inhomogeneity.

2.2.3 Two-boson Ground State in Phase I and Phase II

In both Phase I and II of the two-boson system, the single-particle ground states are two-fold degenerate and are denoted as $|g_1\rangle$ and $|g_2\rangle$. In the case of two interacting bosons, the following two situations represent potential candidates for the ground state:

1. Both atoms occupy the same single-particle ground state. Hence the two-boson state is given by $|g_1g_1\rangle_b$ or $|g_2g_2\rangle_b$, which are the states represented by Eqs. (2.18). From symmetry, we know that these two states are always energetically degenerate, hence we only consider $|g_1g_1\rangle_b$ in the following.

2. The two atoms occupy different single-particle ground state. Hence the two-boson state is given by $|g_1g_2\rangle_b$, which is the state represented by Eq. (2.14).

The question of concern is which state, $|g_1g_1\rangle_b$ or $|g_1g_2\rangle_b$, possesses the lower energy. It is obvious that we only need to compare the interaction energy associated with these two states, which we denote as $E_{\text{int}}^{\text{I,II}}$ with

$$\begin{aligned} E_{\text{int}}^{\text{I}} &\equiv {}_b\langle g_1g_2|\hat{V}|g_1g_2\rangle_b \,, \\ E_{\text{int}}^{\text{II}} &\equiv {}_b\langle g_1g_1|\hat{V}|g_1g_1\rangle_b \,. \end{aligned}$$

With Eqs. (2.6), (2.7), and (3.12), it is straightforward to show that

$$\begin{aligned} E_{\text{int}}^{\text{I}} &= \left(4g + 2g_{\uparrow\downarrow}\right) D + g_{\uparrow\downarrow} F \,, \\ E_{\text{int}}^{\text{II}} &= 2g_{\uparrow\downarrow} D + gF \,, \end{aligned}$$

where

$$D = \int dx\, \phi_1^2(x)\, \phi_2^2(x)\ , \tag{2.25}$$

$$F = \int dx\ \left[\phi_1^4(x) + \phi_2^4(x)\right]\ ,$$

from which we have

$$E_{\text{int}}^{\text{I}} - E_{\text{int}}^{\text{II}} = gF\left[\frac{g_{\uparrow\downarrow}}{g} - f(\Omega)\right]\ , \tag{2.26}$$

where $f(\Omega) = 1 - 4D/F$ and, according to our numerics, is a decreasing function of Ω and satisfies the condition $0 < f(\Omega) < 1$.

If the interaction is spin-independent, i.e., $g_{\uparrow\downarrow} = g$, Eq. (2.26) shows that $E_{\text{int}}^{\text{I}} > E_{\text{int}}^{\text{II}}$, the two-boson system is in Phase II and the two atoms occupy the same single-particle state. This is the manifestation of the bosonic statistics, which favors repulsive bosons to occupy the same state.

For spin-dependent interaction, the situation is more complicated. If $g_{\uparrow\downarrow} > g$, $E_{\text{int}}^{\text{I}} > E_{\text{int}}^{\text{II}}$ still holds, and the interaction also favors two atoms occupying the same state. Hence the interaction effect and the statistical property strengthens each other, and the system remains in Phase II. If $g_{\uparrow\downarrow} < g$, the interaction favors two atoms occupying different states, and hence competes with the statistical effect. For a given Ω, when $g_{\uparrow\downarrow} < gf(\Omega)$, the interaction wins the competition and the system enters Phase I. The above analysis also agrees with Fig. 2.4(b) by showing that for a given $g_{\uparrow\downarrow} < g$, the system enters Phase I when $\Omega < f^{-1}(g_{\uparrow\downarrow}/g)$.

One may still ask the question: In Phase II, can the two atoms occupy the same single-particle state which is a linear superposition of $|g_1\rangle$ and $|g_2\rangle$? For example, how about the state $|\Psi_{\text{MF}}(\theta)\rangle$ as in Eq. (2.23) with $N = 2$, which represents the state where both atoms occupy the single-particle state $(e^{-i\theta/2}|g_1\rangle + e^{i\theta/2}|g_2\rangle)/\sqrt{2}$. The answer is that such a state is not favored in Phase II. This can also be understood from the interaction energy. State $|\Psi_{\mathrm{MF}}(\theta)\rangle$ can be regarded as a linear superposition of $|g_1 g_1\rangle_b$, $|g_2 g_2\rangle_b$, and $|g_1 g_2\rangle_b$. The first two are the degenerate two-boson ground state in Phase II, while the last one is the corresponding first excited state. Hence $|\Psi_{\mathrm{MF}}(\theta)\rangle$ cannot represent the ground state.

2.2.4 Effects of $g_{\uparrow\downarrow}$ on Two-boson Phase Diagram

The above discussion demonstrates that, with $g_{\uparrow\downarrow} = 0.6g$, the ground state exhibits three phases separated by two critical Raman coupling strengths $\Omega_c^{(1)}$ and $\Omega_c^{(2)}$. Now let us discuss how the two-body phase diagram is changed when the inter-species interaction strength $g_{\uparrow\downarrow}$ is varied, while the intra-species interaction strength is fixed at value g.

In Fig. 2.4(b), we also plot the energy difference between the two lowest energy states for several other values of $g_{\uparrow\downarrow}$. The dependence of $\Omega_c^{(1)}$ and $\Omega_c^{(2)}$ on $g_{\uparrow\downarrow}$ are plotted in Fig. 2.4(c). From these plots, we see that $\Omega_c^{(1)}$ vanishes for $g_{\uparrow\downarrow} \geq g$. In other words, when the inter-species interaction strength exceeds the intra-species interaction strength, Phase I, and hence the stripe phase in the mean-field many-body regime, no longer exists. We have checked that this property is independent of the trap frequency ω.

As $g_{\uparrow\downarrow}$ decreases from g, $\Omega_c^{(1)}$ increases from zero and approaches $\Omega_c^{(2)}$, while $\Omega_c^{(2)}$ remains almost unchanged. Correspondingly, the parameter space where Phase II exists shrinks. At a critical value of $g_{\uparrow\downarrow}$, the two critical Raman coupling strengths merge, and for $g_{\uparrow\downarrow}$ smaller than this value, the two-body ground state is no longer degenerate for any values of Ω, and ΔE_b is always positive (see the curve in Fig. 2.4(a) with $g_{\uparrow\downarrow} = -0.4g$).

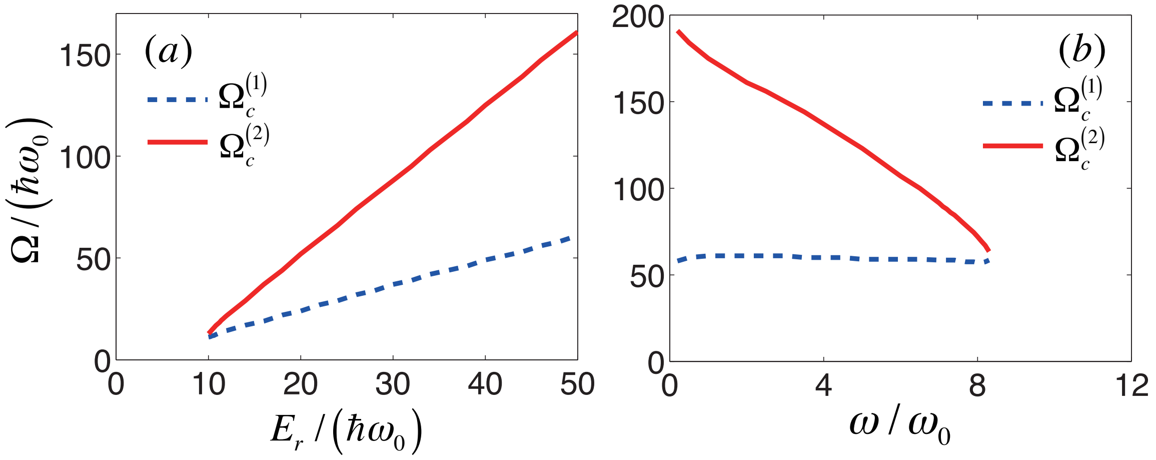

Figure 2.7 : Two critical Raman coupling strengths $\Omega_c^{(1)}$ and $\Omega_c^{(2)}$, (a) as a function of recoil energy E_r with a fixed trap frequency $\omega = 2\omega_0$, and (b) as a function of trap frequency ω with a fixed recoil energy $E_r = 50\hbar\omega_0$. The other parameters are: $g_{\uparrow\downarrow} = 0.9g$, $g = 0.16\hbar\omega_0 a_{\mathrm{ho}}$, $\delta = 0$.

2.2.5 Effects of E_r and ω on Two-boson Phase Diagram

In the above discussion, we have taken the trap frequency $\omega = 2\omega_0$ and the recoil energy $E_r \equiv q_r^2/2m = 50\hbar\omega_0$, by referring to parameters from current experiments in ^{87}Rb [3]. Since both E_r and ω can be tuned in cold atom experiments, here we discuss how the changes of E_r and ω affect the two critical Raman coupling strengths $\Omega_c^{(1)}$ and $\Omega_c^{(2)}$ for $g_{\uparrow\downarrow} = 0.9g$ shown in Fig. 2.4(b).

Figure 2.7(a) plots the dependence of $\Omega_c^{(1)}$ and $\Omega_c^{(2)}$ on E_r at the fixed trap frequency $\omega = 2\omega_0$. As E_r decreases from $50\hbar\omega_0$, both $\Omega_c^{(1)}$ and $\Omega_c^{(2)}$ decrease and the regime of Phase II exists shrinks. At a critical value of E_r around $10\hbar\omega_0$, the two critical Raman coupling strengths merge, and for E_r smaller than this critical value, Phase II disappears.

Figure 2.7(b) depicts $\Omega_c^{(1)}$ and $\Omega_c^{(2)}$ as functions of ω at the fixed recoil energy $E_r = 50\hbar\omega_0$. Here we see that $\Omega_c^{(1)}$ is not very sensitive to ω, while $\Omega_c^{(2)}$ is a decreasing function of ω. At a critical value of ω, $\Omega_c^{(1)}$ and $\Omega_c^{(2)}$ merge and Phase II disappears. That the dependence of $\Omega_c^{(2)}$ on E_r and ω should be expected, because the critical Ω for the single-particle degenerate transition, which is approximately equal to $\Omega_c^{(2)}$, has a similar dependence on these two parameters as shown in Fig. 2.2(b).

2.3 Two-fermion Ground State

The physics of the two-fermion ground state is quite different from that of two bosons, because of the antisymmetric nature and the Pauli exclusion principle for the quantum states of identical fermions. The Hamiltonian, density-density correlation functions, and spin density profiles of the two-fermion system are given by Eqs. (2.9), (2.12), and (2.13), respectively, where $|\Psi_g\rangle$ denotes the two-fermion ground state. As we are only considering s-wave contact interaction, there is no intra-species interaction between two fermions. To investigate the properties of this system, we expand the Hamiltonian onto the antisymmetric two-particle basis states $|ij\rangle_f \equiv \frac{1}{\sqrt{2}}(|i\rangle_1|j\rangle_2 - |j\rangle_1|i\rangle_2)$, and then follow a similar procedure as above for the two-boson case.

Through exact diagonalization of the Hamiltonian in Eq. (2.9) with $\delta = 0$, we obtain ΔE_f, the energy difference between the two lowest-lying states, and plot it in Fig. 2.8 as a function of Ω for several different values of $g_{\uparrow\downarrow}$. As Ω increases from zero, ΔE_f first decreases and reaches a minimum near Ω_c (the critical value of the Raman coupling strength at which the single-particle ground state degeneracy is lifted), and then starts to increase again. The essential difference with the two-boson case is that here ΔE_f is always positive and never becomes zero. Furthermore, since we are concerned with the weak interaction regime, the interaction strength $g_{\uparrow\downarrow}$ does not have a significant effect on the system.

In Fig. 2.9, we display the properties of the two-fermion ground states for two

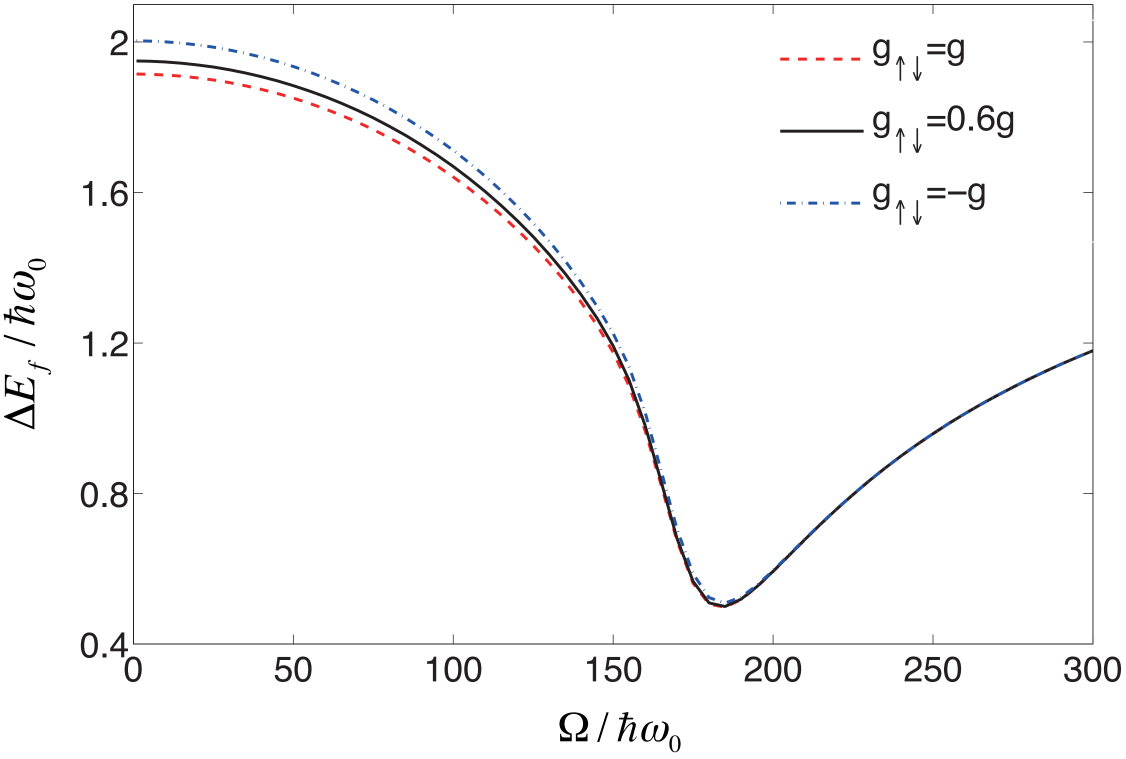

Figure 2.8 : For the case of two weakly interacting fermions, energy difference between the first excited state and the ground state, as a function of Ω with $g_{\uparrow\downarrow} = g, 0.6g, -g$. The parameters: $\delta = 0$, $q_r = 10\sqrt{m\hbar\omega_0}$, $\omega = 2\omega_0$, $\omega_\perp = 100\omega_0$, $g = 0.16\hbar\omega_0$.

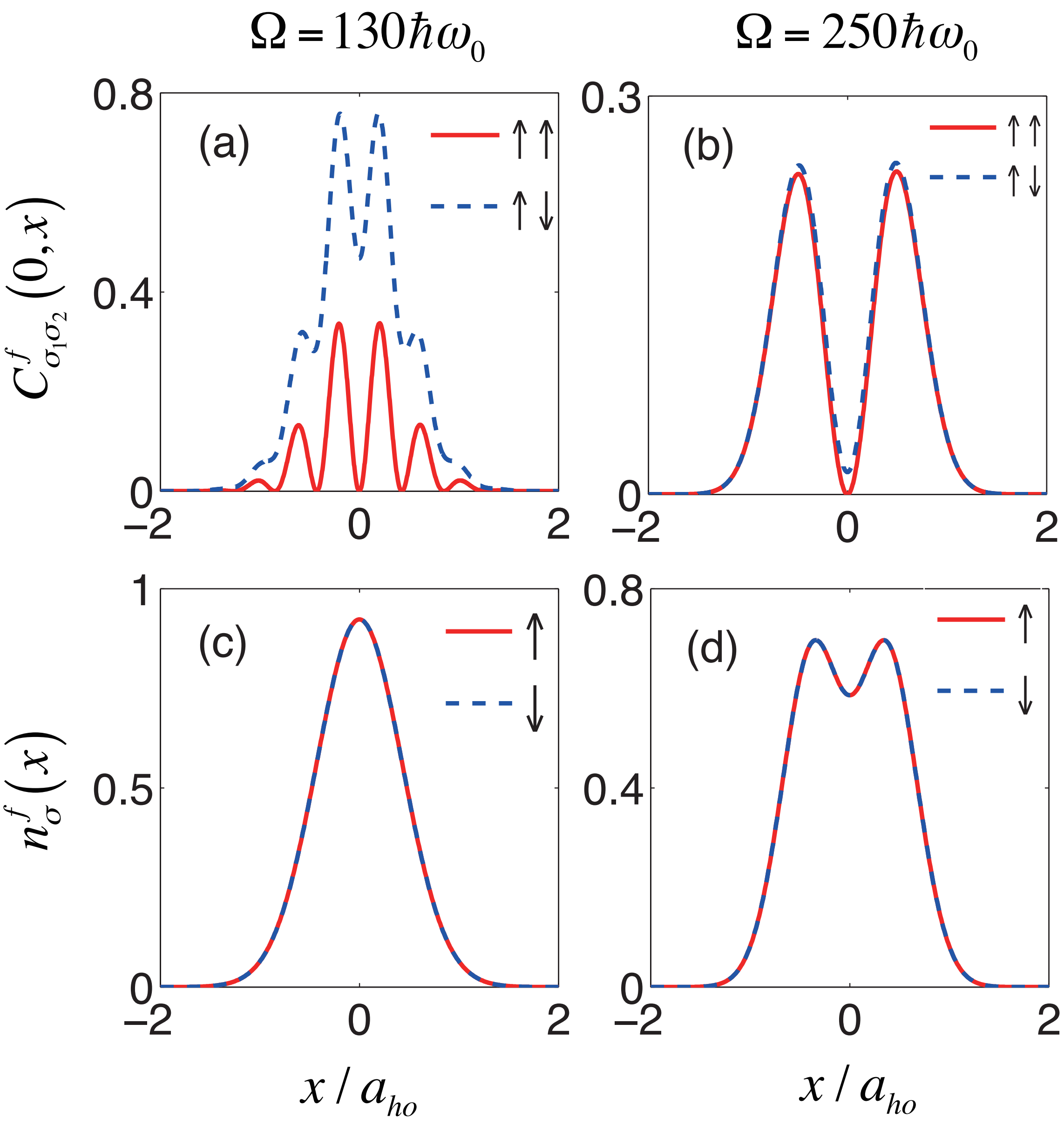

Figure 2.9 : (a)(b) Density-density correlations of two-fermion ground states, which satisfy $C^f_{\uparrow\uparrow}(0,x) = C^f_{\downarrow\downarrow}(0,x)$ and $C^f_{\uparrow\downarrow}(0,x) = C^f_{\downarrow\uparrow}(0,x)$. (c)(d) Spin density profiles of two-fermion ground states. The figures are plotted for the cases with $\Omega/\hbar\omega_0 = 130, 250$, $g_{\uparrow\downarrow} = 0.6g$ and $\delta = 0$.

Raman coupling strengths, one smaller and the other larger than Ω_c:

$\Omega < \Omega_c$ — For this case, the single-particle ground states, $|g_1\rangle$ and $|g_2\rangle$, are two-fold degenerate, and the two-fermion ground state can be approximately represented as

$$|\Psi_g\rangle \approx |g_1 g_2\rangle_f = \frac{1}{\sqrt{2}} \left(|g_1\rangle_1 |g_2\rangle_2 - |g_2\rangle_1 |g_1\rangle_2 \right) , \tag{2.27}$$

from which the correlation functions and density profiles can be straightforwardly calculated as

$$\begin{aligned} C^f_{\uparrow\uparrow}(x_1, x_2) = C^f_{\downarrow\downarrow}(x_1, x_2) &\approx A_1 - B\cos\left[2k\left(x_1 - x_2\right)\right] \; ; \\ C^f_{\uparrow\downarrow}(x_1, x_2) = C^f_{\downarrow\uparrow}(x_1, x_2) &\approx A_2 - B\cos\left[2k\left(x_1 - x_2\right)\right] \; ; \\ n^f_\uparrow(x) = n^f_\downarrow(x) &\approx \phi_1^2(x) + \phi_2^2(x) \, , \end{aligned} \tag{2.28}$$

with A_1, A_2, and B given in Eq. (2.16). The numerical results are displayed in Fig. 2.9(a) and (c). For this case, the density-density correlation function $C^f_{\sigma_1\sigma_2}(x_1, x_2)$ is characterized by oscillations (or stripes) which arise from the sinusoidal terms in Eq. (2.28).

$\Omega > \Omega_c$ — For this case, the single-particle ground state $|g\rangle$ is non-degenerate. The two-fermion ground state can be approximately represented as

$$|\Psi_g\rangle \approx |ge\rangle_f = \frac{1}{\sqrt{2}} \left(|g\rangle_1 |e\rangle_2 - |e\rangle_1 |g\rangle_2 \right) , \tag{2.29}$$

where $|e\rangle$ denotes the non-degenerate single-particle first excited state. The density-density correlation functions and spin density profiles are displayed in Fig. 2.9(b) and (d), respectively. In contrast to the single-peak structure in the previous case, here the spin density profile exhibits a double-peak structure because the real space probability profile of $|e\rangle$ features double peaks.

We remark that a system of two atoms is not unrealistic. Current technology has made it possible to trap deterministic few atoms, which allows us not only to systematically investigate the connection between few- and many-body physics, but also to study unique features of few-body systems. In a series of experiments carried out in S. Jochim's group [32], a few-body system of fermions, with atom number precisely controlled between 1 and 10, is realized in an optical dipole trap with a fidelity of 90%. If we apply the spin-orbit coupling in this kind of experiments, the ground states studied in our work should be readily obtained and their properties such as density profiles and correlations can be measured.

2.4 Measuring the Interaction induced Energy Gap

In Sec. 2.2, we have demonstrated that, for the two-boson case with $\delta = 0$, the energy gap ΔE_b in Phase I with $\Omega < \Omega_c^{(1)}$ is induced by the spin-dependent interaction. For fixed values of Ω and g in this regime, $g_{\uparrow\downarrow}$ and ΔE_b have a one-on-one mapping relation, and hence one can obtain the value of $g_{\uparrow\downarrow}$ through measuring ΔE_b.

In this section, we propose an experimental scheme to measure ΔE_b for the two-boson case. In the $\Omega < \Omega_c^{(1)}$ regime, we consider $|\Psi_g\rangle$ as an initial state perturbed by a harmonic trap with a periodically modulated trapping frequency $\omega(t) = \omega\left[1 - \alpha \sin\left(\omega_v t\right)\right]$, where ω is the original trap frequency, ω_v is the modulation frequency, and $\alpha \ll 1$. The time evolution of the two-boson state $|\Psi\left(t\right)\rangle$ is then determined by the Schrödinger equation

$$i\hbar\frac{\partial}{\partial t}\left|\Psi\left(t\right)\right\rangle = H_v\left(t\right)\left|\Psi\left(t\right)\right\rangle, \tag{2.30}$$

with the time-dependent Hamiltonian

$$H_v\left(t\right) = h_1^v\left(t\right) + h_2^v\left(t\right) + \hat{V}, \tag{2.31}$$

where $h_i^v(t)$ take the form of Eq. (2.1) with ω replaced by $\omega(t)$. We study the time evolution of the system by solving Eq. (2.30) using the Crank-Nicolson method.

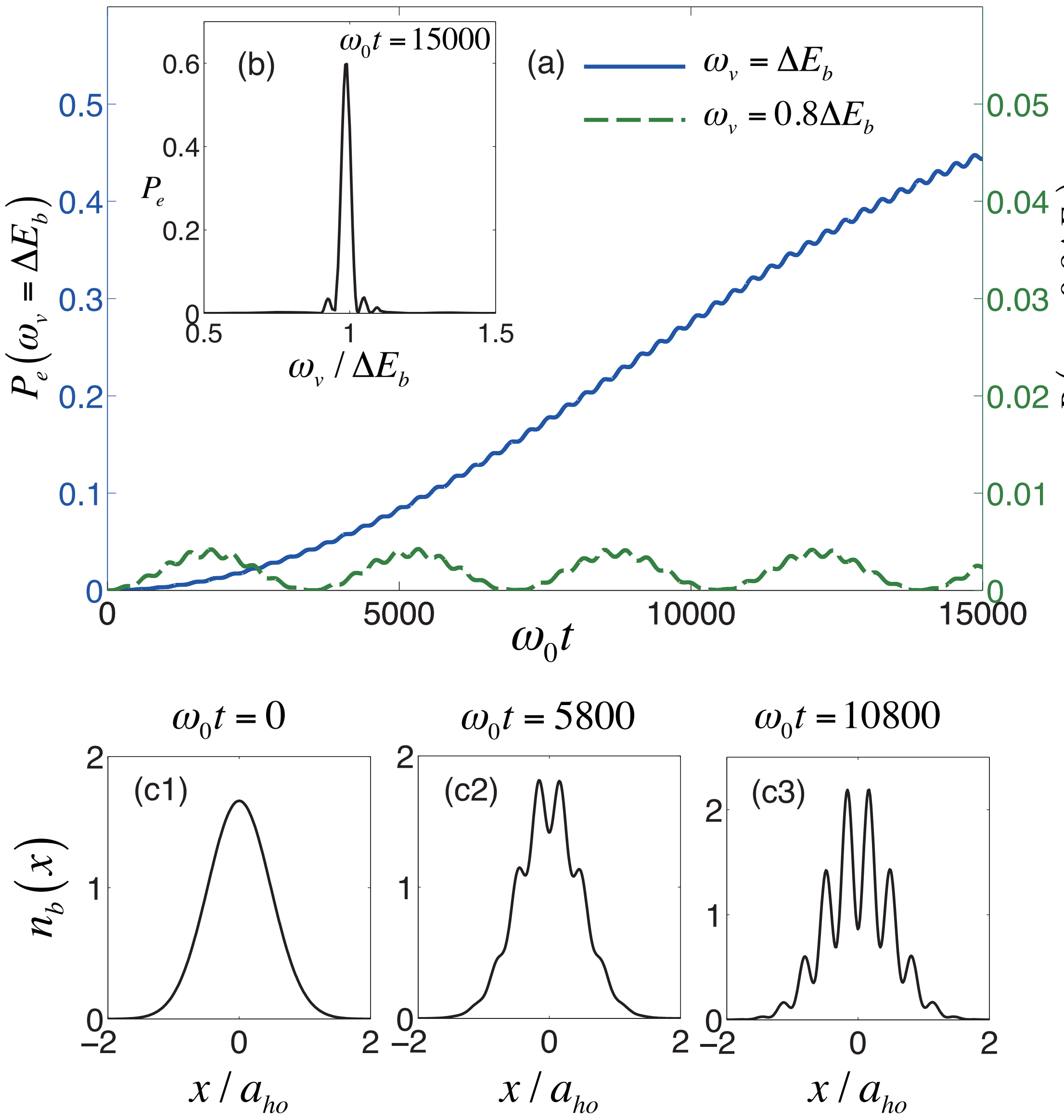

Figure 2.10 : Excitation of the two-boson ground state in a harmonic trap with periodically modulated trapping frequency $\omega\left[1-\alpha\sin\left(\omega_v t\right)\right]$. We fix $g_{\uparrow\downarrow} = 0.6g$, $\Omega = 80\hbar\omega_0$, $\omega = 2\omega_0$, $\alpha = 0.05$, and choose the two-boson ground state as the initial state. (a) Probability $P_e\left(t\right)$ on the first excited state for the on-(off-)resonance case with $\omega_v = \Delta E_b\left(0.8\Delta E_b\right)$, as a function of time t. (b) P_e as a function of ω_v when $\omega_0 t = 15000$. (c1)-(c3) Time evolution of the total density profile $n_b\left(x\right)$ for the on-resonance case with $\omega_v = \Delta E_b$.

The measurement of ΔE_b can be conducted by making use of the resonant excitation of the system. We investigate how periodic perturbations with various ω_v influence the probability $P_e\left(t\right)$ for the ground state to be excited to the first excited state. In the following discussion, we consider $g_{\uparrow\downarrow} = 0.6g$ and $\Omega = 80\hbar\omega_0$, and hence define $\Delta E_b \equiv \Delta E_b\left(\Omega = 80\hbar\omega_0\right)$. For an on-resonance modulation with $\omega_v = \Delta E_b$, we see in Fig. 2.10(a) a significant growth of P_e, whereas for an off-resonance modulation with $\omega_v = 0.8\Delta E_b$, P_e never exceeds 0.5%. We plot in Fig. 2.10(b) the excitation probability P_e as a function of the modulation frequency ω_v at $\omega_0 t = 15000$, where a typical resonance peak is clearly seen.

In order to visualize the above resonant excitation process, we examine the time evolution of the total density profile which is defined as $n_b\left(x\right) \equiv n_\uparrow^b\left(x\right) + n_\downarrow^b\left(x\right)$. For the on-resonance case with $\omega_v = \Delta E_b$, $n_b\left(x\right)$ develops a stripe pattern as a function of t, as shown in Figs. 2.10(c1)-(c3). The presence of this stripe pattern is because $\left|\Psi\left(t\right)\right\rangle_b$ becomes a superposition of the ground state $\left|\Psi_g\right\rangle$ and the first excited state during the time evolution. However, for off-resonant modulation, the system is almost unaffected by the periodic perturbation, and the stripe pattern is not present in $n_b\left(x\right)$.

Chapter 3

Spin-exchange-induced Spin-orbit Coupling in Cold-atom Spinor Mixtures

In the previous chapters, we have shown that spin-orbit (SO) coupled Bose-Einstein condensates (BEC) can host a stripe phase featuring spatially modulated density profiles [4, 17, 33–37], which can be regarded as a supersolid [38]; whereas SO coupled attractive Fermi gas can become a topological superfluid, supporting Majorana edge states [39–50].

However, the spatial period of the stripe phase is on the order of the optical wavelength, making its direct observation extremely challenging, although indirect evidences for the stripe phase have been reported in two seminal experiments [5, 51]. Another serious experimental problem for realizing SO coupling in quantum gas concerns the heating due to the Raman beams. The Raman-induced heating is particularly severe for atomic species with small fine-structure splitting [52]. Wei and Mueller carefully analyzed the heating problems for all alkali-metal atoms [52]. According to their analysis, ^{40}K and ^{6}Li — the two most commonly used fermionic species in cold atom experiments — suffer greatly from such heating. This could explain why an SO coupled fermionic superfluid, despite its tremendous theoretical interest, has yet to be realized in experiment.

Another research frontier in cold atoms is superfluid mixtures, a topic that has been studied in the context of superfluid ^3He-^4He mixtures in condensed-matter physics for many decades. In cold atoms, a Bose-Bose spinor mixture has been realized in a recent experiment, and the associated effects of spin-exchange interaction were observed [53] and theoretically analyzed [19]. In addition, several groups have created Bose-Fermi superfluid mixtures with scalar condensates [54–57].

The primary aim of this chapter is to demonstrate that the cold-atom mixture with spin-exchange interactions provides a unique platform to overcome the heating issue due to the Raman lasers, during the realization of the SO coupling. We consider a mixture of two species of spin-$1/2$ cold atoms, where only the first specie is subjected to the spin-orbit coupling induced by Raman beams. The second specie is not coupled by the Raman beams and hence immune from the Raman-induced heating. Our calculation shows that the second specie can acquire an effective spin-orbit coupling through the spin-exchange interaction between the two species. Therefore, we propose a promising way of obtaining spin-orbit coupled cold atoms without Raman-induced heating.

Besides achieving this primary aim, we also investigate other new and practical physics in the cold-atom spinor mixtures with spin-exchange interactions. In a Bose-Fermi mixture, we strikingly find that the presence of fermions can greatly increase the spatial period of the bosonic density stripes, and hence makes this phase directly observable in experiment. We also propose the realizations of topological Fermi superfluids and topological bands in this Bose-Fermi mixture. In a Bose-Bose mixture, we present a very rich phase diagram, with many of the phases not present in an SO-coupled single-species condensate.

Here, it needs to be explicitly stated that Sec. 3.1 is reprinted from Ref. [18] and Sec. 3.2 is reprinted from Ref. [19], except some minor add-ons, modifications and reorganizations.

3.1 Bose-Fermi Mixture with Spin-exchange-induced Exotic Superfluids

In the section, we consider a mixture of bosonic and fermionic superfluids, each of which is a spin-1/2 system. In addition to the density-density interactions, there exists an inter-species spin-exchange interaction. We assume that the condensate is subjected to the Raman-induced SO coupling, whereas the Fermi gas is not coupled by the Raman beams and hence is immune from the Raman-induced heating. The key observation of this section is that, through the spin-exchange interaction, the Fermi gas experiences a significant effective SO coupling. The interplay between the bosons and fermions leads to a variety of interesting quantum states, including a stripe phase in Bose condensate with the spatial period much larger than the optical wavelength, and topological Fermi superfluids and topological bands for fermions.

3.1.1 Hamiltonian

The total Hamiltonian of the system takes the form (we take $\hbar = 1$)

$$\mathbf{H} = \int dx \left(\Psi_B^\dagger h_B \Psi_B + \Psi_F^\dagger h_F \Psi_F \right) + \mathcal{G}_B + \mathcal{G}_F + \mathcal{G}_{BF}, \tag{3.1}$$

where $\Psi_B(x) = [\psi_{B\uparrow}(x), \psi_{B\downarrow}(x)]^{\mathrm{T}}$ represents the mean-field wave function of the BEC, and $\Psi_F(x) = [\psi_{F\uparrow}(x), \psi_{F\downarrow}(x)]^{\mathrm{T}}$ denotes the field operator of the Fermi gas. Both species have two internal spin states, which are labelled as ↑ and ↓. The single-particle Hamiltonians h_B and h_F are given by

$$h_B = \frac{(k - k_r\sigma_B^z)^2}{2m_B} + \frac{\Omega_B}{2}\sigma_B^x + \frac{\delta_B}{2}\sigma_B^z, \tag{3.2}$$

$$h_F = \frac{(k - k_r\sigma_F^z)^2}{2m_F} + \frac{\delta_F}{2}\sigma_F^z, \tag{3.3}$$

with Ω_B the Raman coupling strength, k_r the Raman recoil momentum, and $\sigma^x_{B,F}$ and $\sigma^z_{B,F}$ the Pauli matrices. We set the two-photon detuning $\delta_B = \delta_F = 0$ in our discussion. For simplicity, we assume a quasi-one dimensional system with strong transverse confinement. The key result that the fermions experience an effective SO coupling is insensitive to the dimensionality.

The last three terms in Eq. (3.1) describe three types of two-body interactions, where the Bose-Bose interactions read as

$$\mathcal{G}_B = \int dx \left[g^B \left(\rho^2_{B\uparrow} + \rho^2_{B\downarrow} \right) + 2g^B_{\uparrow\downarrow} \rho_{B\uparrow} \rho_{B\downarrow} \right], \tag{3.4}$$

with $\rho_{B\sigma} = \left| \psi_{B\sigma}(x) \right|^2$ the spin-σ density of the BEC, the Fermi-Fermi interaction takes the form

$$\mathcal{G}_F = g^F \int dx \, \psi^\dagger_{F\uparrow} \psi^\dagger_{F\downarrow} \psi_{F\downarrow} \psi_{F\uparrow}, \tag{3.5}$$

and the Bose-Fermi interactions are given by

$$\mathcal{G}_{BF} = \int dx \left[\gamma \rho_B \hat{\rho}_F + \beta \Big(\psi^*_{B\downarrow} \psi_{B\uparrow} \psi^\dagger_{F\uparrow} \psi_{F\downarrow} + h.c. \Big) \right], \tag{3.6}$$

where $\rho_B = \rho_{B\uparrow} + \rho_{B\downarrow}$ is the density of bosons, and $\hat{\rho}_F = \psi^\dagger_{F\uparrow} \psi_{F\uparrow} + \psi^\dagger_{F\downarrow} \psi_{F\downarrow}$ is the density operator for fermions. Here we have assumed that the inter-species density-density interactions are spin-independent, with a single interaction strength γ, to avoid the proliferation of parameters. The last term in Eq. (3.6) describes the inter-species spin-exchange interaction characterized by the strength β. We take L to be the length of the system with periodic boundary condition. The number of bosons and fermions are $N_{B,F}$, with the corresponding average densities $n_{B,F} = N_{B,F}/L$, respectively.

3.1.2 Non-interacting Fermions

Let us first consider the case with non-interacting fermions, i.e., $g^F = 0$. Previous studies of SO coupled BEC have shown that, in the absence of the fermions, the mean-field wave function of the condensate Ψ_B can be accurately described by the following ansatz:

$$\frac{\Psi_B}{\sqrt{n_B}} = \left[C_1 \begin{pmatrix} \cos\theta \\ -\sin\theta \end{pmatrix} e^{ik_B x} + C_2 \begin{pmatrix} \sin\theta \\ -\cos\theta \end{pmatrix} e^{-ik_B x} \right], \tag{3.7}$$

where k_B, θ, C_1 and C_2 are variational parameters. We can restrict $k_B \geq 0$ and $\theta \in [0, \pi]$ without loss of generality, and restrict C_1 and C_2 to be real positive numbers, with normalization condition $C_1^2 + C_2^2 = 1$, as the relative phase between them will not affect the total energy. Based on the values of the parameters, three phases of the SO coupled BEC can be identified: the stripe phase (ST) with $B \equiv C_1 C_2 \neq 0$ and $k_B \neq 0$ where the condensate density profile shows the stripe pattern; the plane-wave phase (PW) with $B = 0$ and $k_B \neq 0$ where the BEC condenses into a plane-wave state with finite spin polarization; and the zero-momentum phase (ZM) with $B = 0$ and $k_B = 0$ where the BEC features a smooth density profile with zero spin polarization. Given the variational ansatz (3.7), the BEC energy functional $\mathbf{E}_B\left(k_B, \theta, B\right)$, corresponding to $\int dx \Psi_B^* h_B \Psi_B + \mathcal{G}_B$, is given by

$$\begin{aligned} \frac{\mathbf{E}_B\left(k_B, \theta, B\right)}{N_B} =& \frac{k_B^2 + k_r^2 - 2k_r k_B \cos\left(2\theta\right)}{2m_B} - \frac{\Omega_B}{2}\sin\left(2\theta\right) \\ & - F(B)\cos^2\left(2\theta\right) + G_1\left(1 + 2B^2\right), \end{aligned} \tag{3.8}$$

where we have defined $F(B) = \left(2G_1 + 4G_2\right)B^2 - G_2$ and $G_{1,2} = n_B\left(g^B \pm g^B_{\uparrow\downarrow}\right)/2$.

The interplay between the condensate and the fermions is reflected in the $\mathcal{G}_{BF}$ term in Eq. (3.6). We include its effect in an effective fermionic single-particle Hamiltonian

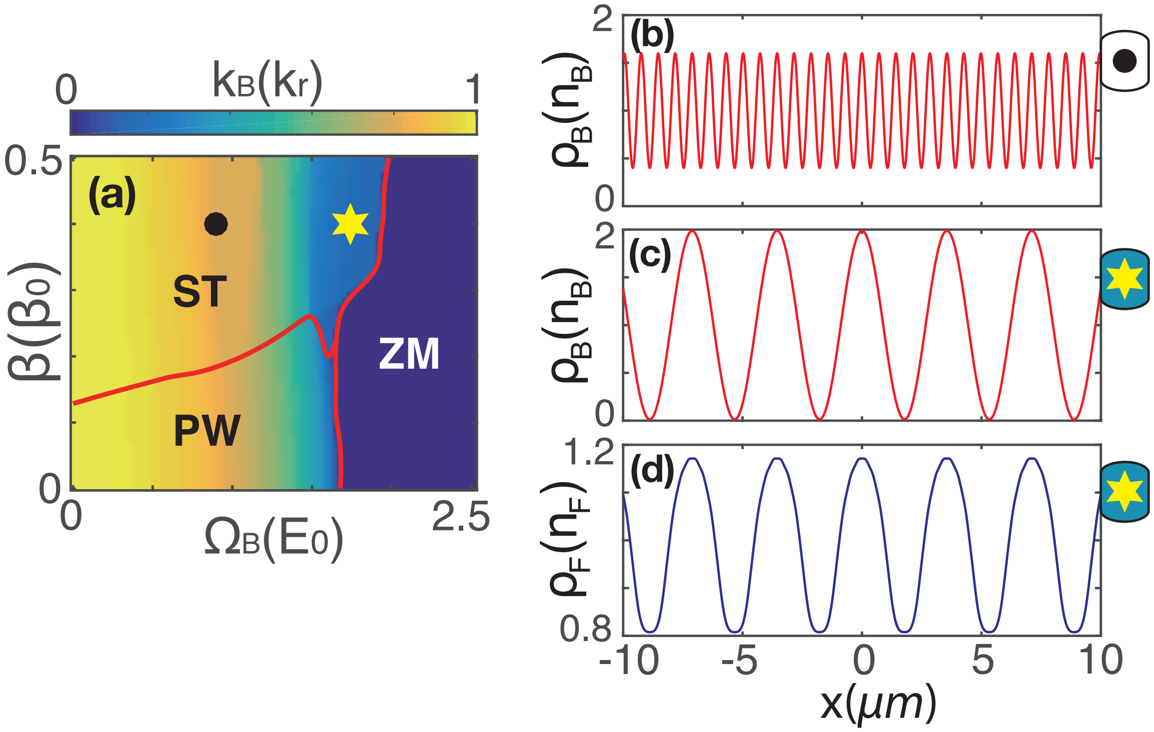

Figure 3.1 : (a) Phase diagram of the BEC characterizing the stripe (ST), plane-wave (PW), and zero-momentum (ZM) phases in the Ω_B-β plane with $\gamma = 0$, where the Fermi-Fermi interaction $g^F = 0$, the density of bosons $n_B = 10n_F$, and the background color displays the value of k_B/k_r. (b) The boson density profiles for the black dot in (a). (c) and (d) are, respectively, the boson and fermion density profiles for the yellow star in (a). The fermion number is set as $N_F = 2000$. The mass ratio is taken to be $m_B/m_F = 4$. We define the Fermi momentum $k_F = \pi n_F/2$ where $n_F = N_F/L$ is the total fermion density, and $\beta_0 = E_0/k_F$ where $E_0 = k_F^2/(2m_F)$. The Raman recoil momentum is taken to be $k_r = 5k_F/4$. The condensate interaction strengths are taken to be $g^B = 6.48 * 10^{-3} k_r/(2m_B)$ and $g^B_{\uparrow\downarrow} = 2g^B$. In (b)-(d), we set $k_r = \sqrt{2}\pi/(804.1\text{nm})$ to convert the length unit to μm.

h_F^{eff} defined as

$$\int dx\, \Psi_F^\dagger h_F^{\text{eff}} \Psi_F = \int dx \Psi_F^\dagger h_F \Psi_F + \mathcal{G}_{BF}\,. \tag{3.9}$$

Since Eq. (3.7) is quite general, we assume that the condensate wave function in the presence fermions can still be faithfully represented by Eq. (3.7). It follows that

$$h_F^{\text{eff}}\left(k_B,\theta,B\right) = \frac{\left(k - k_r\sigma_F^z\right)^2}{2m_F} + n_B \begin{pmatrix} \gamma V & -\beta M \\ -\beta M^* & \gamma V \end{pmatrix}, \tag{3.10}$$

where

$$M \equiv \frac{\sin\left(2\theta\right)}{2} + B\sin^2\theta e^{-2ik_Bx} + B\cos^2\theta e^{2ik_Bx}; \tag{3.11}$$

$$V \equiv 2B\sin\left(2\theta\right)\cos\left(2k_Bx\right) + 1. \tag{3.12}$$

The form of h_F^{eff} in Eq. (3.10) clearly shows that there is an effective SO coupling in the Fermi gas, which emerges from its interaction with the condensate. Since the two species influence each other, the SO coupling in both components possesses a dynamic nature. Dynamic synthetic gauge field has recently received much attention [11,58–60]. The spinor mixture system thus provides another platform where dynamic SO coupling emerges naturally.

Diagonalizing h_F^{eff} gives a set of fermionic single-particle states. Then the total energy of fermions $\mathbf{E}_F\left(k_B,\theta,B\right)$ is obtained by summing up the lowest N_F eigenenergies of h_F^{eff}. The ground state of the mixture is then obtained by minimizing the total energy functional $\mathbf{E}_B\left(k_B,\theta,B\right) + \mathbf{E}_F\left(k_B,\theta,B\right)$ with respect to the variational parameters. In our result, the final values of θ and k_B roughly keep the relation $\cos(2\theta) \approx k_B/k_r$.

This procedure allows us to present the phase diagram of condensate in the Ω_B-β parameter space as shown in Fig. 3.1(a), where we take $n_B = 10n_F$ and $N_F = 2000$. To isolate the effect of the inter-species interactions, we take the density-density interaction strength $\beta = 0$. In the absence of fermions, the condensate only possesses two phases, PW and ZM, for $g^B_{\uparrow\downarrow} > g^B$. The transition between them occurs around $\Omega_B = 4k_r^2/(2m_B)$. A notable feature of Fig 3.1(a) is that the region with large β is dominated by the ST phase. This feature is clearly induced by the fermions. Specifically, the spin-exchange interaction induces an attractive interaction between the two spin components of the condensate, leading to a reduced effective $g^B_{\uparrow\downarrow}$, which favors the ST phase. The background color in Fig. 3.1(a) displays the value of k_B. In the ST phase, the condensate density profile is given by

$$\rho_B\left(x\right) = n_B\left[1 + \sin\left(2\theta\right)\cos\left(2k_B x\right)\right], \tag{3.13}$$

with a density modulation whose spatial period is determined by $1/k_B$. One can see that, for a given β, k_B decreases as Ω_B increases. Figure 3.1(b) and (c) show two condensate density profiles corresponding to the black dot and yellow solid star in (a), respectively. For realistic parameters, the ST phase can possess a spatial period of several microns and a large modulation depth. Such a state can be readily observed using *in situ* imaging with today's technology. The density profile for the Fermi gas, corresponding to the yellow solid star, is shown in (d). The two density profiles in (c) and (d) exhibit in-phase modulations.

Let us now turn to a more in-depth discussion of the properties of fermions in the mixture. When the condensate is in the PW or the ZM phase, we have $B = 0$, and the effective single-particle Hamiltonian for fermions h_F^{eff} in Eq. (3.10) is reduced to (after neglecting a term proportional to the constant n_B)

$$h^{\text{eff}}_{\text{F,PW}} = \frac{\left(k - k_r\sigma_F^z\right)^2}{2m_F} + \frac{\Omega_F^{\text{eff}}}{2}\sigma_F^x, \tag{3.14}$$

which has the same form as the Hamiltonian of an SO coupled Fermi gas, only that here the SO coupling is not due directly to the Raman lasers, but to the inter-species

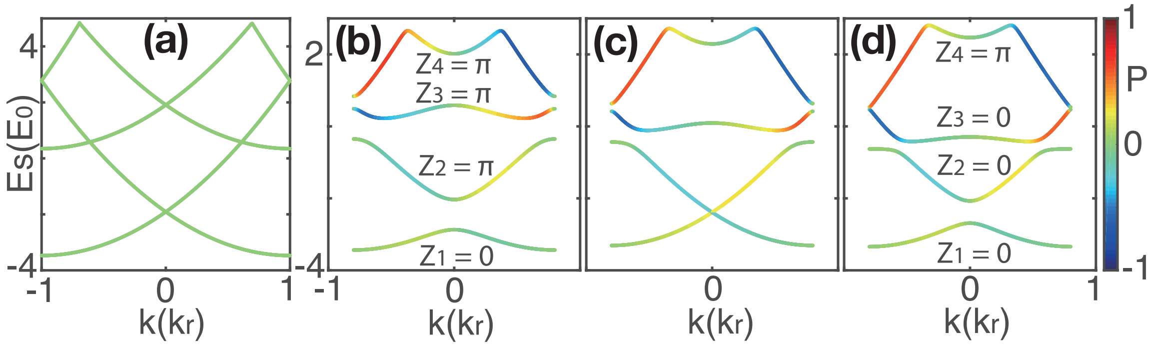

Figure 3.2 : The lowest four energy bands of the non-interacting fermions with $g^F = 0$, when the condensate is in the ST phase. Here $\beta = 0.6\beta_0$ in all plots. In (a), $\Omega_B = 0$ and $\gamma = 0$. For the rest of the plots, $\Omega_B = E_0$, and $\gamma = 0$ (b), $\gamma = 0.23\gamma_0$ (c), and $\gamma = 0.4\gamma_0$ (d). The Zak phase for each band is indicated in (b) and (d). The color of the curve denotes the spin polarization $P = \langle \sigma_F^z \rangle$. The other parameters are the same as those in Fig. 3.1.

spin-exchange interaction with an effective Raman coupling strength given by

$$\Omega_F^{\text{eff}} = -\beta n_B \sin(2\theta)\,. \tag{3.15}$$

When the condensate is in the ST phase, we have $B = 1/2$, both V and M in Eq. (3.10) exhibit spatial modulations, originated from the density modulation of the condensate. The V-term, arising from the inter-species density-density interaction, serves as a lattice potential for the fermions, while the M-term, from the spin-exchange interaction, can be regarded as a periodic Raman coupling for the two spin components of the fermions. This situation is analogous to the optical Raman lattice proposed by Liu *et al.* [46,61], and realized in recent experiments [39]. In the Raman lattice setup, the atom experiences an optical lattice potential and a periodic Raman coupling, both originated from the same laser beams. It is shown that the system parameters can be adjusted and induce topological phase transitions. Drawing from this analogy, we also expect topological phases in our system. Figure 3.2 displays the lowest four energy bands E_s of the effective fermionic single-particle Hamiltonian h_F^{eff} in Eq. (3.10), when the condensate is in the ST phase. In all the plots in Fig. 3.2, we fix the value of β. Figure 3.2(a) is a reference plot where $\Omega_B = 0$, hence there is no SO coupling in the system. Here different bands cross each other. The remaining three plots correspond to the same finite value of Ω_B, with varying γ. In these cases, gaps open up at band crossing points in (a). The color of each band represents the spin polarization $P = \langle \sigma_F^z \rangle$, which can be seen to be momentum-dependent — a manifestation of the SO coupling. The values of Z_j, indicated in (b) and (d), are the Zak phase for each band, defined as [62]

$$e^{iZ_j} = \prod_{a=-d}^{d} w_j^* \left(k_a\right) \cdot w_j \left(k_{a+1}\right), \tag{3.16}$$

where $w_j\left(k_a\right)$ is the eigenstate of band j and discretized momentum k_a, restricted in the first Brillouin zone in the range $k_a \in [-k_B, k_B)$, with the additional constraint $w_j\left(k_{d+1}\right) = w_j\left(k_{-d}\right)$ to form a loop in the calculation of the Zak phase. At a critical value of γ shown in Fig. 3.2(c), the lowest two bands crosses each other. When the band reopens at a larger value of γ, the Zak phase of some of the bands changes its value. Thus the closing and the reopening of the band gap signals a topological transition. Note that Zak phase in topological Bloch bands has been measured in recent cold atom experiments [63].

3.1.3 Interacting Fermions

Now let us turn to the situation where the fermions are self-interacting with an attractive s-wave interaction strength $g^F = -6k_F/\left(\pi m_F\right)$ in Eq. (3.5), which can lead to superfluid pairing. Including Fermi-Fermi interaction greatly complicates the physics in the ST phase. To keep things relatively simple, we take a large boson density $n_B = 500n_F$, such that in the parameter space we will explore, the bosons are nearly unaffected by the fermions and remain in either the PW or the ZM phase. Under this situation, the effective fermionic single-particle Hamiltonian is given by $h^{\text{eff}}_{\text{F,PW}}$ in Eq. (3.14). We thus have a system of attractive Fermi gas subjected to SO coupling with an effective Raman coupling strength Ω^{eff}_F defined in Eq. (3.15). The corresponding fermionic system has been studied before [44] and is known to support topological superfluid phase. This can be intuitively understood as follows. The SO coupling mixes spin singlet and triplet pairings. The Raman term, which can be regarded as an effective Zeeman field, tends to weaken the singlet pairing. For sufficiently large Ω^{eff}_F, the singlet pairing is suppressed, and the Fermi gas becomes a topological superfluid with effective p-wave pairing. This picture is indeed confirmed by our calculation.

Our calculation proceeds as follows. The bosonic contribution to the total energy functional $\mathbf{E}_B\left(k_B, \theta, B\right)$ still takes the form of Eq. (3.8), only that the parameter B vanishes for the PW and the ZM phase. For the fermionic part, the thermodynamic grand potential can be written as

$$\mathbf{P}_F\left(\mu, \theta\right) = \int dx \Psi^\dagger_F \left(h^{\text{eff}}_{\text{F,PW}} - \mu\right) \Psi_F + \mathcal{G}_F, \tag{3.17}$$

where μ is the chemical potential, and $h^{\text{eff}}_{\text{F,PW}}$ and $\mathcal{G}_F$ are defined by Eqs. (3.14) and (3.5), respectively. Note that $h^{\text{eff}}_{\text{F,PW}}$ is a function of the variational parameter θ. In our treatment of the fermionic part, we follow the standard mean-field approach introduced for the single-species interacting fermions as reported in, e.g., Refs [44,49]. In the mean-field approximation, the Fermi-Fermi interaction term becomes

$$\mathcal{G}_F = -\Delta \left[\psi^\dagger_{F\uparrow}\left(x\right) \psi^\dagger_{F\downarrow}\left(x\right) + \text{h.c.}\right] - \Delta^2 / g^F, \tag{3.18}$$

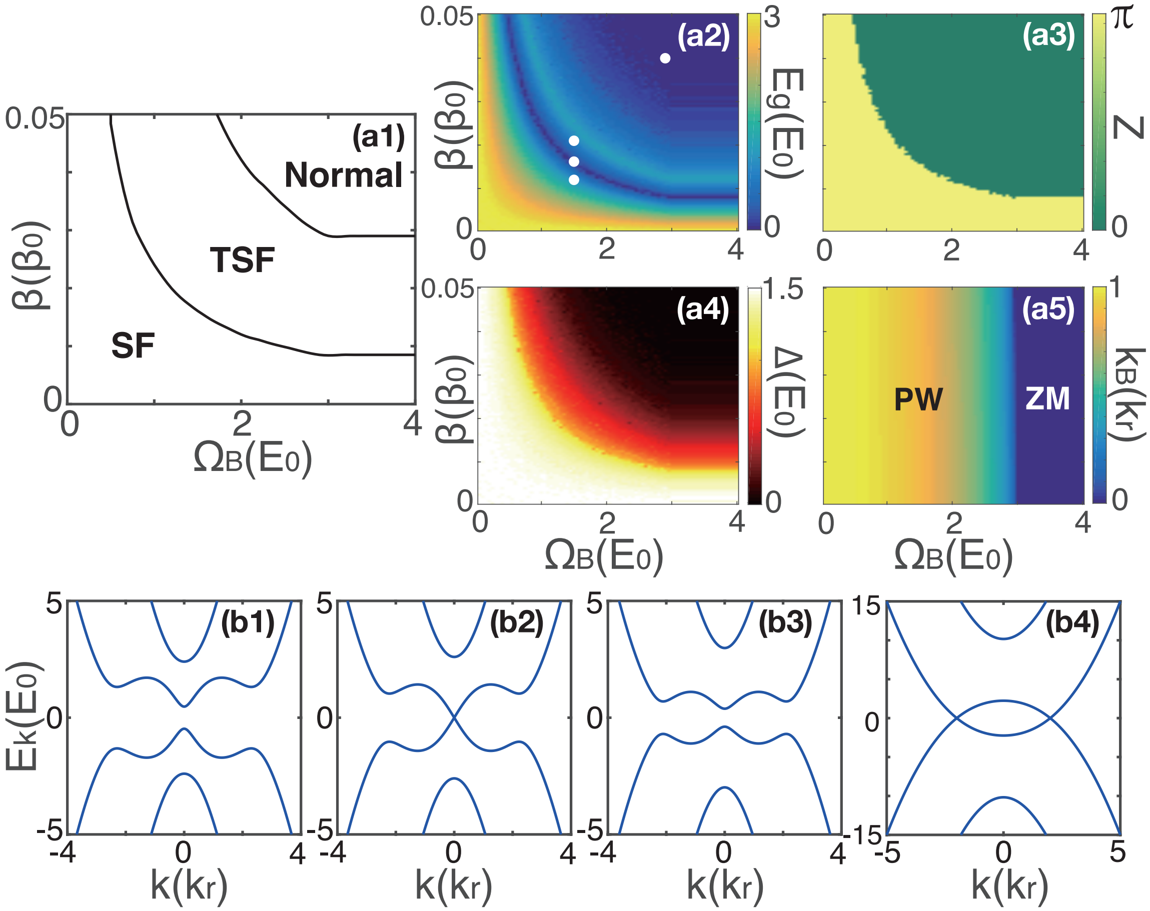

Figure 3.3 : (a1) The phase diagram of the fermions identifying the superfluid (SF), topological superfluid (TSF), and normal phases in the Ω_B-β parameter space with attractive Fermi-Fermi interaction strength $g^F = -6k_F/(\pi m_F)$ and $n_B = 500n_F$. In the same parameter space, we also plot: (a2) the quasi-particle excitation gap E_g; (a3) the winding number Z; (a4) the Fermi superfluid order parameter Δ; and (a5) the variational momentum k_B of the condensate. The four excitation spectra E_k corresponding to the 4 red dots in (a2), from bottom to top, are plotted in (b1) - (b4), respectively. We take $N_F = 800$. The other parameters are the same as those in Fig. 3.1.

where the superfluid order parameter is defined as

$$\Delta = -g^F \left\langle \psi_{F\downarrow}(x)\, \psi_{F\uparrow}(x) \right\rangle .$$

In momentum space, the grand potential can be re-written as

$$\mathbf{P}_F(\mu, \theta, \Delta) = \frac{1}{2} \sum_k C_k^\dagger M_k C_k + \sum_k \xi_k - \frac{L\Delta^2}{g^F}, \tag{3.19}$$

where $C_k^\dagger = \begin{bmatrix} c_{k\uparrow}^\dagger & c_{k\downarrow}^\dagger & c_{-k\uparrow} & c_{-k\downarrow} \end{bmatrix}$ and

$$M_k = \begin{bmatrix} \xi_k + \lambda k & \Omega_{\mathrm{F}}^{\mathrm{eff}}/2 & 0 & -\Delta \\ \Omega_{\mathrm{F}}^{\mathrm{eff}}/2 & \xi_k - \lambda k & \Delta & 0 \\ 0 & \Delta & -\xi_k + \lambda k & -\Omega_{\mathrm{F}}^{\mathrm{eff}}/2 \\ -\Delta & 0 & -\Omega_{\mathrm{F}}^{\mathrm{eff}}/2 & -\xi_k - \lambda k \end{bmatrix}, \tag{3.20}$$

with $\xi_k = k^2/(2m_F) - \mu$ and $\lambda = -k_r/m_F$. Diagonalizing the matrix M_k, we can further transform the grand potential to the following form:

$$\begin{aligned} \mathbf{P}_F(\mu, \theta, \Delta) = \frac{1}{2} \sum_k (&E_{k1}\alpha_{k1}^\dagger \alpha_{k1} + E_{k2}\alpha_{k2}^\dagger \alpha_{k2} \\ &+ E_{k3}\alpha_{k3}\alpha_{k3}^\dagger + E_{k4}\alpha_{k4}\alpha_{k4}^\dagger) + \sum_k \xi_k - \frac{L\Delta^2}{g^F}, \end{aligned} \tag{3.21}$$

where α_{k1}, α_{k2}, α_{k3}, and α_{k4} are quasi-particle elementary excitation operators with the symmetry $E_{k4} = -E_{-k1}$ and $E_{k3} = -E_{-k2}$. The two positive excitation branches are given by

$$E_{k1,2} = \left(\xi_k^2 + \eta_k + \Delta^2 \pm \sqrt{4\eta_k \xi_k^2 + \left(\Omega_{\mathrm{F}}^{\mathrm{eff}}\right)^2 \Delta^2} \right)^{\frac{1}{2}}, \tag{3.22}$$

with $\eta_k = (k_r k/m_F)^2 + \left(\Omega_{\mathrm{F}}^{\mathrm{eff}}\right)^2/4$. The ground state of the fermions is considered to be the quasi-particle vacuum, with the corresponding ground-state grand potential given by

$$\mathbf{P}_F(\mu, \theta, \Delta) = -\frac{1}{2} \sum_k (E_{k1} + E_{k2}) + \sum_k \xi_k - \frac{L\Delta^2}{g^F}, \tag{3.23}$$

where the anti-commutation relations of α_{k1}, α_{k2}, α_{k3}, and α_{k4} have been considered. Note that $\mathbf{P}_F(\mu,\theta,\Delta)$ is a functional of three undetermined variational parameters μ, θ, and Δ.

The ground state of the whole mixture is obtained through the minimization of $\mathbf{E}_B(k_B,\theta,0)+\mathbf{P}_F(\mu,\theta,\Delta)$ with respect to the variational parameters k_B, θ, and Δ, where the constraint $N_F=-\partial\mathbf{P}_F(\mu,\theta,\Delta)/\partial\mu$ is imposed to fix the number of fermions. Actually, the minimization of $\mathbf{E}_B(k_B,\theta,0)$ with respect to k_B leads to the rigorous relation $\cos(2\theta)=k_B/k_r$, and hence we only need to deal with θ and Δ in the numerical minimization. The converged results of k_B, θ, Δ, and μ are obtained in the thermodynamic limit with $N_B,N_F,L\to\infty$ while keeping $n_B=N_B/L$ and $n_F=N_F/L$ finite.

Our results are summarized as follows. Figure 3.3(a1) represents the zero temperature phase diagram of the Fermi gas in the Ω_B-β space. It shows three phases: the non-topological superfluid (SF), the topological superfluid (TSF), and the normal phase. The first two phases feature finite superfluid order parameter Δ, whereas Δ vanishes in the normal phase, as shown in Fig. 3.3(a4). The quasi-particle excitation gap E_g is finite in the SF and the TSP phases, except at the boundary of these two phases, as shown in Fig. 3.3(a2), where E_g vanishes as expected for topological phase transition. Several examples of the quasi-particle excitation spectra E_k at various phases are displayed in Fig. 3.3(b1)∼(b4).

The topological phase transition can be further confirmed by the winding number Z, which is defined through a loop connecting the two positive excitation branches at infinitely large k, and can be calculated as [49]

$$e^{iZ}=\prod_{a=-b}^{b}\left[w_1^*(k_a)\cdot w_1(k_{a+1})\right]\left[w_2^*(k_a)\cdot w_2(k_{a+1})\right], \tag{3.24}$$

where $w_1(k_a)$ and $w_2(k_a)$ are the quasiparticle eigenstates corresponding to the two positive excitation branches E_{k1} and E_{k2} in Eq. (3.22), with the quasi-momentum defined as $k_a = 2\pi a/L$ with the integer $a \in [-b, b]$ where b is a sufficiently large numerical cut-off. We define $w_1(k_{b+1}) = w_2(k_{-b})$ and $w_2(k_{b+1}) = w_1(k_{-b})$ to connect the two positive excitation branches and form the loop in calculating the winding number. Note that here k_a in (3.24) is no longer restricted in the first Brillouin zone. As shown in Fig. 3.3(a3), Z jumps from π to 0 when entering from SF to TSF. Finally, through combining the result of k_B in Fig. 3.3(a5), the definition of Ω_F^{eff} in Eq. (3.15), and the relation $\cos(2\theta) = k_B/k_r$, we can see that the TSF phase does correspond to the larger Ω_F^{eff}, and hence our result agrees with our previous picture.

3.2 Bose-Bose Mixture with Spin-exchange-induced Novel Phase Diagrams

In this section, we consider a two-species spinor BEC [1620] and investigate the effects of SO coupling in such a system. More specifically, each species in our study represents a spin-1/2 condensate, as produced in a recent experiment [21]. One of the species is subjected to a Raman-induced SO coupling [1,2224], whereas the other species is not directly coupled to the Raman beams. We show that the latter species acquires an effective SO coupling due to the spin-exchange interaction between the two. Similar to the Bose-Fermi mixture discussed in the previous section, such spin-exchange-induced SO coupling may overcome the heating problem suffered by certain atomic species when subjected to Raman beams. Significantly, this Bose-Bose mixture system displays a very rich phase diagram, with many of the phases not present in an SO-coupled single-species condensate.

3.2.1 Hamiltonian

— We consider the Raman SO-coupling scheme [3, 4, 34] onto each species (species A and B) in our dual-species bosonic mixture, where the two Raman beams conter-propagate along x axis carrying opposite optical momentum $\pm\hbar k_L$, as schematically shown in Fig. 3.4(a). The relevant atomic energy level structure of each species is shown in Fig. 3.4(b). Due to the large single-photon detuning, the upper energy level can be adiabatically eliminated, and as a result under the rotating approximation and mean field framework, the total energy functional of the system reads (we set $\hbar = 1$)

$$E\left(\mathbf{\Psi}_A, \mathbf{\Psi}_B\right) = \sum_{i=A,B} \int dx \mathbf{\Psi}_i^\dagger h_i \mathbf{\Psi}_i + \sum_{i=A,B} \mathcal{G}_i + \mathcal{G}_{AB}, \tag{3.25}$$

where $\mathbf{\Psi}_i = \left(\psi_{i,\uparrow}, \psi_{i,\downarrow}\right)^T$ represents the spinor wave function satisfying $\int dx \left|\mathbf{\Psi}_i\right|^2 = N_i$ with N_i being the total particle number of species i ($i = A$ or B), and

$$h_i = \frac{k_i^2}{2m_i} + \frac{\delta_i}{2}\sigma_z^i + \frac{\Omega_i}{2}\begin{pmatrix} 0 & e^{-2ik_L x_i} \\ e^{2ik_L x_i} & 0 \end{pmatrix} + V_{ext}^i\left(x_i\right) \tag{3.26}$$

is the single-particle Hamiltonian where δ_i denotes the two-photon detuning, $V_{ext}^i\left(x_i\right)$ depicts the external potential, k_L is the recoil momentum associated with the Raman process, and $\Omega_i = \Omega_1^i\Omega_2^i/2\Delta_i$ characterizes the two-photon Raman coupling strength with Δ_i being the single-photon detuning of the species i. Note that in the Hamiltonian (3.26) we only keep the spatial terms along the direction of x, because the perpendicular terms (in y-z plane) are decoupled with h_i. From an experimental point of view, the spin-1/2 BEC mixture can be reduced from a spin-1 mixture with large quadratic Zeeman splittings. In this work, we assume the either species is on a two-photon resonance with $\delta_i = 0$, and only focus on the situation with $\Omega_B \approx 0$ which can be simply realized, for instance, by properly adjusting the frequencies of Raman beams satisfying $\Delta_B \gg \Delta_A$, as shown in Fig. 3.4(b).

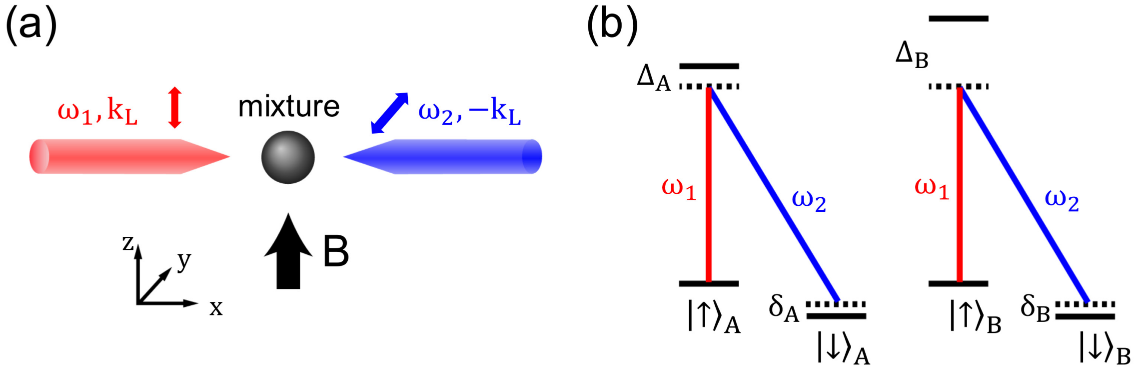

Figure 3.4 : (a) Schematic representation of the dual-species BECs system. (b) Atomic level structure for either species.

The last two terms in Eq. (3.25) characterize two different types of two-body interactions, interaspecies or homonuclear interaction $\mathcal{G}_i$ and interspecies or heteronuclear interactions $\mathcal{G}_{AB}$. The former is in a form of $\mathcal{G}_i = \int dx \left[g^i\left(\rho_{i,\uparrow}^2 + \rho_{i,\downarrow}^2\right) + g_{\uparrow\downarrow}^i \rho_{i,\uparrow}\rho_{i,\downarrow}\right]$ where $\rho_{i,\sigma} = |\psi_{i,\sigma}|^2$ denotes the spinor density with respect to the species i, and $g_{\sigma\sigma'}^i = 4\pi a_{\sigma\sigma'}^i/m_i$ with $a_{\sigma\sigma'}^i$ being s-wave scattering length in different spin channels and assumed to be always repulsive $a_{\sigma\sigma'}^i > 0$ in this work. On the other hand, the heteronuclear interaction has a form of

$$\begin{aligned}\mathcal{G}_{AB} = \int dV\, [&\gamma\left(\rho_{A,\uparrow}\rho_{B,\uparrow} + \rho_{A,\downarrow}\rho_{B,\downarrow}\right) \\ &+ \alpha\left(\rho_{A,\uparrow}\rho_{B,\downarrow} + \rho_{A,\downarrow}\rho_{B,\uparrow}\right) \\ &+\beta\left(\psi_{A,\uparrow}^*\psi_{B,\downarrow}^*\psi_{B,\uparrow}\psi_{A,\downarrow} + \psi_{A,\downarrow}^*\psi_{B,\uparrow}^*\psi_{B,\downarrow}\psi_{A,\uparrow}\right)]\,,\end{aligned} \tag{3.27}$$

where interaction strengths are defined as $\alpha, \beta, \gamma \equiv 2\pi a_{\alpha,\beta,\gamma}/m_\mu$ with

$$m_\mu \equiv m_A m_B/(m_A + m_B) \tag{3.28}$$

being the reduced mass. Apparently, the first two terms of Eq. (3.27) can be rewritten into a compact form of $(\gamma+\alpha)\rho_A\rho_B/2 + (\gamma-\alpha)F_z^A F_z^B/2$ with $F_{l=x,y,z}^i = \vec{\Psi}_i^\dagger \sigma_l^i \vec{\Psi}_i$

being the spinor spin density operator. In the case of $\alpha = \gamma$ and $\beta = 0$, $\mathcal{G}_{AB}$ only contains a simple density-density interaction term that commonly appeared in a dual-species scalar BEC mixture. At the Thomas-Fermi limit, $\gamma_C = \sqrt{g^A g^B}$ is the critical point of phase separation of the two species [64]. Hence, in order to explore the mutual influence of the two species, we only focus on a miscible configuration by setting $0 < \alpha = \gamma < \sqrt{g^A g^B}$ in our following calculation. In particular, the β interaction term in Eq. (3.27) describes a interspecies spin-exchange process where two distinguishable particles exchange spin states after the two-body collision. Note that the sign of β only determines the same or reversed alignment of spins of two species along x direction but has no influence on ground-state energy, and hence we only focus on the case of $\beta > 0$.

We apply a gauge transformation $U_i = e^{ik_L x_i \sigma_z^i}$ for each species in the system. In the rotating frame, the spinor wave function becomes $\tilde{\mathbf{\Psi}}_i = U_i \mathbf{\Psi}_i$ and the single-particle Hamiltonian $\tilde{h}_i = U_i h_i U_i^\dagger$ has a form of

$$\tilde{h}_A = \frac{\left(k_A - k_L \sigma_z^A\right)^2}{2m_A} + \frac{\Omega_A}{2}\sigma_x^A + V_{ext}^A\left(x_A\right), \tag{3.29}$$

and

$$\tilde{h}_B = \frac{\left(k_B - k_L \sigma_z^B\right)^2}{2m_B} + V_{ext}^B\left(x_B\right), \tag{3.30}$$

where we already set $\Omega_B = 0$ and a finite Ω_A. Note that the unitary transformation towards species B is necessary here, since it eliminates the new phase factor generated by $\tilde{\mathbf{\Psi}}_A$ in the β term, and finally remains the form of heteronuclear interaction unchanged in rotating frame, i.e. $\tilde{\mathcal{G}}_{AB} = \mathcal{G}_{AB}$. Although there is no Raman coupling in the single-particle Hamiltonian $\tilde{h}_B$ in Eq. (3.30), the β interaction term acts like a transverse magnetic field coupling of two inner spin states, and as a result induces an effective SO coupling for species B, which is the key point of our work.

In the following, we will make detailed discussions on two different parametric cases: $N_A \gg N_B$ and $N_A = N_B$. Moreover, for simplicity, our discussions will be only in the rotating framework, and hence all the tildes symbols can be neglected without any confusion.

3.2.2 Case of $N_A \gg N_B$

As a good approximation, we can ignore the influence from species B to species A, and meanwhile only consider the vise action. In this case, the species A is isolated, and A's physical properties can be well depicted by the variational method in a homogenous system ($V_{ext}^{A} = 0$) [4], where the ground-state wave function can be described by the ansätz:

$$\mathbf{\Psi}_A = \sqrt{\rho_A}\left[C_+ \begin{pmatrix} \cos\theta_A \\ -\sin\theta_A \end{pmatrix} e^{i\kappa_A x_A} + C_- \begin{pmatrix} \sin\theta_A \\ -\cos\theta_A \end{pmatrix} e^{-i\kappa_A x_A}\right], \tag{3.31}$$

where ρ_A denotes the average density of the homogeneous system, and $C_\pm$, θ_A, and κ_A are the variational parameters with $|C_+|^2 + |C_-|^2 = 1$. The minimization of the single-particle energy $\int dx \mathbf{\Psi}_A^\dagger h_A \mathbf{\Psi}_A$ with respect to θ_A yields the relation $\theta_A = \arccos\left(\kappa_A/k_L\right)/2$ with $0 \le \theta_A \le \pi/4$. In the condition $g_{\uparrow\downarrow}^{A} < g^A$, the minimization of the single-particle energy respect to κ_A and $C_\pm$ ensures three phases: (i) Stripe (ST) phase in $\Omega_A < \Omega_A^{S-P}$ where the species A condenses in a superposition of the two plane wave states with momentums κ_A and $-\kappa_A$ and thus $|C_+| = |C_-|$ and $\kappa_A \neq 0$; (ii) Plane wave (PW) phase in $\Omega_A^{S-P} < \Omega_A < \Omega_A^{P-Z}$ where the species A condenses in a single plane wave state with the momentum κ_A or $-\kappa_A$ and thus $|C_+||C_-| = 0$ and $\kappa_A \neq 0$; (iii) Zero-momentum (ZM) phase in $\Omega_A > \Omega_A^{P-Z}$ where the species A condenses in a zero-momentum state and thus $|C_+||C_-| = 0$ and $\kappa_A = 0$. Here Ω_A^{S-P} and Ω_A^{P-Z} are phase boundaries between three phases.

By substituting $\boldsymbol{\Psi}_A$ in Eq. (3.31) into $\mathcal{G}_{AB}$ in Eq. (3.27), one can see the influence from A to B. Now, the species B is with an effective single particle Hamiltonian $h_{B,eff}$. When species A is in PW or ZM phase, $h_{B,eff}$ takes the form

$$h_{B,eff} = \frac{\left(k_{B,x} - k_L \sigma_z^B\right)^2}{2m_B} + \frac{\Omega_B}{2}\sigma_x^B, \tag{3.32}$$

where

$$\Omega_B = -\beta n_A \sin 2\theta_A. \tag{3.33}$$

Note that, as expected, the β interaction now provides transverse magnetic field coherently coupling the two spin states of species B. Then, we can redo the whole discussions of species A on B by simply assuming B's ground-state wave function as

$$\boldsymbol{\Psi}_B = \sqrt{\rho_B}\left[D_+ \begin{pmatrix} \cos\theta_B \\ \sin\theta_B \end{pmatrix} e^{i\kappa_B x_B} + D_- \begin{pmatrix} \sin\theta_B \\ \cos\theta_B \end{pmatrix} e^{-i\kappa_B x_B}\right], \tag{3.34}$$

where $D_\pm$, θ_B, and κ_B are the variational parameters determined by the minimization of $\int dx \boldsymbol{\Psi}_B^\dagger h_{B,eff} \boldsymbol{\Psi}_B$. In the condition $g_{\uparrow\downarrow}^B < g^B$, species B also has three quantum phases: $\mathcal{ST}$, $\mathcal{PW}$ and $\mathcal{ZM}$. The corresponding phase boundaries can be obtained in terms of β as

$$\beta_B^{S-P} = \frac{1}{n_A \sin 2\theta_A} \frac{4G_-^B\left(k_L^2 + G_+^B\right)\left(k_L^2 - 2G_-^B\right)}{\left(G_+^B + 2G_-^B\right)}, \tag{3.35}$$

and

$$\beta_B^{P-Z} = \frac{2\left(k_L^2 - 2G_-^B\right)}{n_A \sin 2\theta_A}, \tag{3.36}$$

where the homonuclear interactions parameters of the species B are defined as $G_\pm^B = \rho_B\left(g^B \pm g_{\uparrow\downarrow}^B\right)/4$. Note that the $\sin 2\theta_A$ in Eqs. (3.35) and (3.36) is pre-determined in the species-A ground state as a function of Ω_A and other parameters of the species A.

When the species A is in the ST phase, the effective Hamiltonian $h_{B,eff}$ becomes

$$h_{B,eff} = \frac{\left(k_B - k_L \sigma_z^B\right)^2}{2m_B} + h_B', \tag{3.37}$$

where

$$h'_B = \rho_A \left[1 + \sin 2\theta_A \cos\left(2\kappa_A x_B\right)\right] \begin{pmatrix} \gamma & -\frac{\beta e^{i\phi(x_B)}}{2} \\ -\frac{\beta e^{-i\phi(x_B)}}{2} & \gamma \end{pmatrix}, \tag{3.38}$$

with the help of the relationship

$$\frac{\left|\sin 2\theta_A + 2\cos\left(2\kappa_A x_B\right)\sin^2\theta_A + e^{\pm 2i\kappa_A x_B}\right|^2}{\left[1 + \sin 2\theta_A \cos\left(2\kappa_A x_B\right)\right]^2} = 1. \tag{3.39}$$

Here, $\phi\left(x_B\right)$ denotes the relative phase factor between the diagonal and off-diagonal element in h'_B. In particular, when $\theta_A = \pi/4$, we have $\phi(x_B) = 0$, and the species B is like being placed into an atomic lattice with a coordinate relevant spin flipping in a period of κ_A/π. As for the more general case with $\theta_A \in (0, \pi/4)$, though it is hard for us to further reduce the express Eq. (3.38), one need to notice that the matrix in Eq. (3.38) has two eigenvalues $\gamma \pm \beta/2$. Further, the $\gamma - \beta/2$ is the lowest band since $\beta > 0$, and the point $\beta = 2\gamma$ indicates a phase transition. Specifically, when $\beta < 2\gamma$, in order to minimize the total energy, the stripe of species B would oscillate out-of-phase with that of species A. On the contrary when $\beta < 2\gamma$, the stripes of A and B would be in-phase.

As a comparison to our above analytical discussion in the $N_A \gg N_B$ limit, we carry out a direct numerical result by solving the mean-field Gross-Pitaevskii (GP) equations corresponding to the total energy functional of the whole mixture system in Eq. (3.1). We get the ground-state wave function $\psi_{i,\sigma}$ by evoluting the GP equations in imaginary time. Fig. 3.5(a) shows the ground-state phase diagram where 10 different phases are observed and classified. Each phase is symboled by a combination of the conditions of two species. In the meanwhile, the corresponding density profile of each phase is shown in Fig. 3.5(b). In our calculation, we take species A as ^{23}Na with homonuclear $a^A = 50a_B$ and $N_A = 2.5 \times 10^4$, while species B as ^{87}Rb with $a^B = 100a_B$ and $N_B = 1 \times 10^3$. Moreover, two species are confined in boxed

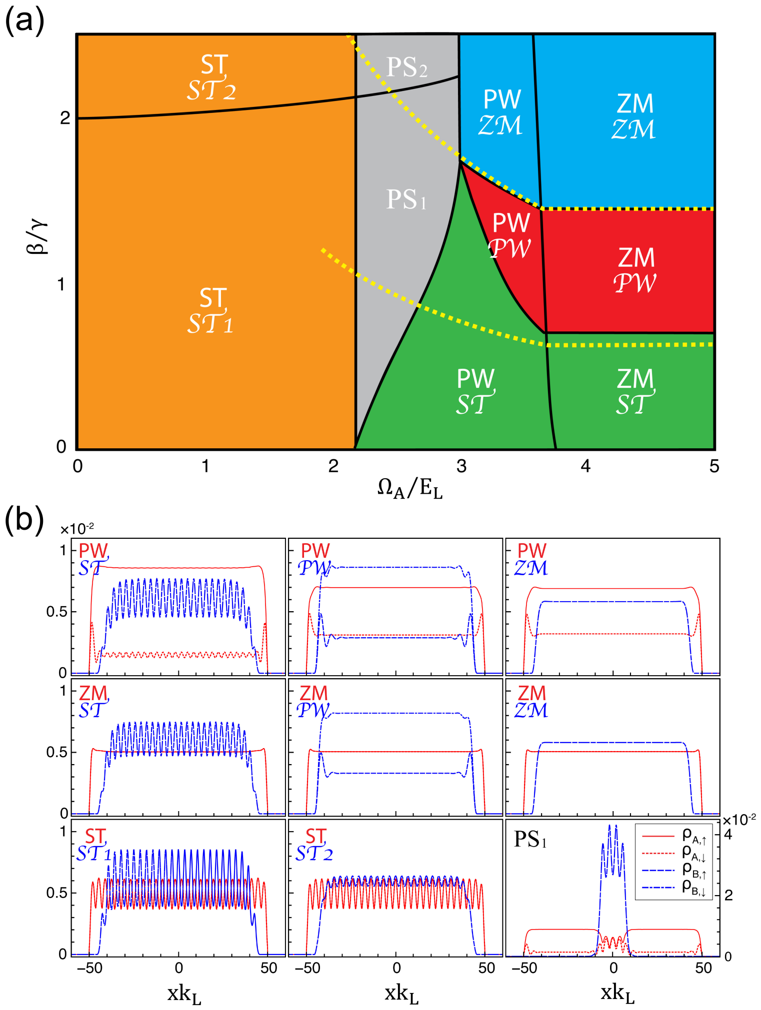

Figure 3.5 : (a) Ground-state phase diagram in the case of $N_A \gg N_B$ where the upper and lower yellow dashed lines indicate the analytical phase boundary predicated by Eq. (3.36) and (3.35), respectively. (b) Typical density profiles of each phases in phase diagram (a), where density of each species has been renormalized to 1, i.e. $\sum_\sigma \int dx \rho_{i,\sigma} = 1$. The the density distribution of PS_1 phase, which is measured by the right ticks, is a phase separation (PS) with PW phase on the box edge and meanwhile ST/$\mathcal{ST}_1$ phase in the middle. Moreover, similar to PS_1, the phase PS_2 (not shown) is also a PS but with ST/$\mathcal{ST}_2$ in the middle. In the calculation, we take $N_A = 2.5 \times 10^4 = 25 N_B$. The unit $E_L = k_L^2/2m_A$ is the recoil energy.

potentials ($L_A = 100k_L^{-1} \approx 27\mu m$ and $L_B = 0.9L_A$ with L_i being the box width), which have been already realized in recent experiment. One can see in Fig. 3.5(b) that the superiority of the boxed potential is to well simulate a homogeneous system in the middle of the box. However, near the edge, the density distributions are severely modulated. Therefore, taking L_B slightly smaller than L_A is mainly to reduce this edge effects from A to B. Moreover, we fix $a_\gamma = a_\alpha = 35a_B$ and $a^i_{\uparrow\downarrow} = 0.8a^i$ where two species are highly miscible, and for either species three quantum phases are predicated to exist. Finally, we modulate the values of Ω_A and β to map out the whole phase diagram.

In the region where A is in PW or ZM phase, the upper and lower yellow dashed line on the phase diagram Fig. 3.5(a) are the phase boundaries Ω_B^{P-Z} and Ω_B^{S-P} given by Eq. (3.36) and (3.35), respectively. Apparently, Ω_B^{P-Z} fits quite well with our numerical result, while Ω_B^{S-P} has a deviation especially near $\Omega_A \to \Omega_A^{S-P}$. The phase boundaries, either Ω_B^{P-Z} or Ω_B^{S-P}, is Ω_A-dependent (-independent) when A is in PW (ZM) phase, which can be understood by the fact that, in Eq. (3.33), the θ_A is Ω_A-dependent when A is in PW phase while θ_A is fixed as $\pi/4$ when A is in ZM phase. Furthermore, the mismatch between numerical and analytical Ω_B^{S-T} is due to the fact that the back influence from B to A can be no longer neglected when Ω_A approaches Ω_A^{S-P} from righthand side. Near Ω_A^{S-P}, species A possesses a large polarization with a small θ_A. In this case, the density of the lower-density component $\rho_{A,\downarrow}$ is strongly perturbed by ρ_B, and as a result possesses a shallow stripe (see $\rho_{A,\downarrow}$ of PW/$\mathcal{ST}$ phase in Fig. 3.5(b)). The striped behavior of species A will finally prompts B to stay in the $\mathcal{ST}$, which explains the enlarged area of phase PW/$\mathcal{ST}$.

Now we turn to discuss the left 4 phases in phase diagram Fig. 3.5(a). When A is in the ST phase, species B has two different stripes $\mathcal{ST}_{1,2}$. The difference between

$\mathcal{ST}_{1,2}$ is that the stripe fringes of species B are out-of-phase or in-phase with that of species A. From the examination of the wave function in momentum space, we find that, the wave function of $\mathcal{ST}_{1,2}$ can be roughly described by

$$\mathbf{\Psi}_B \propto \begin{pmatrix} \cos\theta_B \\ \sin\theta_B \end{pmatrix} e^{i\kappa_B x_B} + \begin{pmatrix} \sin\theta_B \\ \cos\theta_B \end{pmatrix} e^{-i\kappa_B x_B} - \epsilon \begin{pmatrix} e^{3i\kappa_B x_B} \\ e^{-3i\kappa_B x_B} \end{pmatrix}, \tag{3.40}$$

where $\epsilon \ll 1$ is a small quantity. Here, we have neglected a global normalization factor. For a certain value of Ω_A, the ϵ decreases while $\sin\theta_B$ increases as β increases. Particularly at $\beta \approx 2\gamma$, $\epsilon \approx \sin\theta_B$ where the visibility of $\rho_{B,\sigma}$ almost vanishes. This lines the phase boundary between $\mathcal{ST}_{1,2}$, which is in good agreement with our former analytical discussion. Moreover, we also observe two intermediate phases $PS_{1,2}$ located near Ω_A^{S-P}. One can see from the bottom-right subfigure in Fig. 3.5(b) that $PS_{1,2}$ are phase-separation states, i.e. near the box edge, species A is a PW, while in the middle, the mixture has a ST/$\mathcal{ST}_{1,2}$.

3.2.3 Case of $N_A = N_B$

In this case, two species have strong mutual influence. In our numerical simulation of the GP equation, we set $N_A = N_B = 1 \times 10^4$ and $L_A = L_B = 100k_L^{-1} \approx 27\mu m$, and keep all the other parameters used in the former calculation unchanged. Fig. 3.6(a) shows the ground-state phase diagram, and Fig. 3.6(b) shows the typical density profiles of the three new phases: longitudinal polarized stripe (PST)/$\mathcal{ST}$, ST/$\mathcal{ST}_3$, and the third phase separation PS$_3$. One apparent feature in this parametric condition is that all the homogenous phases disappear, which is obviously due to the strong mutual influence between A and B. Particularly, the PST/$\mathcal{ST}$ phase is a generalization of PW/$\mathcal{ST}$ phase of Fig. 3.5(a), where either spin components of species A, $\rho_{A,\uparrow}$ or $\rho_{A,\downarrow}$, is severely affected by species B through the interaction $\mathcal{G}_{AB}$. The ground-state

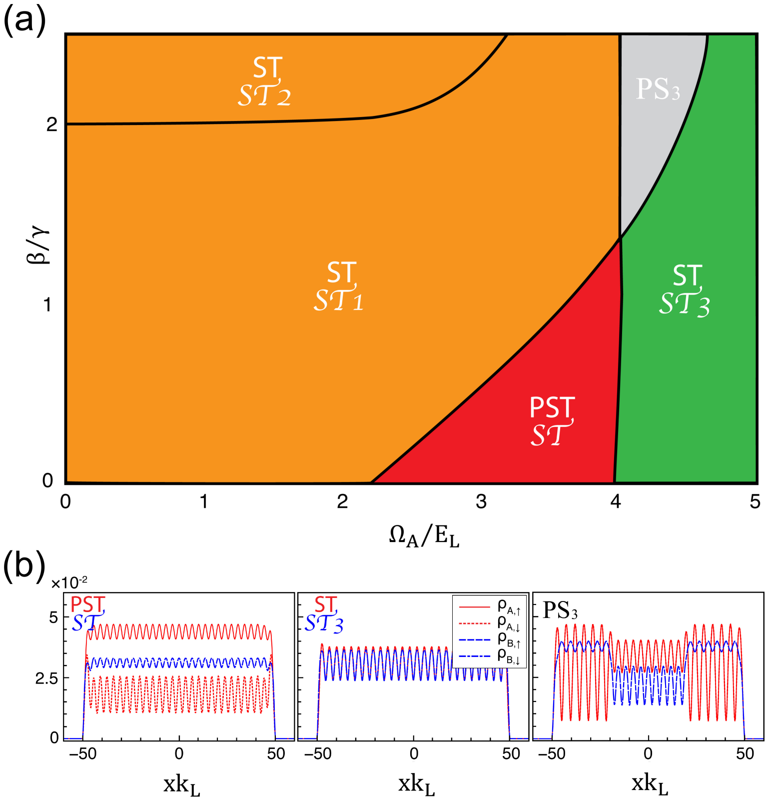

Figure 3.6 : (a) Ground-state phase diagram in the case of $N_A = N_B$. (b) Typical density profiles of the PST/$\mathcal{ST}$, ST/$\mathcal{ST}_3$ and PS$_3$ phases, where the density of each species has been renormalized to 1, i.e. $\sum_\sigma \int dx \rho_{i,\sigma} = 1$. In the calculation, we take $N_A = N_B = 1 \times 10^4$, and $L_A = L_B = 100 k_L^{-1}$ with all the other parameters remain same as the phase diagram Fig. 3.5.

wave function of PST phase can also be approximately discribed by Eq. (3.31) with $C_+ \neq C_-$, and as a result A has a z-axis polarization. One can see that the PST/$\mathcal{ST}$ phase is greatly suppressed by ST/$\mathcal{ST}_1$ as Ω_A increases. This behavior results from a back action from B to A. Specifically, without species B and β, the Raman coupling of species A is only Ω_A and it induces the A's phase transition from ST to PW; with species B and β, the heteronuclear spin-exchange β provides A an effective transverse magnetic field $\beta\left(\psi^*_{B,\downarrow}\psi_{B,\uparrow} + \psi^*_{B,\uparrow}\psi_{B,\downarrow}\right)$, and this term suppresses the effect of Ω_A, and thus the ST to PST transition needs a larger Ω_A. The ST/$\mathcal{ST}_3$ phase is a generalization of ZM/$\mathcal{ST}$ phase of Fig. 3.5(a). Unlike the ST/$\mathcal{ST}_{1,2}$ phase where the species A is a superposition of two spinor states with momenta $k_A = \pm\kappa_A$, the ground-state wave function of species A here is a superposition of the states $k_A = 0$ and $k_A = \pm 2\kappa_A$ in which $k_A = 0$ plays a dominant role, i.e.

$$\mathbf{\Psi}_A \propto \begin{pmatrix} 1 \\ 1 \end{pmatrix} + \epsilon \begin{pmatrix} e^{2i\kappa_A x_A} \\ e^{-2i\kappa_A x_A} \end{pmatrix}. \tag{3.41}$$

Again, a global normalization constant has been neglected. Comparing with the wave function of ZM phase, the additional ϵ term results from the influence from B to A, which finally leads to a striped density distribution. Besides, we find a intermediate phase PS$_3$ located between ST/$\mathcal{ST}_1$ and ST/$\mathcal{ST}_3$, whose density distribution is shown in the third column of Fig. 3.6(b). Near the box edge, we have a ST/$\mathcal{ST}_3$ while in the middle we have a ST/$\mathcal{ST}_1$.

Chapter 4

Cavity-assisted Spin-orbit Coupling in Cold Atoms in an Optical Cavity

The interaction between atomic internal pseudo-spin degrees of freedom (hyperfine states) and quantized photon field supported by an optical cavity has long been a focus of the field of cavity quantum electrodynamics (CQED) [65]. The advent of cold atoms makes the atomic center-of-mass (COM) motion no longer negligible, and hence the coupling between the atomic external COM degrees of freedom and the cavity photon field needs to be considered. The Bose-Einstein condensate in a CQED system has been realized in experiments on various platforms [66, 67]. In this system, the mutual influence between the atomic COM motion and the cavity photon field modifies the collective atomic motion [68, 69], the cavity transmission spectra [70], and can lead to matter wave bistability [71] and multistability behaviors [72], the entanglement generation [73], etc. In the experimental realization of Dicke model in Ref. [74, 75], the two-level atomic system is formed by two motional states of the atom.

The purpose of this Chapter is to understand the mutual influence between three degrees of freedom, including the atomic internal pseudo-spin states, the atomic COM motion, and the cavity photon field. Due to the fact that the photon field influences both the internal and external states of the atom, an effective spin-orbit coupling (SOC) can be realized. In section 4.1, we systematically discuss how the spin-orbit coupling affect the ground-state and dynamic properties of the JC model and the superradiant phase transition in the TC model. In section 4.2, we add dissipations into our model through considering the photon pumping and leakage of the optical cavity, and compare the mean-field results with results obtained from the beyond-mean-field quantum Master equation.

Here, it needs to be explicitly stated that Sec. 4.1 is reprinted from Ref. [20] and Sec. 4.2 is reprinted from Ref. [21], except some minor add-ons, modifications and reorganizations.

4.1 Effects of Spin-Orbit Coupling on Jaynes-Cummings and Tavis-Cummings Models

One of the simplest CQED systems is described by the Jaynes-Cummings (JC) model [76] which concerns the interaction of a single two-level atom and a single-mode cavity field under the rotating wave approximation. Over the past few decades, various techniques have been developed to realize such a system in experiment [77–86], and both the static [80–82] and dynamic [83, 84] properties have been explored. The corresponding model with N two-level atoms coupled identically to the single-mode cavity was considered by Dicke [87] and, later, by Tavis and Cummings [88]. In the literature, the N-atom model with and without the rotating wave approximation are often referred to as the Tavis-Cummings (TC) model and the Dicke model, respectively. It was Dicke who first suggested to treat all atoms as a single quantum system in the study of coherent spontaneous radiation process [87] and proposed what is now called the Dicke states which are a family of correlated N-atom states whose spontaneous emission rate scales as N^2. In the context of CQED, both the TC and the Dicke model predict the superradiant phase transition which describes a sudden emergence of macroscopic cavity photon number when the atom-cavity coupling strength exceeds a critical value. Several recent experiments have explored this phoenomenon [74, 75, 89]. Theoretically, the Dicke superradiant phase transition in both zero [90–93] and finite [94] temperatures has been investigated, and the non-equilibrium physics [95, 96] of the Dicke model has also been considered.

Our purpose in this section is to investigate the effects of the SOC on both the JC and the TC models. In experimental setups for both Bose [3, 97–99] and Fermi [9, 11] gases, the SOC is generated by a pair of counter-propagating coherent laser beams coupling two hyperfine states of the atom via a two-photon Raman process [100]. Many-body [4, 33, 101–103] and few-body [17, 22, 23] theories have been proposed to study the emergence of various quantum phases, and the SOC-induced dynamics [104, 105] has been investigated. In our proposal, we replace one of the Raman laser beams by the cavity field which is *dynamically* coupled to the atoms, in the sense that the atomic dynamics provides a back action to the cavity field. Several previous studies have focused on the properties of quantum gases subjected to such dynamic SOC [21,106–110]. In Ref. [87], Dicke already considered the effect of the atomic COM motion on the superradiant emission, although SOC was not explicitly mentioned.

Our system is schematically shown in Fig. 4.1, where ultracold atoms are inside a ring optical cavity that supports a single plane-wave mode. The cavity field, together with an external coherent laser field, drives a two-photon Raman transition between two internal pseudo-spin states of the atom. This gives rise to an effective coupling between atom's pseudo-spin and external center-of-mass (COM) motion. The motivation of this section is to clarify how the atomic COM motion and the SOC modify the static and dynamic properties of the JC model and the superradiant phase transition in the TC model.

This Section is organized as follows. In Sec. 4.1.1 we analytically present the excitation number and the energy dispersion of a single atom with cavity-assisted SOC in homogeneous space, and compare these results to the JC model and the classical-laser-induced SOC. In Sec. 4.1.2 we show that the combination of SOC and a confining trapping potential not only further modifies the excitation number of the JC model, but also dramatically modifies the spin dynamics. In Sec. 4.1.4 we investigate the Dicke superradiant phase transition of a many-atom system in the thermodynamic limit, and discuss how the cavity-assisted SOC modifies the Dicke phase transition boundary.

4.1.1 Single Atom without Trap

We consider a single atom with two internal pseudo-spin states, denoted as $|\uparrow\rangle$ and $|\downarrow\rangle$, inside a ring cavity, as shown in Fig. 4.1(a). The ring cavity supports a single mode travelling wave with frequency ω_C, and an external light source produces an additional classical laser beam with frequency ω_R. These two counter-propagating light beams induce a two-photon Raman transition between the $|\uparrow\rangle$ and $|\downarrow\rangle$ states, and simultaneously transfer a recoil momentum of $\pm 2q_r$ to the atom along the cavity axis which we denote as the z-axis. In the lab frame, this cavity-assisted SOC model with the rotating wave approximation is governed by the following Hamiltonian,

$$h_{\text{lab}} = \frac{\hat{k}_{\text{lab}}^2}{2m} + \frac{\omega_0}{2}\hat{\sigma}_z + \frac{\Omega e^{2iq_r z}}{2}\hat{\sigma}^+ c + \frac{\Omega e^{-2iq_r z}}{2}\hat{\sigma}^- c^\dagger + \omega_L c^\dagger c, \tag{4.1}$$

where m is the atomic mass, $\hat{k}_{\text{lab}}$ denotes the atomic COM momentum operator along the cavity axis, ω_0 represents the energy difference between $|\uparrow\rangle$ and $|\downarrow\rangle$, c and $c^\dagger$ are the cavity photon annihilation and creation operator, respectively, $\omega_L = \omega_C - \omega_R$ describes the frequency difference between two light beams, and Ω is the single-photon Raman coupling strength. A rotation with frequency ω_R of the coherent laser beam has been considered in obtaining Hamiltonian h_{lab}. We will always assume $\omega_L > 0$ in this work, as, otherwise, Hamiltonian (4.1) supports no ground state. We have set $\hbar$ equal to unity for convenience and will choose ω_0 as the energy unit. Here $\hat{\sigma}_z$, $\hat{\sigma}^+$, and $\hat{\sigma}^-$ are defined as

$$\begin{aligned} \hat{\sigma}_z &= \left|\uparrow\right\rangle \left\langle\uparrow\right| - \left|\downarrow\right\rangle \left\langle\downarrow\right|; \\ \hat{\sigma}^+ &= \left|\uparrow\right\rangle \left\langle\downarrow\right|; \quad \hat{\sigma}^- = \left|\downarrow\right\rangle \left\langle\uparrow\right|. \end{aligned} \tag{4.2}$$

Note that for simplicity, we have ignored the atomic COM motion along the two transverse directions perpendicular to the cavity axis, as they are not coupled to the cavity field. It is often more convenient to work in a quasi-momentum frame where the Hamiltonian reads

$$h = \frac{\hat{k}^2}{2m} + \frac{q_r \hat{k}}{m}\hat{\sigma}_z + \frac{\omega_0}{2}\hat{\sigma}_z + \frac{\Omega}{2}\left(\hat{\sigma}^+ c + \hat{\sigma}^- c^\dagger\right) + \omega_L c^\dagger c. \tag{4.3}$$

Here the quasi-momentum frame and the lab frame are connected by a gauge transformation $h = \mathrm{U} h_{\mathrm{lab}} \mathrm{U}^\dagger$ with

$$\mathrm{U} \equiv \mathrm{e}^{-iq_r z} \left|\uparrow\right\rangle \left\langle\uparrow\right| + \mathrm{e}^{iq_r z} \left|\downarrow\right\rangle \left\langle\downarrow\right|. \tag{4.4}$$

Note that in the quasi-momentum frame, $\hat{k} = -i\partial/\partial z$ represents the COM quasi-momentum operator, which is related to actual atomic momentum $\hat{k}_{\mathrm{lab}}$ as $\hat{k}_{\mathrm{lab}} = \hat{k} + \hat{\sigma}_z q_r$. In the following, our discussion will be in the quasi-momentum frame if not otherwise specified.

In this homogeneous system, both the quasi-momentum $\hat{k}$ and the excitation number

$$\hat{n} = c^+ c + \left|\uparrow\right\rangle \left\langle\uparrow\right|, \tag{4.5}$$

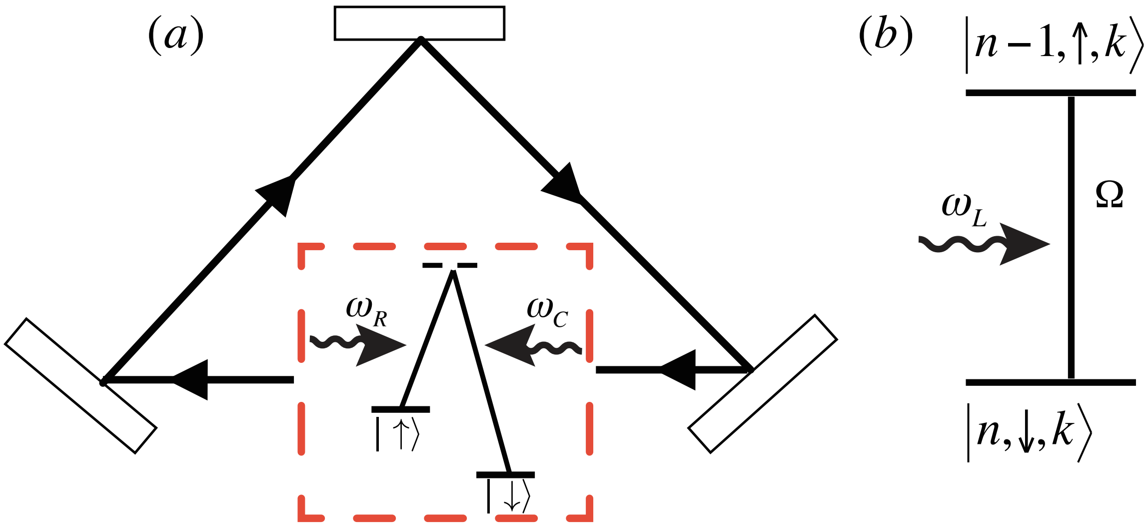

Figure 4.1 : (a) Schematic diagram of the spin-orbit coupled system in a ring cavity. (b) Effective two level model for the scheme in (a), where a photon field with frequency ω_L induces a transition from $|n,\downarrow,k\rangle$ to $|n-1,\uparrow,k\rangle$, during which the actual atomic COM momentum $\hat{k}_{\text{lab}} = \hat{k} + \hat{\sigma}_z q_r$ changes from $k - q_r$ to $k + q_r$.

are conserved. Our model, as described by Hamiltonian (4.3), can also be effectively viewed as a two level atom coupled by a photon field with frequency ω_L as shown in Fig. 4.1(b). A coupling is present between the states $|n,\downarrow,k\rangle$ and $|n-1,\uparrow,k\rangle$, where $|n_p,\sigma,k\rangle$ denotes a state with n_p cavity photons, and the atom in spin-σ with quasi-momentum k. This spin flipping transition conserves k, but the actual atomic COM momentum $\hat{k}_{\text{lab}}$ changes from $k-q_r$ to $k+q_r$ as its spin changes from $|\downarrow\rangle$ to $|\uparrow\rangle$ by absorbing a cavity photon. Note that if the photon recoil momentum vanishes, i.e., $q_r = 0$, (which occurs when the cavity field and the external laser beam are co-propagating), the SOC term (the second term on the r.h.s. of Hamiltonian (4.3)) is absent, thus the atomic COM motion is completely decoupled from the cavity field. Under this situation, our system is reduced to the conventional JC model after the irrelevant kinetic energy term $\hat{k}^2/(2m)$ in Hamiltonian (4.3) is ignored. In this section, we investigate the ground state excitation number, and clarify how the SOC modifies the JC model. We also discuss how the quantization of the cavity photon field modifies the SOC induced by two classical lasers.

We choose $|n_p, \sigma, k\rangle$ as the basis states. As the excitation number n and atomic quasi-momentum k are good quantum numbers, we can consider the two-dimensional subspace characterized by $n \geq 1$ and atomic momentum k which is spanned by two basis states $|n-1, \uparrow, k\rangle$ and $|n, \downarrow, k\rangle$. The Hamiltonian for this subspace is given by (the subspace for $n = 0$ contains only one state $|0, \downarrow, k\rangle$):

$$h_n(k) = \begin{bmatrix} h_n^{\uparrow}(k) & \frac{\sqrt{n}\Omega}{2} \\ \frac{\sqrt{n}\Omega}{2} & h_n^{\downarrow}(k) \end{bmatrix}, \tag{4.6}$$

with

$$\begin{aligned} h_n^{\uparrow}(k) &= \frac{k^2}{2m} + \frac{q_r k}{m} + \frac{\omega_0}{2} + (n-1)\,\omega_L\,; \\ h_n^{\downarrow}(k) &= \frac{k^2}{2m} - \frac{q_r k}{m} - \frac{\omega_0}{2} + n\omega_L\,. \end{aligned} \tag{4.7}$$

Diagonalizing $h_n(k)$, we obtain two energy dispersions in this subspace

$$E_{n\geqslant 1}^{\pm}(k) = \frac{k^2}{2m} \pm \frac{1}{2}\sqrt{\left(\delta_k^{\mathrm{eff}}\right)^2 + n\Omega^2} + \left(n - \frac{1}{2}\right)\omega_L\,, \tag{4.8}$$

where

$$\delta_k^{\mathrm{eff}} = \delta + 2q_r k/m\,, \tag{4.9}$$

with $\delta = \omega_0 - \omega_L$ being the bare two-photon detuning for the Raman transition, and the effect of the SOC can be regarded as producing a momentum-dependent effective two-photon detuning δ_k^{eff}. To complete the spectrum, we should also include the single dispersion curve in the $n = 0$ sector which is given by

$$E_{n=0}^{-}(k) = \frac{k^2}{2m} - \frac{q_r k}{m} - \frac{\omega_0}{2}\,. \tag{4.10}$$

Ground-State Excitation Number

In the following, we will first consider the ground state excitation number in this subsection, and then discuss the energy dispersion curve in the next subsection.

For the case with $\delta = 0$, by taking the derivative of $E_n^-(k)$, we analytically obtain one minimum for $E_0^-(k)$ at $k = q_r$, two minima for $E_{1\leqslant n<n_c}^-(k)$ at $k = \pm q_r\sqrt{1 - n\Omega^2/\left(16E_r^2\right)}$, and one minimum for $E_{n\geqslant n_c}^-(k)$ at $k = 0$, where $n_c = \left(4E_r/\Omega\right)^2$, and $E_r = q_r^2/\left(2m\right)$ is the photon recoil energy which also characterizes the strength of the SOC. Hence, the energy minimum $E\left(n\right)$ in each n subspace can be written into two pieces

$$\begin{aligned} E\left(n\right) \quad &= n\left(\omega_0 - \tfrac{\Omega^2}{16E_r}\right) - \tfrac{\omega_0}{2} - E_r, \quad\ n < n_c \\ E\left(n\right) \quad &= \omega_0\left(\sqrt{n} - \tfrac{\Omega}{4\omega_0}\right)^2 - \tfrac{\Omega^2}{16\omega_0} - \tfrac{\omega_0}{2}, \quad n \geqslant n_c \end{aligned} \tag{4.11}$$

Finally we obtain the ground state energy and the corresponding excitation number by identifying the smallest $E\left(n\right)$ among all n's.

Figure 4.2(a) presents the ground-state excitation number n_{gs} as a function of the Raman coupling strength Ω and the recoil energy or SOC strength E_r. For $E_r = 0$, we recover the result for the JC model, where as Ω increases from zero, n_{gs} starts from 0 and increases with steps of one at succeeding critical values of Ω. This is plotted as the black dashed line in Fig. 4.2(b). The critical values Ω_n at which n_{gs} jumps from n to $n+1$ can be straightforwardly obtained as

$$\begin{aligned} \Omega_{n=0} &\equiv \Omega_c^{\mathrm{JC}} = 2\omega_0\,; \\ \Omega_{n\geqslant 1} &= 2\omega_0\left[\left(2n+1\right) + 2\left(n^2+n\right)^{\frac{1}{2}}\right]^{\frac{1}{2}}\ , \end{aligned} \tag{4.12}$$

where we have denoted the first critical value as Ω_c^{JC}.

In the presence of SOC (i.e., $E_r \neq 0$), n_{gs} still increases in steps at critical values

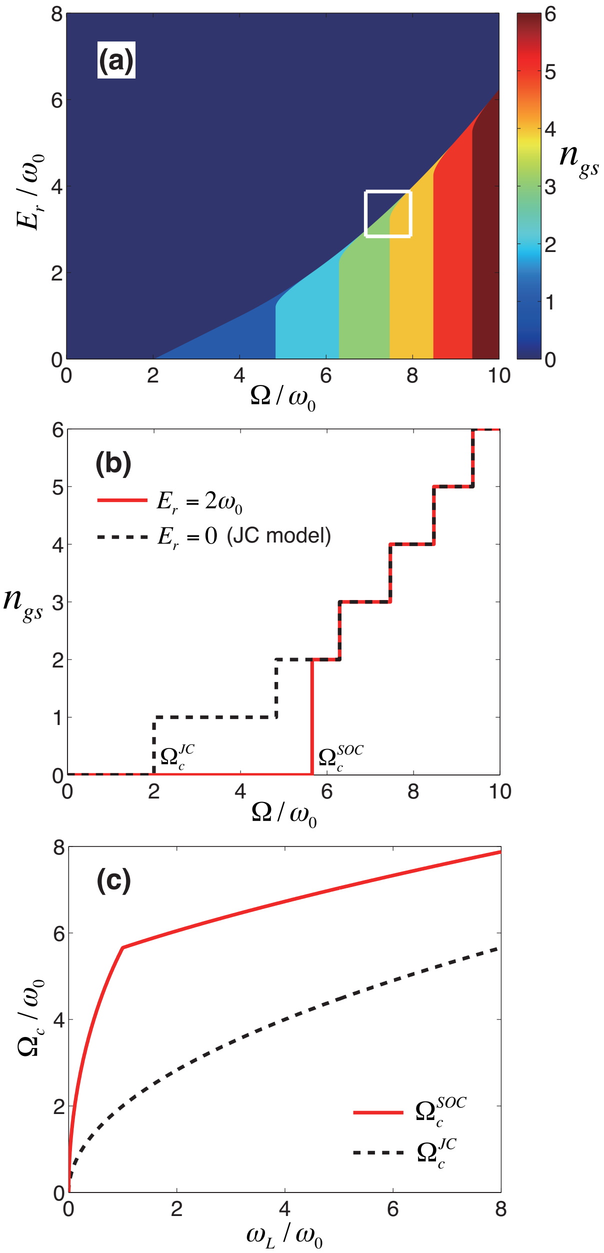

Figure 4.2 : (a) Ground-state excitation number n_{gs} of a single atom in a homogeneous space, as a function of Raman coupling strength Ω and recoil energy E_r, with $\omega_L = \omega_0$. (b) Ground-state excitation numbers for $E_r = 2\omega_0$ and $E_r = 0$ (Jaynes-Cummings model) as step functions of Ω with $\omega_L = \omega_0$. (c) The critical Raman coupling strength at which n_{gs} jumps from 0 to finite value as a function of ω_L/ω_0. The red solid line corresponds to Ω_c^{SOC} with $E_r = 2\omega_0$, and the black dashed line to Ω_c^{JC} obtained at $E_r = 0$.

of Ω. However, in comparison to the JC model, there are some key differences. First the parameter regime for $n_{\text{gs}} = 0$ is enlarged, i.e., the first jump where n_{gs} changes from 0 to finite occurs at a critical Raman coupling strength $\Omega = \Omega_c^{\text{SOC}} > \Omega_c^{\text{JC}}$. This is due to the fact that, as can be seen from Eqs. (4.11) and (4.10), finite E_r (or q_r) reduces the value of $E_{n=0}^{-}$ more than that of $E_{n\geqslant 1}^{-}$, which helps to enlarge the $n = 0$ regime. Here the value of Ω_c^{SOC} can be obtained from Eq. (4.11) as

$$\Omega_c^{\text{SOC}} = \begin{cases} 2\left(\omega_0 + E_r\right)\,, & \text{for } \ E_r \leqslant \omega_0 \\ 4\sqrt{\omega_0 E_r}\,, & \text{for } \ E_r > \omega_0 \end{cases} . \tag{4.13}$$

Second, at $\Omega = \Omega_c^{\text{SOC}}$, n_{gs} jumps from 0 to a finite value that is not necessarily equal to 1. An example is shown in Fig. 4.2(b) as the red solid line. Third, as Ω keeps increasing from Ω_c^{SOC}, n_{gs} will jump with steps of 1 at exactly the same critical values as in the JC model, because for $\Omega > \Omega_c^{\text{SOC}}$, the ground state always occurs at $k = 0$ and $h_n\left(k = 0\right)$ in Eq. (4.11) takes exactly the same form as that in the JC model.

For the case with $\delta \neq 0$, we can proceed in a similar way to obtain results with $\delta \neq 0$. Critical values of Ω at which n_{gs} jumps can still be found analytically, but the results are too cumbersome to write down explicitly. The main features are not qualitatively different from the previous case with $\delta = 0$. In particular, the parameter regime with $n_{\text{gs}} = 0$ is always enlarged in comparison to the JC model. In other words, we always have $\Omega_c^{\text{SOC}} > \Omega_c^{\text{JC}}$ at any value of δ, as can be seen in Fig. 4.2(c).

Energy Dispersion and Degeneracy

We now discuss the energy dispersion curve and ground state degeneracy, which are determined by Eqs. (4.8) and (4.10). For the Raman spin-orbit coupling induced by two classical laser beams whose Hamiltonian is given by

$$h_{\text{cl}} = \frac{\hat{k}^2}{2m} + \frac{q_r\hat{k}}{m}\hat{\sigma}_z + \frac{\delta}{2}\hat{\sigma}_z + \frac{\Omega_{\text{cl}}}{2}\hat{\sigma}^{+} + \frac{\Omega_{\text{cl}}}{2}\hat{\sigma}^{-}\,, \tag{4.14}$$

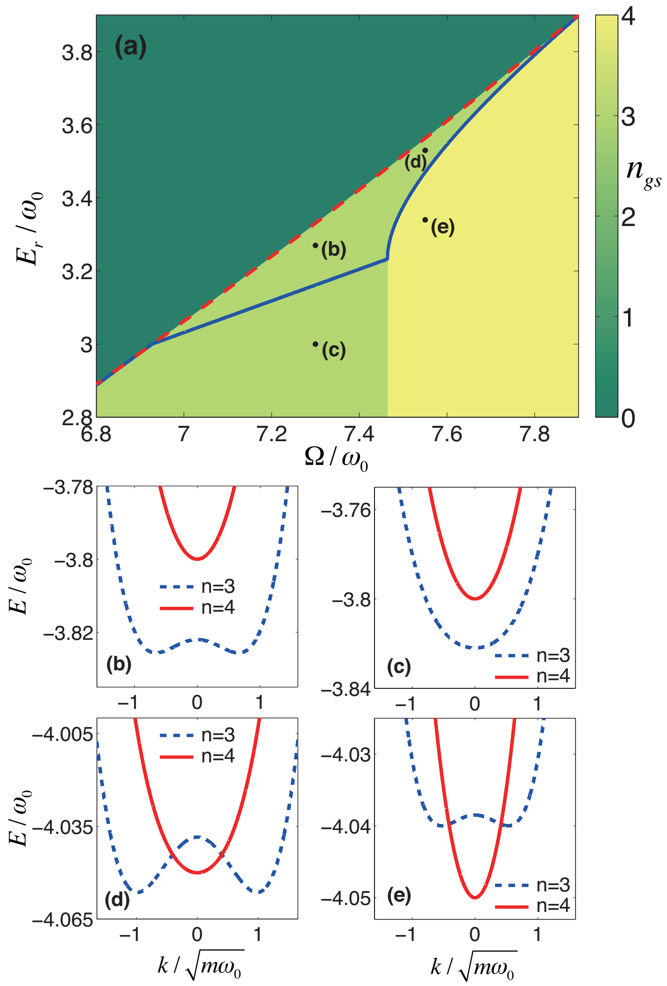

Figure 4.3 : (a) Degenerate-to-nondegenerate transition boundary and ground state excitation number n_{gs} in the parameter space corresponding to the white box in Fig. 4.2(a). The region bounded by the red dash and the blue solid lines features two-fold degenerate ground state. Outside this region, the ground state is non-degenerate. (b)-(e) Energy dispersion relations for excitation number $n = 3, 4$ with $\Omega = 7.3\omega_0$ and $E_r = 3.27\omega_0$ in (b), $\Omega = 7.3\omega_0$ and $E_r = 3\omega_0$ in (c), $\Omega = 7.55\omega_0$ and $E_r = 3.53\omega_0$ in (d), and $\Omega = 7.55\omega_0$ and $E_r = 3.34\omega_0$ in (e). These parameters correspond to points (b)-(e) in (a).

it is well known [13] that, for $\delta = 0$, the energy dispersion exhibits a single minimum when $E_r \leqslant \Omega_{\mathrm{cl}}/4$, and two double minima when $E_r > \Omega_{\mathrm{cl}}/4$.

In our system with quantized light field, things become more complicated. An example is shown in Fig. 4.3. In Fig. 4.3(a), whose parameter space corresponds to that represented by the white box in Fig. 4.2(a), the background color represents the value of ground state excitation number n_{gs}. The region bounded by the red dashed and the blue solid lines has two-fold degenerate ground state, while the other region features nondegenerate ground state. The two lowest dispersion curves of 4 points labelled by (b-e) in Fig. 4.3(a) are plotted in Fig. 4.3(b-e).

As E_r decreases from point (b) to (c), the $n = 3$ dispersion transforms from two double minima to a single minimum, and the ground state changes from degenerate to non-degenerate. This process is similar to what happens in the classical-laser-induced SOC, since the ground state always stays in $n = 3$ dispersion.

As E_r decreases from point (d) to (e), the $n = 3$ dispersion curve always possess two minima, but the ground state changes from degenerate to nondegenerate as the ground state excitation number n_{gs} jumps from 3 to 4. Hence, this process is a unique feature of the cavity-assisted SOC.

4.1.2 Single Atom in Harmonic Trap

In the absence of the trapping potential, the atomic quasi-momentum is conserved. For a fixed quasi-momentum k, Hamiltonian (4.3) is the same as that for the JC model, and the SOC term is to effectively shift the atomic transition frequency ω_0 by a momentum-dependent amount of $2q_r k/m$, or equivalently to give rise to a momentum-dependent detuning δ_k^{eff} defined in Eq. (4.9). When a trapping potential is present, k will no longer be a good quantum number, and different quasi-momentum components will therefore be coupled together. This is the situation we are now going to investigate. Specifically, we will consider the presence of a harmonic trap with trapping frequency ω_t. The total Hamiltonian is now

$$h_t = h + \frac{1}{2} m\omega_t^2 z^2, \tag{4.15}$$

where h is given in Eq. (4.3).

Ground-State Excitation Number

We first consider the ground state excitation number. Note that, even in the presence of the trapping potential, the excitation number n, defined in Eq. (4.5), remains a good quantum number. Note that Hamiltonian (4.15) can be represented by phonon operators a and $a^\dagger$ of the harmonic oscillator as

$$\begin{aligned} h_t =& \omega_t a^\dagger a + i q_r \sqrt{\frac{\omega_t}{2m}} \left(a^\dagger - a\right) \sigma_z \\ &+ \frac{\omega_0}{2} \hat{\sigma}_z + \frac{\Omega}{2} \left(\hat{\sigma}^+ c + \hat{\sigma}^- c^\dagger\right) + \omega_L c^\dagger c, \end{aligned} \tag{4.16}$$

where we have used $\hat{k} = i\sqrt{m\omega_t/2}\left(a^\dagger - a\right)$ and made an energy shift of $\omega_t/2$. We obtain the ground state through the exact diagonalization approach by expanding the Hamiltonian (4.16) onto the basis states $|n_p, \sigma, q\rangle$, where $|n_p\rangle$ is the photon Fock state, $|\sigma\rangle$ is the atomic spin state, and $|q\rangle$ represents the phonon Fock state of the harmonic oscillator defined by $a^\dagger a\,|q\rangle = q\,|q\rangle$. A sufficiently large cutoffs for n_p and q are chosen in the calculation.

Figure 4.4(a1) shows the ground-state excitation number n_{gs} as a function of Raman coupling strength Ω and recoil energy E_r for $\delta = 0$ in the presence of a relatively weak harmonic trap with trap frequency $\omega_t = 3\omega_0$. Compared to the previous result without the trap as shown in Fig. 4.2(a), here the boundaries between different n_{gs} are bent curves instead of straight lines. Figure 4.4(a2) shows n_{gs} as a

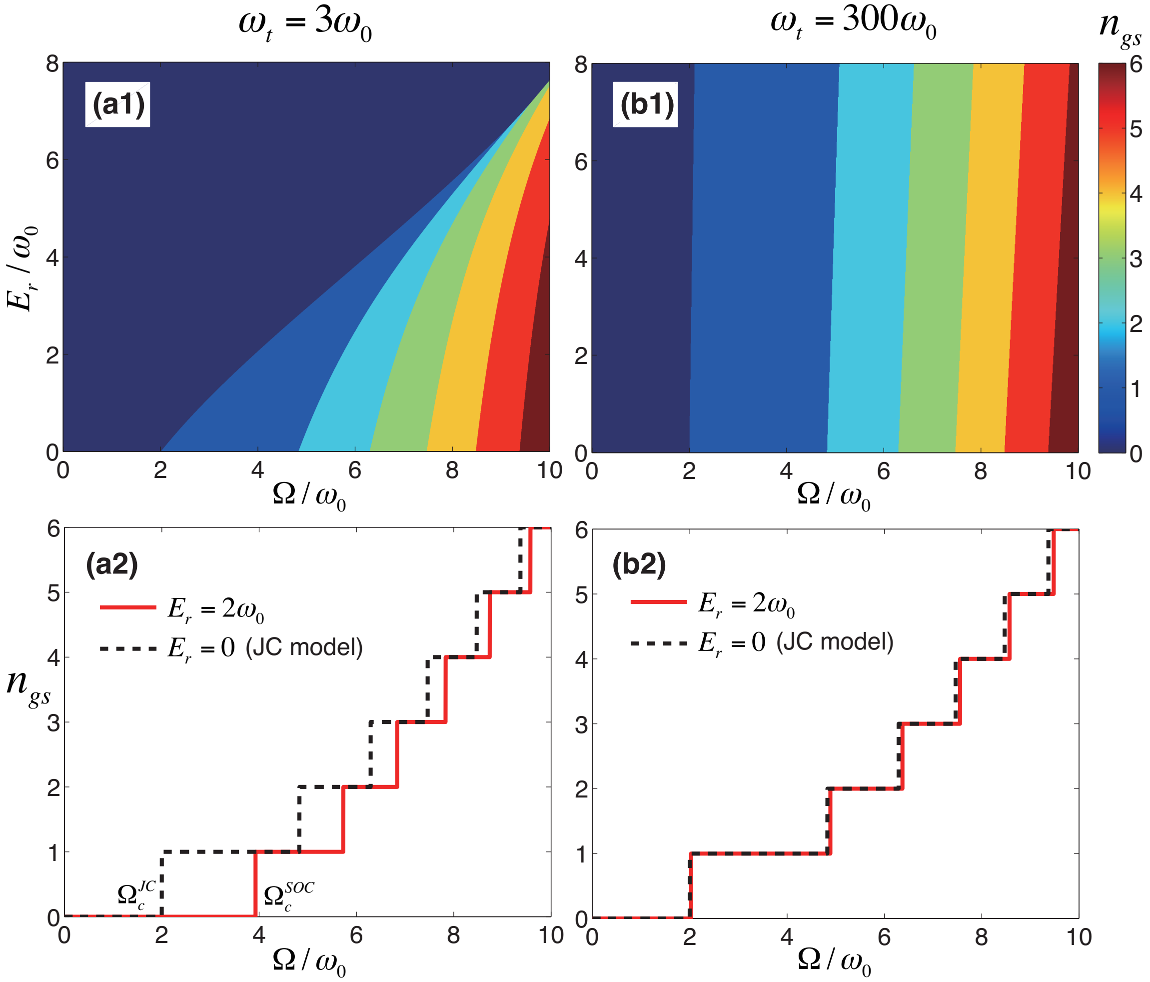

Figure 4.4 : (a1)(b1) Ground-state excitation number n_{gs} of a single atom in harmonic trap with trap frequency $\omega_t = 3\omega_0, 300\omega_0$, as a function of Raman coupling strength Ω and recoil energy E_r. (a2)(b2) The n_{gs} for $E_r = 2\omega_0$ and $E_r = 0$ (Jaynes-Cummings model) as step functions of Ω with $\omega_t = 3\omega_0, 300\omega_0$. Here we consider $\omega_L = \omega_0$.

function of Ω for two values of E_r. The case with $E_r = 0$ corresponds to the absence of SOC and our model is reduced to the JC model. At finite E_r, the SOC term shifts the values of the critical Raman coupling strength at which n_{gs} jumps. In addition, $\Omega_c^{\mathrm{SOC}} > \Omega_c^{\mathrm{JC}}$ is still satisfied for any $\omega_L \geqslant 0$ as in the previous case of homogeneous space.

In Fig. 4.4(b1) and (b2), we plot the n_{gs} for a relatively strong harmonic trap with $\omega_t = 300\omega_0$. In this case, we find that the results for finite E_r are not very different from the JC model results as long as $E_r \ll \omega_t$. This can be intuitively understood as follows. In the presence of a very strong trapping potential, the effect of photon recoil, and hence that of the SOC, becomes less important. This is analogous to the Lamb-Dicke limit in the context of ion trapping, in which the coupling between the ion's internal dynamics and its motional dynamics induced by an external light field is suppressed by a strong confining potential.

Spin Dynamics

In the JC model, when a cavity field with definite photon number (i.e., a cavity Fock state) is coupled to the two-level atom, the ensuing spin dynamics is described by the well-known Rabi oscillation, where the oscillation frequency is determined by the coupling strength Ω and the detuning δ. In our model, the trapping term couples different quasi-momentum states, and each quasi-momentum state experiences a momentum-dependent effective Raman detuning δ_k^{eff}. The resulting spin dynamics becomes much more complicated.

To investigate the spin dynamics in our model, we consider a specific initial state $|\psi(0)\rangle = |n_p, \downarrow, q = 0\rangle$ in the lab frame, where the atom is prepared in the $|\downarrow\rangle$ state and the ground state of the harmonic trap, and the cavity field is in a Fock state with

n_p photons. This confines the system dynamics within the subspace characterized by excitation number $n = n_p$. Within this subspace, the Hamiltonian in Eq. (4.15) takes the form as (after neglecting a dynamically irrelevant constant term)

$$h_t\left(n_p\right) = \frac{\hat{k}^2}{2m} + \frac{q_r\hat{k}}{m}\hat{\sigma}_z + \frac{\delta}{2}\hat{\sigma}_z + \frac{\Omega_{\mathrm{cl}}}{2}\hat{\sigma}^+ + \frac{\Omega_{\mathrm{cl}}}{2}\hat{\sigma}^- + \frac{1}{2}m\omega_t^2 z^2\,, \tag{4.17}$$

where $\Omega_{\mathrm{cl}} \equiv \Omega\sqrt{n_p}$, and $\hat{\sigma}_z$, $\hat{\sigma}^+$, and $\hat{\sigma}^-$ are re-defined as

$$\hat{\sigma}_z = \left|n_p - 1, \uparrow\right\rangle \left\langle n_p - 1, \uparrow\right| - \left|n_p, \downarrow\right\rangle \left\langle n_p, \downarrow\right|\,; \tag{4.18}$$

$$\hat{\sigma}^+ = \left|n_p - 1, \uparrow\right\rangle \left\langle n_p, \downarrow\right|\,; \quad \hat{\sigma}^- = \left|n_p, \downarrow\right\rangle \left\langle n_p - 1, \uparrow\right|\,.$$

Note that this Hamiltonian is mathematically equivalent to the Hamiltonian describing a spin-orbit coupled atom where the SOC is generated by two classical Raman laser beams (see Eq. (4.14)) [3, 13, 97, 98]. As a consequence, the result presented below is also valid in that context. In the classical laser context, the corresponding spin dynamics has been studied in [105], whereas we focus on the effects of the photon recoil on the Rabi oscillation in cases of different trapping strengths.

We solve the time-dependent Schrödinger equation numerically to find the state vector $|\psi(t)\rangle$ starting from the initial state $|\psi(0)\rangle$, we then calculate the probability of finding the atom in $|\uparrow\rangle$:

$$P_{\uparrow}\left(t\right) \equiv \sum_{q=0}^{\infty} \left|\left\langle n_p - 1, \uparrow, q\right| \psi\left(t\right)\rangle\right|^2\,. \tag{4.19}$$

Examples of spin dynamics are plotted in Fig. 4.5(a-c), which represent the $\delta = 0$ cases for a strong, an intermediate, and a weak trap, respectively, where the trap strength is measured against E_r.

Strong Trap — As we discussed in the previous subsection, in the presence of a strong trap with $\omega_t \gg E_r$, the system is in the Lamb-Dicke regime where the effect

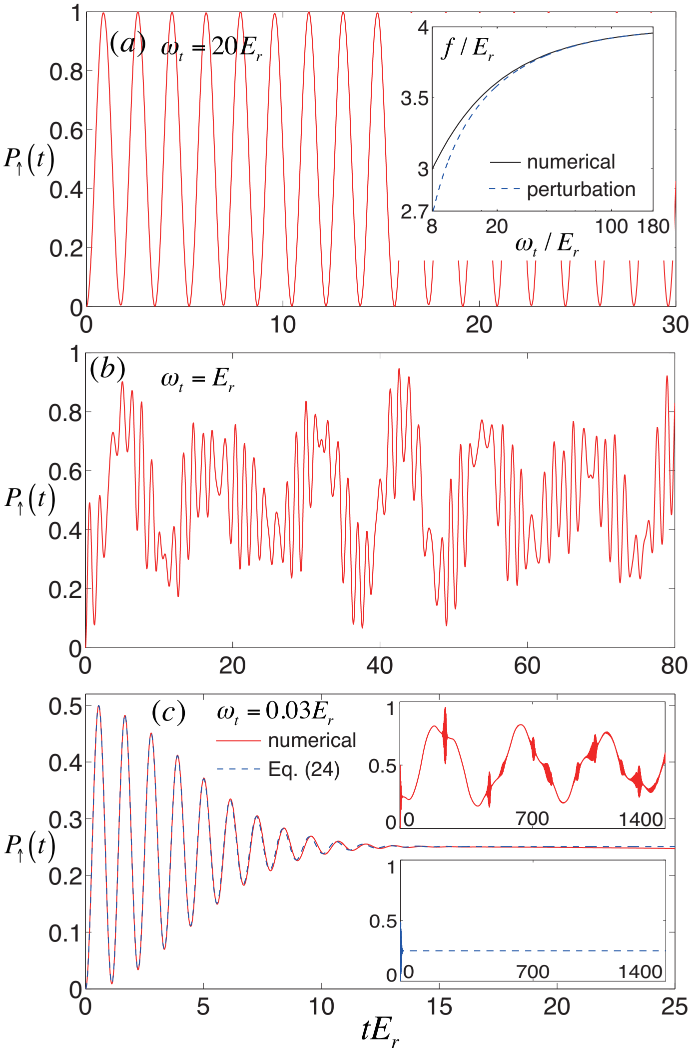

Figure 4.5 : (a)-(c) Time evolution of the spin-up probability $P_\uparrow(t)$ of a single atom in a harmonic trap with $\omega_t = 20E_r$, E_r, and $0.03E_r$. The system is initially prepared in the harmonic oscillator ground state with spin down. The inset of (a) plots $f(\omega_t)$, the oscillation frequency of $P_\uparrow(t)$, as a function of ω_t in the strong trap regime, where the black solid line depicts the numerical result obtained by Fourier analysis and the blue dashed line depicts the analytical result from the perturbation theory [Eq. (4.21)], and a logarithmic scale is used for the horizontal axis. In (c) for the weak trap regime, the red solid line shows the numerical result, and the blue dashed line shows the analytic result in Eq. (4.24) where the coupling between different momentum spaces is neglected. The corresponding long time evolutions of $P_\uparrow(t)$ are shown in the inset of (c). Other parameters: $\Omega_{\mathrm{cl}} = 4E_r$, $\delta = 0$.

of SOC may be regarded as a small perturbation. The corresponding spin dynamics shown in Fig. 4.5(a) is accurately described by a sinusoidal oscillation as

$$P_{\uparrow}(t) = \sin^2\left[\frac{f(\omega_t)}{2}t\right], \tag{4.20}$$

where $f(\omega_t)$ denotes the oscillation frequency depending on ω_t. In the limit of $\omega_t \to \infty$, the JC model result is recovered as the oscillation frequency $f(\omega_t \to \infty) = \Omega_{\text{cl}}$, with the Rabi frequency $\Omega_{\text{cl}} = 4E_r$ in this example. For large but finite ω_t, the oscillation frequency $f(\omega_t)$ deviates away from this value. By treating the SOC term as a small perturbation, we can analytically obtain the oscillation frequency as

$$f(\omega_t) = \Omega_{\text{cl}} - \frac{2E_r\Omega_{\text{cl}}}{\omega_t} - \frac{2E_r\Omega_{\text{cl}}^3}{\omega_t\left(\omega_t^2 - \Omega_{\text{cl}}^2\right)}. \tag{4.21}$$

Details of this derivation can be found in Sec. 4.1.3. In the inset of Fig. 4.5(a), we compare the spin oscillation frequency obtained from the numerical calculation (black solid line) and the analytic result of Eq. (4.21) (blue dashed line), and find excellent agreement for large ω_t.

Weak Trap — An example of weak trap with $\omega_t \ll E_r$ is presented in Fig. 4.5(c), where the short- and long-time behaviours are plotted in the main figure and the insets, respectively. For short-time scale, the system exhibits a damped oscillation. This damped oscillation can be intuitively understood as follows. The initial COM wave function of the atom is a Gaussian (the ground state of the harmonic oscillator), which in the (quasi-)momentum space can be written as

$$\phi_0(k) = (\pi m\omega_t)^{-\frac{1}{4}} e^{-\frac{(k-q_r)^2}{2m\omega_t}}. \tag{4.22}$$

For such a weak trap, and for short time scale, we can neglect the trap-induced coupling between different momentum components. Then each momentum component exhibits Rabi oscillation, such that for a given quasi-momentum k we have

$$p_\uparrow(t,k) = \frac{\Omega_{\mathrm{cl}}^2}{\Omega_{\mathrm{cl}}^2 + \left(\delta_k^{\mathrm{eff}}\right)^2} \sin^2\left(\frac{1}{2}\sqrt{\Omega_{\mathrm{cl}}^2 + \left(\delta_k^{\mathrm{eff}}\right)^2}t\right) , \tag{4.23}$$

where $\delta_k^{\mathrm{eff}} = 2q_r k/m$ is the effective two-photon detuning for the given momentum component k. Integrating over all the momentum components, we have

$$P_\uparrow(t) = \int dk\, |\phi_0(k)|^2 p_\uparrow(t,k)\,. \tag{4.24}$$

In the main figure of Fig. 4.5(c), the red solid line represents the result obtained from the numerical calculation and the blue dashed line the result based on Eq. (4.24). Both results agree with each other very well. The damping of the oscillation arises from the dephasing effect, as different momentum components oscillate at different frequencies due to the momentum-dependent effective detuning δ_k^{eff}.

For time scales on the order of or longer than $1/\omega_t$, the assumption underlying Eq. (4.24) that different momentum components behave independently is no longer valid. The numerically obtained long-time result and the one based on Eq. (4.24) are plotted in the insets of Fig. 4.5(c). Significant discrepancies can be seen. In particular, Eq. (4.24) predicts a featureless flat line: once the dephasing occurs, $P_\uparrow$ no longer oscillates and stays constant. But the full numerical result shows that, due to the momentum components coupling induced by the trapping potential, the long-time behaviour of the system can be quite rich.

4.1.3 Perturbation Theory for Modified Rabi Oscillation

In this subsection, we provide a detailed derivation of Eq. (4.21) using a perturbation calculation. It is more convenient to carry out the calculation in the lab frame, in which the Hamiltonian reads

$$h_t^{\mathrm{lab}} = \frac{\hat{k}^2}{2m} + \frac{1}{2}m\omega_t^2 x^2 + \frac{\delta}{2}\hat{\sigma}_z + \frac{\Omega_{\mathrm{cl}} e^{2iq_r x}}{2}\hat{\sigma}^+ + \frac{\Omega_{\mathrm{cl}} e^{-2iq_r x}}{2}\hat{\sigma}^- , \tag{4.25}$$

which is the counterpart of Hamiltonian (4.17).

In the limit of large trapping frequency $\omega_t \gg E_r$, the atoms are tightly confined within a spatial region much smaller than $1/q_r$. Hence we may Taylor expand the two exponentials in Hamiltonian (4.25) to second order in q_r, and write

$$h_t^{\mathrm{lab}} = h_0 + V, \tag{4.26}$$

where

$$h_0 = \frac{k^2}{2m} + \frac{1}{2} m\omega_t^2 x^2 + \frac{\delta}{2}\hat{\sigma}_z + \frac{\Omega_{\mathrm{cl}}}{2}\hat{\sigma}^+ + \frac{\Omega_{\mathrm{cl}}}{2}\hat{\sigma}^-; \tag{4.27}$$

$$V = \left(iq_r x - q_r^2 x^2\right)\Omega_{\mathrm{cl}}\hat{\sigma}^+ - \left(iq_r x + q_r^2 x^2\right)\Omega_{\mathrm{cl}}\hat{\sigma}^-. \tag{4.28}$$

We shall treat V as a perturbation to h_0, and focus on the case with $\delta = 0$.

The eigenenergies and eigenstates of the unperturbed Hamiltonian h_0 are given by

$$E_{q\pm}^{(0)} = \left(\frac{1}{2} + q\right)\omega_t \pm \frac{\Omega_{\mathrm{cl}}}{2}; \tag{4.29}$$

$$|q\pm\rangle = \frac{1}{\sqrt{2}}\left(|\uparrow\rangle \pm |\downarrow\rangle\right)|q\rangle, \tag{4.30}$$

where q is the harmonic oscillator quantum number. Our initial state has the atom in $|\downarrow\rangle$ and harmonic oscillator ground state $|q = 0\rangle$, which can be written as

$$|\psi(0)\rangle = \frac{1}{\sqrt{2}}\left(|0+\rangle - |0-\rangle\right). \tag{4.31}$$

Neglecting V, the ensuing dynamics will lead to Rabi oscillation with frequency Ω_{cl}, i.e., the energy difference between the two eigenstates $|0\pm\rangle$. This is the result for the JC model.

To find the oscillation frequency when V is included, we shall calculate the energy shift to the states $|0\pm\rangle$ to second order in q_r. The corresponding oscillation frequency will then be

$$f = \left(E_{0+}^{(0)} + E_{0+}^{(1)} + E_{0+}^{(2)}\right) - \left(E_{0-}^{(0)} + E_{0-}^{(1)} + E_{0-}^{(2)}\right) \tag{4.32}$$

with $E_{0\pm}^{(1)}$ and $E_{0\pm}^{(2)}$ being the $1st$ and $2nd$ order energy shift due to the perturbation V, respectively. Through the standard time independent perturbation theory, we obtain

$$E_{0\pm}^{(1)} = \langle 0\pm| V |0\pm\rangle = \mp\frac{E_r\Omega_{\mathrm{cl}}}{\omega_t}; \tag{4.33}$$

and

$$\begin{aligned} E_{0\pm}^{(2)} &= \frac{\left|\langle 1\mp| V |0\pm\rangle\right|^2}{E_{0-}^{(0)} - E_{1\mp}^{(0)}} + \frac{\left|\langle 2\pm| V |0\pm\rangle\right|^2}{E_{0-}^{(0)} - E_{2\pm}^{(0)}} \\ &= -\frac{E_r\Omega_{\mathrm{cl}}^2}{\omega_t\left(\omega_t \mp \Omega_{\mathrm{cl}}\right)} - \left(\frac{E_r\Omega_{\mathrm{cl}}}{\omega_t}\right)^2 \frac{1}{\omega_t}. \end{aligned} \tag{4.34}$$

Substituting Eqs. (4.29)(4.33)(4.34) into Eq. (4.32), we obtain the oscillation frequency of $P_{\uparrow}(t)$

$$f\left(\omega_t\right) = \Omega_{\mathrm{cl}} - \frac{2E_r\Omega_{\mathrm{cl}}}{\omega_t} - \frac{2E_r\Omega_{\mathrm{cl}}^3}{\omega_t\left(\omega_t^2 - \Omega_{\mathrm{cl}}^2\right)}, \tag{4.35}$$

as given in Eq. (4.21) in sec. 4.1.2.

4.1.4 Many-atom Superradiance in Thermodynamic Limit

So far, we have been focusing on the properties of a single atom. In this section, we consider a system where the single mode cavity photon field is coupled to many atoms in thermodynamic limit. We neglect the bare interactions between atoms. However, as each atom influences the whole photon field which back acts on the other atoms, the photon field induces an effective coupling between atoms. When the atomic COM motion is neglected, our model reduces to the TC model. One of the most well-known many-body effects in this model is the Dicke superradiant phase transition [90–94]. Here we investigate how the COM degree of freedom and the SOC affect the Dicke phase transition.

We consider a canonical ensemble where N atoms inside the cavity are confined within a box with volume V. In the thermodynamic limit, both N and V are taken to be infinity but the number density $\rho = N/V$ is finite. The Hamiltonian of this system is given by

$$H = \omega_L c^\dagger c + \sum_{j=1}^{N} \hat{h}_j \,, \tag{4.36}$$

with the Hamiltonian for the jth atom

$$\hat{h}_j = \frac{\hat{\mathbf{k}}_j^2}{2m} + \frac{q_r \hat{k}_{zj}}{m}\sigma_z^j + \frac{\omega_0}{2}\sigma_z^j + \frac{\tilde{\Omega}}{2\sqrt{N}}\left(\sigma_j^+ c + \sigma_j^- c^\dagger\right) \,, \tag{4.37}$$

where $\tilde{\Omega} = \sqrt{N}\Omega$ is the rescaled Raman coupling strength, and $\hat{\mathbf{k}}_j$ is the three dimensional quasi-momentum operator for the jth atom.

To investigate the thermodynamic phase transition at temperature T, we take a similar approach as in Ref. [94] in which the Dicke phase transition in the TC model is investigated. The canonical partition function $Z = \mathrm{Tr}\left(e^{-\beta H}\right)$ with $\beta = 1/\left(k_B T\right)$ can be calculated as

$$Z = \frac{V^N}{(2\pi)^{3N}} \int \frac{d^2\alpha}{\pi} \prod_{j=1}^{N} \left(\int d\mathbf{k}_j \sum_{\sigma_j=\uparrow,\downarrow} \right) \langle\Psi| e^{-\beta H} |\Psi\rangle \,, \tag{4.38}$$

where we have chosen the states

$$|\Psi\rangle = |\alpha\rangle \prod_{j=1}^{N} |\mathbf{k}_j\rangle |\sigma_j\rangle \tag{4.39}$$

as our basis states to evaluate the trace. Here $|\alpha\rangle$ is the photon coherent state, i.e., the eigenstate of photon annihilation operator such that $c|\alpha\rangle = \alpha|\alpha\rangle$, $|\mathbf{k}_j\rangle$ is the quasi-momentum eigenstate for the jth atom, and $|\sigma_j\rangle$ ($\sigma_j = \uparrow, \downarrow$) is the eigenstate of σ_z^j for the jth atom. By using the condition $N \to \infty$, we obtain

$$\langle\alpha| e^{-\beta H} |\alpha\rangle = \exp\left[-\beta\left(\omega_L |\alpha|^2 + \sum_{j=1}^{N} \hat{h}_j^\alpha\right)\right] \,, \tag{4.40}$$

where

$$\hat{h}_j^\alpha = \frac{\hat{\mathbf{k}}_j^2}{2m} + \frac{q_r \hat{k}_{zj}}{m}\sigma_z^j + \frac{\omega_0}{2}\sigma_z^j + \frac{\tilde{\Omega}}{2\sqrt{N}}\left(\sigma_j^+ \alpha + \sigma_j^- \alpha^*\right) . \tag{4.41}$$

As the summation over spin and integral over momentum in Eq. (4.38) are independent for different atoms, the partition function can be simplified as

$$Z = \int \frac{d^2\alpha}{\pi} e^{-\beta\omega_L |\alpha|^2} \left[\frac{V}{(2\pi)^3} \int d\mathbf{k} \left(e^{-\beta\epsilon^+} + e^{-\beta\epsilon^-}\right)\right]^N , \tag{4.42}$$

where

$$\epsilon^\pm = \frac{\mathbf{k}^2}{2m} \pm \sqrt{\left(\frac{q_r k_z}{m} + \frac{\omega_0}{2}\right)^2 + \left(\frac{\tilde{\Omega}}{2}\right)^2 \frac{|\alpha|^2}{N}} \tag{4.43}$$

are the eigenvalues of $\hat{h}_j^\alpha$ in Eq. (4.41). Integrating over the complex angle of α and x, y components of $\mathbf{k}$ in (4.42), and letting $u = \frac{|\alpha|^2}{N}$, we can rewrite the partition function as

$$Z = C_1 \int_0^\infty du \exp\left\{N\left[F(u)\right]\right\} , \tag{4.44}$$

with constant $C_1 = N\left(\frac{mV}{4\pi^2\beta}\right)^N$ and

$$F(u) = -\beta\omega_L u + \log S\left(u\right) , \tag{4.45}$$

$$S\left(u\right) = 2\int dk_z \exp\left(-\frac{\beta k_z^2}{2m}\right) \cosh\xi\left(k_z, u\right) , \tag{4.46}$$

$$\xi\left(k_z, u\right) = \beta\sqrt{\left(\frac{q_r k_z}{m} + \frac{\omega_0}{2}\right)^2 + \left(\frac{\tilde{\Omega}}{2}\right)^2 u} \, . \tag{4.47}$$

The Laplace's method [94] is used to deal with the integral over u in Eq. (4.44). For $N \to \infty$, this yields

$$Z = C_2 \max_{u\in[0,\infty)} \exp\left\{N\left[F(u)\right]\right\} , \tag{4.48}$$

where C_2 is a constant and we denote that the maximum of $F(u)$ is reached at $u = u_0$. We numerically obtain a $u_0 \geqslant 0$ by taking the first and second order derivatives of

$F(u)$, and it is straightforward to show that u_0 is actually the normalized photon number

$$u_0 = \frac{\left\langle c^\dagger c \right\rangle}{N} \,, \tag{4.49}$$

where $\left\langle c^\dagger c \right\rangle /N > 0$ corresponds to the superradiant phase with a macroscopic photon excitation appearing in the thermodynamic limit; and $\left\langle c^\dagger c \right\rangle /N = 0$ corresponds to the normal phase.

Figure 4.6(a) shows $\left\langle c^\dagger c \right\rangle /N$ as a function of the temperature T and the rescaled Raman coupling strength $\tilde{\Omega}$ with the SOC strength $E_r = 0.5\omega_0$. The red solid line in the figure represents the critical coupling strength $\tilde{\Omega}_c$ (i.e., the phase boundary): Above this line, we have $\left\langle c^\dagger c \right\rangle /N > 0$ and the system is in the superradiant phase; and below this line, $\left\langle c^\dagger c \right\rangle /N = 0$ which corresponds to the normal phase. In Fig. 4.6(b), we plot $\tilde{\Omega}_c$ as a function of T for several different values of E_r. As in the previous single-atom case, we recover the usual TC model when $E_r = 0$ (bottom curve in Fig. 4.6(b)). For the TC model, $\tilde{\Omega}_c$ is a monotonically increasing function of T, and $\tilde{\Omega}_c = 2\sqrt{\omega_0\omega_L}$ at $T = 0$. For finite E_r, $\tilde{\Omega}_c$ is larger than the corresponding value in the TC model. In other words, in the presence of the SOC, the regime of normal phase is enlarged, which is consistent with the single-atom property that the SOC enlarges the $n = 0$ regime with no photons, as shown in Eqs. (4.12) and (4.13), and Fig. 4.2. The upward shift of $\tilde{\Omega}_c$ at finite E_r is more pronounced at lower temperature. This may not be surprising as, at lower temperature, the average atomic COM kinetic energy is lower and hence the photon recoil plays a more significant role. This temperature dependent shift leads to another important feature brought by the SOC: $\tilde{\Omega}_c$ is no longer a monotonic function of T, as can be easily seen in Fig. 4.6(b), and reaches the minimum value at a finite temperature.

A consequence of the nonmonotonic behaviour of $\tilde{\Omega}_c$ is that the normal phase

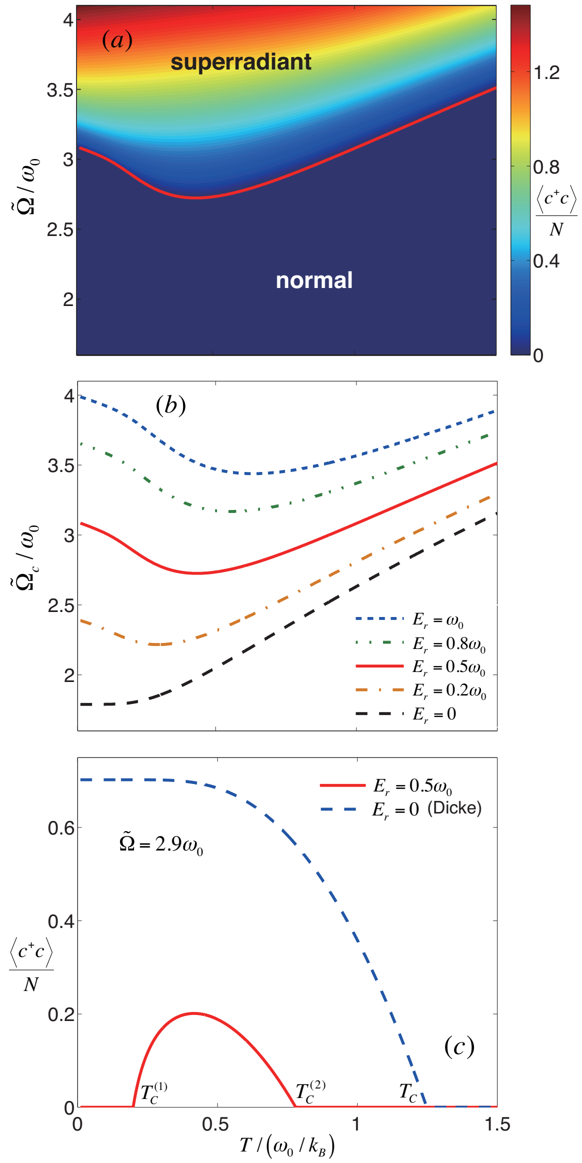

Figure 4.6 : (a) Normalized photon number $\langle c^\dagger c\rangle/N$ as a function of temperature T and effective Raman coupling strength $\widetilde{\Omega}$ with $E_r=0.5\omega_0$, where $\langle c^\dagger c\rangle$ is the average photon number and N is the atom number. Here $\langle c^\dagger c\rangle/N>0$ corresponds to the superradiant phase and $\langle c^\dagger c\rangle/N=0$ corresponds to the normal phase. (b) Normal-Superradiant Phase boundary in $T-\widetilde{\Omega}$ plane for $E_r/\omega_0=0,0.2,0.5,0.8,1$. (c) $\langle c^\dagger c\rangle/N$ as a function of T for $\widetilde{\Omega}=2.9\omega_0$ with $E_r/\omega_0=0,0.5$. We take $\omega_L=0.8\omega_0$ in these figures.

may become reentrant as the temperature varies. This is depicted in Fig. 4.6(c), where we plot $\left\langle c^\dagger c \right\rangle /N$ as a function of T with $\tilde{\Omega} = 2.9\omega_0$ for $E_r = 0.5\omega_0$ (red solid line) and $E_r = 0$ (blue dashed line). For the TC model ($E_r = 0$), the system is in the superradiant phase at sufficiently low temperature when $\tilde{\Omega} > 2\sqrt{\omega_0\omega_L}$ (as is the case shown in Fig. 4.6(c)) with finite $\left\langle c^\dagger c \right\rangle /N$. As temperature increases, $\left\langle c^\dagger c \right\rangle /N$ decreases monotonically until it reaches 0 at the critical temperature T_c which is given by

$$\frac{4\omega_0\omega_L}{\tilde{\Omega}^2} = \tanh\left(\frac{\omega_0}{2\omega_L k_B T_c}\right) . \tag{4.50}$$

For the example shown in Fig. 4.6(c) with finite E_r, the system is in the normal phase with $\left\langle c^\dagger c \right\rangle /N = 0$ at both the low and the high temperature ends, and is in the superradiant phase in an intermediate temperature window between $T_c^{(1)}$ and $T_c^{(2)}$.

A remark is in order. In our derivation of the partition function Z in Eq. (4.38), we have treated the N atoms as distinguishable particles which obey the Boltzmann distribution. In other words, we have ignored the quantum statistics of atoms. This should be a good assumption at high temperature. We may estimate the temperature regime in which this assumption is valid as follows. Let us assume that the atoms are ideal bosons. The critical temperature for the bosons to form Bose-Einstein condensate is given by

$$T_{\text{BEC}} = 3.31\frac{\hbar^2\rho^{\frac{2}{3}}}{mk_B} \approx 3\times 10^{-4}\left(\frac{\hbar\omega_0}{k_B}\right), \tag{4.51}$$

where we have taken typical values such that the atomic number density $\rho = 10^{13}\text{cm}^{-3}$, m the mass of ^{87}Rb atom, and energy splitting between two ground state hyperfine states $\omega_0 = 2\pi \times 4.81\text{MHz}$. When $T \gg T_{\text{BEC}}$, quantum statistics is not important, and the bosons can in practice be treated as distinguishable particles. As T_{BEC} is very small in our unit system, our results as presented in Fig. 4.6 should largely remain valid for typical experimental situations. Note that as T_{BEC} is roughly the same as Fermi degenerate temperature, this estimate is also valid for a system of Fermi gas. How to properly incorporate quantum statistics of atoms in the calculation for temperatures within the quantum degenerate regime remains a challenge and will be investigated in the future.

4.2 Spin-orbit Coupled Atoms inside a Dissipative Optical Cavity

In this Section, we extend our previous system to a dissipative system with photon pumping into the cavity and photon leakage from the cavity, where the interplay between the atomic dynamics and the cavity field gives rise to intriguing nonlinear phenomena. We explore the full quantum mechanical treatment beyond the mean-field formalism, and investigate the correspondence between the quantum and the mean-field treatment. The quantum treatment is carried out by solving the Master equation for the total density operator, from which we can derive various quantities of interest, such as the cavity photon statistics, the degree of entanglement between the atom and cavity field. These two different approaches provide a deeper understanding to this intriguing system.

This Section is organized as follows. In Sec. 4.2.1, we show that the mean-field approach results in a phase diagram characterizing nonlinear band structures. In Sec. 4.2.2, we develop the full quantum mechanical formalism to the physical system of interest. In Sec. 4.2.3, we discuss the intimate correspondence between these two approaches.

4.2.1 Model Setup and Mean-Field Approach

As shown schematically in Fig. 4.7, we consider a single atom being confined by a single-mode unidirectional ring cavity, whose cavity mode together with an additional coherent laser beam form a pair of Raman beams that induces transition between two hyperfine atomic ground states denoted as $|\uparrow\rangle$ and $|\downarrow\rangle$, while transferring recoil momentum $\pm 2\hbar q_r \hat{z}$ to the atom. The ring cavity has a resonant frequency of ω_c, decay rate κ, and is pumped by an external laser field with frequency ω_p and pumping rate ε_p. The Hamiltonian under the rotating wave approximation can be written as,

$$\begin{aligned} \mathcal{H}_{\text{eff}} &= \sum_{\sigma=\uparrow,\downarrow} \int dz \left[\hat{\psi}_\sigma^\dagger(z) \left(\frac{k^2 + 2\alpha_\sigma q_r k}{2m} + \alpha_\sigma \delta \right) \hat{\psi}_\sigma(z) \right] \\ &+ \frac{\Omega}{2} \int dz \left[\hat{\psi}_\uparrow^\dagger(z) \hat{\psi}_\downarrow(z) \hat{c} + h.c. \right] \\ &+ i\varepsilon_p (\hat{c}^\dagger - \hat{c}) - \delta_c \hat{c}^\dagger \hat{c} \,, \end{aligned} \tag{4.52}$$

where, for simplicity, we only consider the atomic COM motion along the z-axis, which is the direction of the photon recoil. In Hamiltonian (4.52), k is the atomic COM quasi-momentum (we take $\hbar = 1$) along the z-axis, $\hat{c}$ is the cavity annihilation operator, $\hat{\psi}_\sigma(z)$ ($\sigma = \uparrow, \downarrow$) is the atomic operator, $\alpha_{\uparrow,\downarrow} = \pm 1$, 2δ represents the two-photon Raman detuning, $\delta_c = \omega_p - \omega_c$ is the cavity-pump detuning, and Ω denotes the atom-cavity coupling strength (or more specifically, the Raman coupling strength per cavity photon). Finally we will treat the cavity decay phenomenologically, which amounts to adding a non-Hermitian term $-i\kappa \hat{c}^\dagger \hat{c}$ in the above effective Hamiltonian. Note that for a quasi-momentum k, the real momentum for an atom is spin-dependent: it is $k + q_r$ for $|\uparrow\rangle$ state and $k - q_r$ for $|\downarrow\rangle$ state.

From Hamiltonian (4.52), one can easily obtain the Heisenberg equations of motion for both atomic and cavity fields. In this work, we only consider a single atom inside the cavity. Hence we rewrite the atomic field operators as first quantization wave

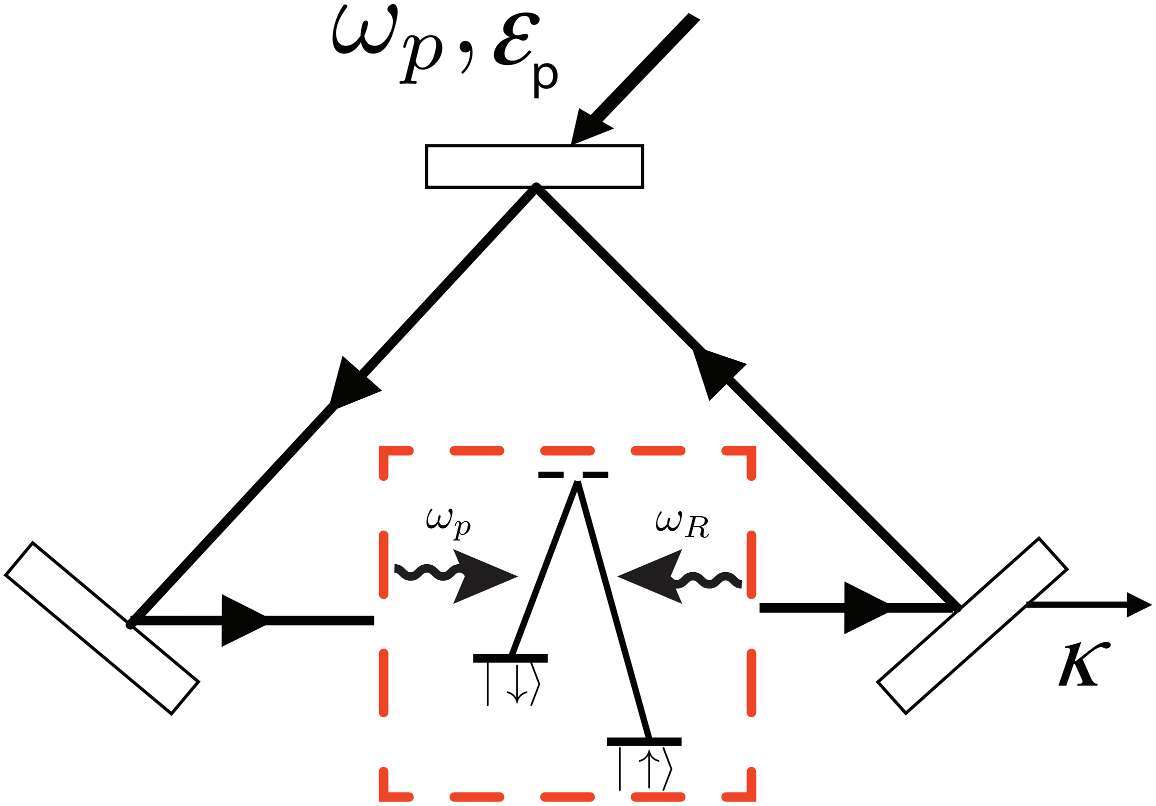

Figure 4.7 : Schematic diagram of the cavity-assisted spin-orbit coupled system. Inside the red dashed box, we show the level diagram of the atom and the light field configuration where ω_p represents the cavity field and ω_R is an external coherent laser beam. ε_p and κ are the cavity pumping rate and decay rate, respectively.

functions $\hat{\psi}_\sigma(z) \to \psi_\sigma(z)$. Assuming spatial homogeneity, we further take the plane-wave wave function for the atomic modes $\psi_\sigma(z) = e^{ikz}\varphi_\sigma$ with the normalization condition $|\varphi_\uparrow|^2+|\varphi_\downarrow|^2 = 1$. To proceed further, we adopt the mean-field approximation by replacing the photon field operators by its respective expectation value: $\hat{c} \to c \equiv \langle \hat{c} \rangle$. The validity of this mean-field approximation lies on two assumptions: (1) the cavity field can be described as a coherent state; (2) the atomic field and the cavity field have negligible entanglement. We shall come back to these two assumptions later when we compare the mean-field results with results obtained from the beyond-mean-field quantum Master equation.

Within the mean-field formalism, the steady-state solution for the photon field is obtained by taking the time derivative of the photon field to be zero, from which we obtain:

$$c = \frac{\varepsilon_p - i\frac{\Omega}{2}\varphi_\downarrow^*\varphi_\uparrow}{\kappa - i\delta_c}. \tag{4.53}$$

Inserting this into the equations for atomic fields, we obtain the coupled nonlinear time-dependent equations for the two spin components as,

$$\begin{aligned} i\dot{\varphi}_\uparrow &= \left(\frac{k^2}{2m} + q_r k + \delta\right)\varphi_\uparrow + \frac{\Omega_{\text{eff}}}{2}\,\varphi_\downarrow\,, & (4.54)\\ i\dot{\varphi}_\downarrow &= \left(\frac{k^2}{2m} - q_r k - \delta\right)\varphi_\downarrow + \frac{\Omega_{\text{eff}}^*}{2}\,\varphi_\uparrow\,. & (4.55)\end{aligned}$$

where $\Omega_{\text{eff}} \equiv \Omega c = \Omega\frac{\varepsilon_p - i\frac{\Omega}{2}\varphi_\downarrow^*\varphi_\uparrow}{\kappa - i\delta_c}$ is the effective Raman coupling strength between two atomic states. The fact that Ω_{eff} depends on the atomic field itself is a manifestation of the non-linearity arising from the atomic back-action to the cavity field.

For a given atomic quasi-momentum k, we define eigenstate and eigenenergy as the solution of the time-independent version of Eqs. (4.54) and (4.55), by replacing $i(\partial/\partial t)$ with $\epsilon(k)$. After some lengthy but straightforward algebra, we find that $\epsilon(k)$

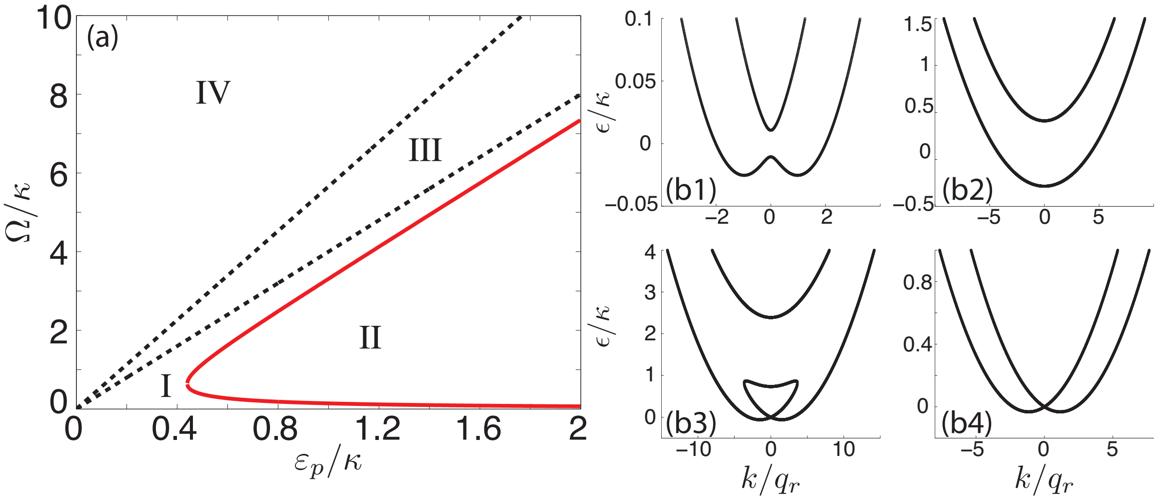

Figure 4.8 : Single particle eigen-energy spectrum "phase diagram". The dispersion curve is generally catagorized by four regions, represented from I to IV in (a). From (b1) to (b4), we fix $\varepsilon_p = \kappa$. In region I, the dispersion has double minima as shown in (b1) with $\Omega = 0.03\kappa$; region II is enclosed by the red solid curve in (a) and we show the typical point in (b2) ($\Omega = \kappa$) where only single minimum exisits in the lower helicity branch; region III is enclosed by the black dashed lines in (a) and it is a region where loop structure emerges, as in (b3) with $\Omega = 5\kappa$; finally, in region IV we recover the double minimum dispersion although it's different from region I by closing the gap at $k = 0$, as in (b4) with $\Omega = 8\kappa$. Throughout this Section we fix $\delta_c = \kappa$ and $\delta = 0$, and adopt a dimensionless unit system with $\hbar = m = \kappa = 1$. A typical value for κ is $2\pi \times 1$ MHz, and we choose $q_r = 0.22$ in our dimensionless units (based on a realistic experimental parameter estimate).

obeys a quartic equation in the form of

$$4\epsilon^4 + B\epsilon^3 + C\epsilon^2 + D\epsilon + E = 0\,. \tag{4.56}$$

We can gain some insights about the general structure of the dispersion relation $\epsilon(k)$, e.g. the degeneracy condition and the appearance and disappearance of the loop. In the case of vanishing two-photon detuning (i.e., $\delta = 0$), simple analysis shows that there should be a total of four regimes, as shown in Fig. 4.8(a). In region I, the two dispersion branches are gapped, and the lower branch has a double degenerate minima, as shown in Fig. 4.8(b1). This dispersion curve structure is very similar to the case when both Raman beams are provided by classical coherent laser fields (we shall refer to this as the "classical case") and the Raman coupling strength is small. In region II, as shown in Fig. 4.8(b2), the two dispersion branches are still gapped, but the lower branch has a single minimum. This is similar to the classical case with a large Raman coupling strength. Regions III and IV do not have analogs in the classical case. Region III features a loop structure, as shown in Fig. 4.8(b3), whereas in Region IV, the loop dissolves but the two dispersion branches becomes gapless at $k = 0$, as shown in Fig. 4.8(b4). In the looped region, the quartic equation (4.56) yields four real roots. It can be shown that this requires the coupling strength Ω to satisfy

$$\Omega_c^{(1)} \equiv 4\varepsilon_p \leq \Omega \leq 4\varepsilon_p\sqrt{1+(\delta_c/\kappa)^2} \equiv \Omega_c^{(2)} .$$

The two dashed lines in Fig. 4.8(a) represent the two critical values $\Omega_c^{(1)}$ and $\Omega_c^{(2)}$, respectively.

It is instructive to examine how the effective Raman coupling strength Ω_{eff} behaves as a function of Ω. In Fig. 4.9(a), we plot $|\Omega_{\text{eff}}|$ for the lowest dispersion branch as a function of Ω for different k values. Note that $|\Omega_{\text{eff}}|^2 = \Omega^2 n_{\text{photon}}$ where $n_{\text{photon}} = |c|^2$ is the steady-state cavity photon number. A few remarks can be made based on this plot. First, the fact that Ω_{eff} is different for different k clearly shows the influence of the atomic COM motion on both the atomic internal dynamics and the cavity photon number. Second, $|\Omega_{\text{eff}}|$ is not a monotonous function of Ω. For given k, $|\Omega_{\text{eff}}|$ increases with Ω linearly for small Ω. This can be intuitively understood as follows. At such weak atom-photon coupling, the back-action from the atom to the cavity photon is negligible. The number of cavity photons n_{photon} is roughly given by $n_{\text{photon}} \approx n_0 = \left|\frac{\varepsilon_p}{\kappa - i\delta_c}\right|^2 = \frac{\varepsilon_p^2}{\kappa^2+\delta_c^2}$, where n_0 is the number of cavity photons when

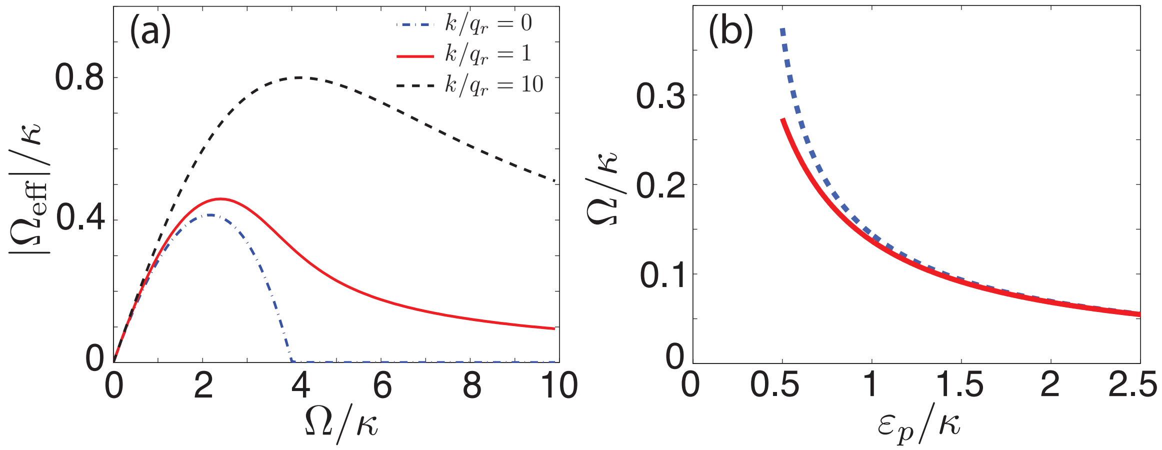

Figure 4.9 : (a) Effective Raman coupling $|\Omega_{\text{eff}}|$ is plotted as a function of atom-photon coupling strength Ω for different k values, $0, q_r, 10q_r$ for blue dash-dot, red solid and black dashed lines. We observe that $|\Omega_{\text{eff}}|$ does not monotonically increases with Ω but rather peaks at an intermediate value, then approaches zero in the large Ω limit. Figure (b) shows a comparison between critical boundary of region I and II (red solid curve) and the analytical result (blue dashed line) given in Eq. (4.57). At large ε_p limit, the two results match asymptotically well.

the atom is absent. As a result, we have $|\Omega_{\text{eff}}| \approx \Omega\sqrt{n_0}$ which is independent of the atomic quasi-momentum k. On the other limit, when Ω is very large, the strong atom-cavity coupling strength significantly detunes the cavity away from resonance and the cavity photon number n_{photon}, and hence $|\Omega_{\text{eff}}|$, decreases as a function of Ω. Such a non-monotonous behavior of Ω_{eff} is a unique feature of the cavity system and a direct manifestation of the non-linearity of the system arising from the back-action of the atom on the cavity photon.

From the above analysis, it should also become clear that when the effect of the back-action is weak (which occurs when Ω is small and/or ε_p is large), we should recover the properties of the classical case. In particular, in the classical case, the lower dispersion branch change from two degenerate minima to a single minimum when the Raman coupling strength exceeds a critical value. Using our notation, this occurs when $|\Omega_{\text{eff}}|$ exceeds the critical value $4E_r$ where $E_r = q_r^2/(2m)$ is the photon recoil energy. For weak atom-cavity coupling, $|\Omega_{\text{eff}}| = \Omega\sqrt{n_0} = \Omega\frac{\varepsilon_p}{\sqrt{\kappa^2+\delta_c^2}}$. Hence the critical value of Ω is given by

$$\Omega = 4E_r\frac{\sqrt{\kappa^2+\delta_c^2}}{\varepsilon_p}\,. \tag{4.57}$$

In Fig. 4.9(b), we plot this critical value (blue dashed line) as a function of cavity pump rate ε_p and compare it with the numerically determined lower boundary (red solid line) between region I and II of Fig. 4.8(a). The two curves overlap with each other when ε_p increases. Therefore, as we have expected, in the limit of weak atom-cavity coupling and strong cavity pumping, we fully recover the classical case where the SOC is induced by two classical laser beams.

4.2.2 Master Equation Approach

The above discussion is based on the mean-field approach where the cavity field is replaced by a c-number that represents the photon amplitude. This mean-field treatment relies on two implicit assumptions: (1) the atom-photon correlation is negligible, and (2) the photon field can be well approximated by a coherent state. In order to examine the validity of these assumption, and hence the validity of the mean-field approximation, we now turn to a full quantum treatment based on the Master equation:

$$\dot{\rho} = \frac{1}{i\hbar}[\mathcal{H}_{\text{eff}}, \rho] + \mathcal{L}[\rho]\,. \tag{4.58}$$

Here ρ is the total density operator of the coupled atom-cavity system, the effective Hamiltonian $\mathcal{H}_{\text{eff}}$ is the same as in Eq. (4.52). The dissipation arising from cavity decay is modeled by the Liouvillean term in the standard form of Lindblad superoperator,

$$\mathcal{L}[\rho] = \kappa(2c\rho\hat{c}^\dagger - \hat{c}^\dagger\hat{c}\rho - \rho\hat{c}^\dagger\hat{c})\,. \tag{4.59}$$

Again, due to spatial homogeneity, we decouple momentum eigenstates by taking the plane-wave ansatz for the atomic modes as $\hat{\psi}_\sigma(z) = e^{ikz}\hat{\psi}_\sigma$. As there is no coupling between atomic operators with different k, we can work in the subspace for a fixed value of k. Here we explicitly write the commutator in Eq. (4.58), for a given atomic quasi-momentum k, as,

$$\begin{aligned}
[\mathcal{H}_{\text{eff}}(k), \rho] \;\; = \;\; & \left(\frac{k^2}{2m} + \frac{q_r k}{m} + \delta\right)\left(\hat{\psi}_\uparrow^\dagger\hat{\psi}_\uparrow\rho - \rho\hat{\psi}_\uparrow^\dagger\hat{\psi}_\uparrow\right) \\
& + \left(\frac{k^2}{2m} - \frac{q_r k}{m} - \delta\right)\left(\hat{\psi}_\downarrow^\dagger\hat{\psi}_\downarrow\rho - \rho\hat{\psi}_\downarrow^\dagger\hat{\psi}_\downarrow\right) \\
& + \frac{\Omega}{2}\left(\hat{\psi}_\uparrow^\dagger\hat{\psi}_\downarrow\hat{c}\rho + \hat{c}^\dagger\hat{\psi}_\downarrow^\dagger\hat{\psi}_\uparrow\rho - \rho\hat{\psi}_\uparrow^\dagger\hat{\psi}_\downarrow c - \rho\hat{c}^\dagger\hat{\psi}_\downarrow^\dagger\hat{\psi}_\uparrow\right) \\
& + i\varepsilon_p\left(\hat{c}^\dagger\rho - \hat{c}\rho - \rho\hat{c}^\dagger + \rho\hat{c}\right) - \delta_c\left(\hat{c}^\dagger\hat{c}\rho - \rho\hat{c}^\dagger\hat{c}\right)\,.
\end{aligned} \tag{4.60}$$

Note that if the photon recoil $q_r = 0$, which occurs when the cavity mode and the external laser beams are co-propagating, the COM kinetic energy terms $k^2/(2m)$ can be gauged away after a simple gauge transformation. Our model is then reduced to the J-C model and the atomic COM motion does not play a role. To solve the Master equation (4.58), we choose our basis states as direct product states of photon Fock state $|n\rangle$ and atomic internal state $|\sigma =\uparrow,\downarrow\rangle$: $|n;\sigma\rangle \equiv |n\rangle \otimes |\sigma\rangle$, where non-negative integer n denotes cavity photon number. Our goal is to calculate the entire matrix elements of the density operator under this set of basis states, denoted by $\langle m;\sigma|\rho|n;\sigma'\rangle \equiv \rho_{mn}^{\sigma\sigma'}$. We found the governing equation for the matrix element can be written as,

$$\begin{aligned}\frac{d}{dt}\rho_{mn}^{\sigma\sigma'} &= -i\left(\frac{k^2}{2m}+\frac{q_r k}{m}+\delta\right)\left(\delta_{\sigma\uparrow}-\delta_{\sigma'\uparrow}\right)\rho_{mn}^{\sigma\sigma'} - i\left(\frac{k^2}{2m}-\frac{q_r k}{m}-\delta\right)\left(\delta_{\sigma\downarrow}-\delta_{\sigma'\downarrow}\right)\rho_{mn}^{\sigma\sigma'} \\ &+ \frac{\Omega}{2i}(\delta_{\sigma\uparrow}\sqrt{m+1}\rho_{m+1n}^{\bar{\sigma}\sigma'}+\delta_{\sigma\downarrow}\sqrt{m}\rho_{m-1n}^{\bar{\sigma}\sigma'}-\delta_{\sigma'\uparrow}\sqrt{n+1}\rho_{mn+1}^{\sigma\bar{\sigma}'}-\delta_{\sigma'\downarrow}\sqrt{n}\rho_{mn-1}^{\sigma\bar{\sigma}'}) \\ &+ \varepsilon_p\left(\sqrt{m}\rho_{m-1n}^{\sigma\sigma'}-\sqrt{m+1}\rho_{m+1n}^{\sigma\sigma'}+\sqrt{n}\rho_{mn-1}^{\sigma\sigma'}-\sqrt{n+1}\rho_{mn+1}^{\sigma\sigma'}\right) \\ &+ i\delta_c\left(m-n\right)\rho_{mn}^{\sigma\sigma'}+\kappa\left(2\sqrt{m+1}\sqrt{n+1}\rho_{m+1n+1}^{\sigma\sigma'}-(m+n)\rho_{mn}^{\sigma\sigma'}\right), \qquad (4.61)\end{aligned}$$

where $\bar{\sigma}$ represents the flip-spin value, i.e. $\bar{\uparrow}=\downarrow$ and $\bar{\downarrow}=\uparrow$.

With Eq. (4.61), we can study the dynamical evolution of the density operator ρ for a given initial state. Obviously, we need to introduce a sufficiently large photon number cutoff. Once we obtain the density operator, all relevant physical quantities can be readily calculated. An example is given in Fig. 4.10, where we show the time evolution of the cavity photon number $n = \mathrm{Tr}[\rho\hat{n}] = \mathrm{Tr}[\rho\hat{c}^\dagger\hat{c}]$ for the initial state $|0;\uparrow\rangle$. The three different curves in Fig. 4.10 correspond to different atomic quasi-momentum k.

As evidenced in Fig. 4.10, due to the presence of cavity decay, a steady state will eventually be reached. Let us now focus on the properties of the steady state. The steady-state density operator matrix elements can be obtained by equating the RHS of Eq. (4.61) to zero. The red dashed lines in Fig. 4.11(a)-(c) represent the steady-state photon number as functions of atomic quasi-momentum k. The horizontal arrows in the plot represent the cavity photon number by setting $q_r = 0$, in which case our model reduces to the J-C model and all physical quantities become k-independent.

To have a better understanding of the photon statistics, we study the steady-state photon number fluctuation. Specifically, we calculate the normalized photon number fluctuation defined as

$$\Delta_n = \frac{\langle(\Delta n)^2\rangle}{\langle\hat{n}\rangle} = \frac{\langle\hat{n}^2\rangle - \langle\hat{n}\rangle^2}{\langle n\rangle}\,,$$

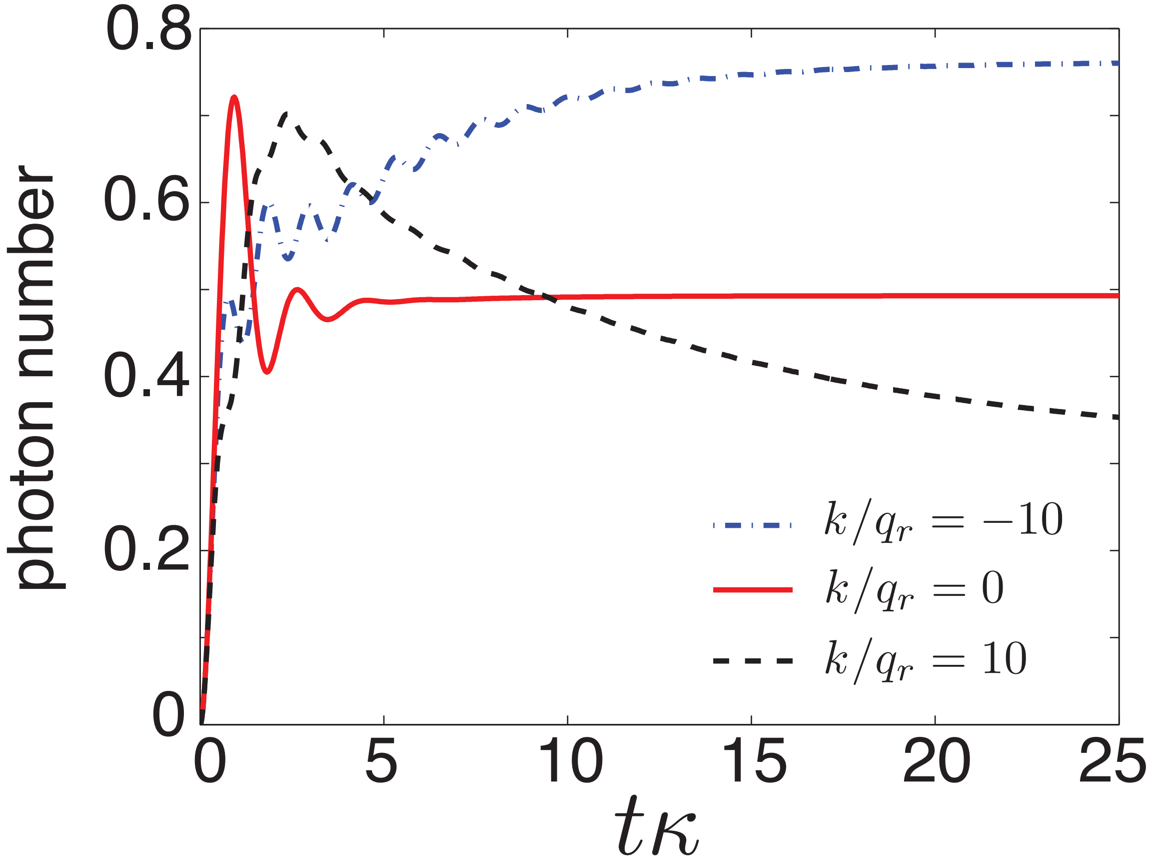

Figure 4.10 : Time evolution of cavity photon number. The initial state is given by $|0;\uparrow\rangle$ and we consider the same parameter as in Fig. 4.11(a) with $k/q_r = -10$, 0, 10. The steady-state values, obtained in the long time limit as shown here, correspond to red dashed lines at corresponding k values in Fig. 4.11(a).

where the expectation values of the operators are obtained with the help of the steady-state density operator. For a coherent cavity field, the photon fluctuation is Poissonian and we have $\Delta_n = 1$. The solid curves in Fig. 4.11(d)-(f) represent Δ_n (left vertical axis) as functions of k, and the horizontal arrows pointing to left give the values of Δ_n from the J-C model by setting $q_r = 0$. For the parameters we have used, we note that the J-C model always predicts a super-Poissonian photon statistics, whereas our model gives super-Poissonian photon statistics only for small atomic quasi-momentum, but Poissonian statistics as $k/q_r \to \pm\infty$.

Last but not least, to characterize the correlation between the atom and the cavity field, we investigate the so-called negativity which measures the degree of entanglement for a mixed state system. The negativity is defined as $\mathcal{N}(\rho) = (||\rho^{T_A}||_1 - 1)/2$, where ρ^{T_A} is the partial transpose of the density operator with respect to either the atom subsystem or the cavity subsystem, and $||\rho^{T_A}||_1$ denotes its trace norm with the definition $||\hat{A}||_1 \equiv \mathrm{Tr}[\sqrt{\hat{A}^\dagger \hat{A}}]$. A negativity of zero indicates that the two subsystems (the atom and the cavity, in our case) are not entangled, whereas a positive negativity means that finite degree of entanglement is present. The dashed curves in Fig. 4.11(d)-(f) represent the negativity (right vertical axis) in the steady state as functions of k, and the horizontal arrows pointing to right give the values of the negativity from the J-C model by setting $q_r = 0$. One can observe that for the chosen parameters, the J-C model always predicts a finite degree of entanglement between the atom and the cavity field. By contrast, the degree of entanglement in our model weakens when $k/q_r \to \pm\infty$.

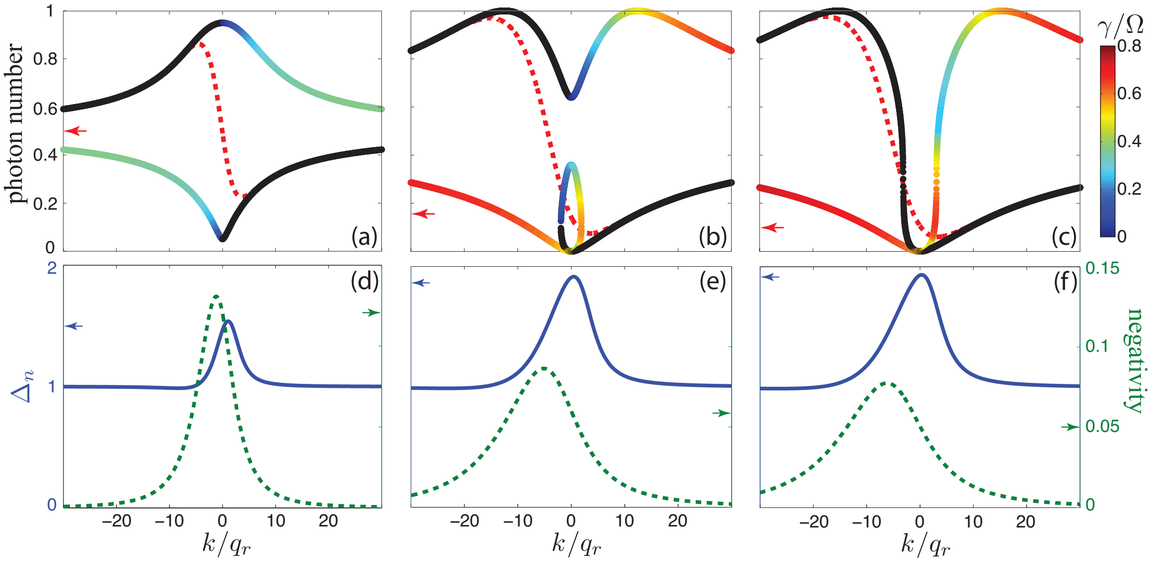

Figure 4.11 : (a)∼(c) Photon number obtained from the mean-field approach (solid curves) and from quantum mechanical Master equation approach (red dashed curves). From (a) to (c), $\Omega = 3\kappa$, 5.6κ, 6κ. The color on the solid curves represents the normalized decay rate γ/Ω of unstable mean-field states. The black color represents stable mean-field states. We have used $\varepsilon_p = \kappa$, and other parameters are the same as in Fig. 4.8. (d)∼(f) Corresponding photon number fluctuation (blue solid curve) and negativity (green dashed line) obtained from the quantum approach. The parameters used here are the same in (a)∼(c), respectively. The horizontal arrows indicate results from the J-C model by taking $q_r = 0$.

4.2.3 Master Equation versus Mean-Field Results

In the previous two sections, we have presented two different methods for studying the system. We are now in a position to discuss their connections.

In Fig. 4.11(a)-(c), in addition to the steady-state photon number obtained from the quantum treatment (dashed curves), we also plot the photon number $n_{\mathrm{photon}} = |c|^2$ obtained from the mean-field approach (solid curves), with c given in Eq. (4.53). In the quantum treatment, the steady-state density matrix is obtained by solving a set of linear equations. For a given k, the solution is unique. Hence we only get one steady-state photon number for a given atomic quasi-momentum. On the other hand, the mean-field treatment allows multiple steady-state solutions corresponding to different real roots of the quartic equation Eq. (4.56). Hence a single k value is associated with more than one steady-state photon number. However, due to the non-linearity intrinsic in the mean-field method, not all steady-states are dynamically stable. A straightforward stability analysis allows us to quantify the dynamical stability of the mean-field states. The stability information of the mean-field states are encoded as the color value in the solid curves. Those stable states are represented by black color, while any color other than black indicates an unstable state, and the color value represents the decay rate (see the colorbar) of the corresponding state. From Fig. 4.11(a)-(c), we clearly see that at large atomic quasi-momentum $k/q_r \to \pm\infty$, the Master equation result overlaps with the stable mean-field branch; while at small $|k|$, the quantum result deviates significantly away from the mean-field solution.

The agreement for large $|k|$ and the discrepancy at small $|k|$ are both consistent with the results of the negativity and photon number fluctuations as presented in Fig. 4.11(d)-(f): At large $|k|$, the negativity is small (i.e., atom-cavity entanglement is weak) and the photon number fluctuation tends to Poissonian (i.e., the photon field is well approximated by a coherent state), this is exactly the regime where we expect the mean-field approximation is valid. By contrast, for small $|k|$, the quantum calculation indicates that there is non-negligible entanglement between the atom and the cavity field, and the cavity field itself cannot be assumed as a coherent state. Hence the mean-field assumption is no longer valid.

The reason why mean-field approximation only works for large $|k|$ is actually rather simple. Consider a Raman transition process where the atom jumps from $|\uparrow\rangle$ to $|\downarrow\rangle$. The quasi-momentum k does not change during this process, however the real momentum changes from $k + q_r$ to $k - q_r$. Therefore the effective two-photon Raman detuning is not just 2δ, but $2\delta + 2q_r k/m$, where the additional term comes from the difference of the kinetic energies for different pseudo-spin state $|\sigma\rangle$. In other words, the SOC renders the two-photon detuning momentum-dependent. In the examples we presented in this work, we have taken $\delta = 0$. Hence the Raman transition is only near-resonant for small $|k|$, and becomes far off-resonant for large $|k|$. Therefore, for large $|k|$, the atom-photon coupling, and hence the atomic back-action to cavity, are weak. This explains why the mean-field assumption becomes valid in this regime.

Chapter 5

Summary

In summary, we have presented five innovative research projects in the research field of ”synthetic spin-orbit coupling in cold atoms”, based on a variety of novel quantum systems, which includes the harmonically trapped system presented in Chapter 2, the Bose-Fermi mixture in Sec. 3.1, the Bose-Bose mixture in Sec. 3.2, the quantum optical system in Sec. 4.1, and the dissipative optical cavity in Sec. 4.2.

In Chapter 2, we have systematically investigated the single-particle and two-body ground states of Raman-induced spin-orbit coupled ultracold atoms in a 1D harmonic trap. In the absence of the Raman coupling, all single-particle eigenstates are two-fold degenerate. As the Raman coupling strength increases, the degeneracy of higher energy eigenstates start to be lifted first, and eventually at a critical coupling strength, the ground state (and hence all energy eigenstates) becomes non-degenerate. The single-particle spectrum and wave functions help us to understand the two-body properties of the system for both bosons and fermions. For the two-boson case, we point out three phases distinguished by the behaviors of the degeneracy, density-density correlation functions, and spin density profiles. Then we identify a regime where the two atoms in the ground state are entangled and characterized by stripes in density-density correlations. This regime corresponds to the regime of the exotic stripe phase in the mean-field many-body limit. This Chapter therefore establishes a connection among one-, few- and many-body physics of trapped atomic systems with spin-orbit coupling.

In Section 3.1, we have investigated a system of Bose-Fermi spinor mixtures. The bosons form a condensate that subjected to the Raman-induced spin-orbit coupling, while the fermions are not coupled to the Raman lasers, but interact with the bosons via the density-density and/or spin-exchange interaction. We show that the spin-exchange interaction makes the fermions experiencing an effective spin-orbit coupling, without suffering Raman-induced heating. This could pave a new way towards the first realization of spin-orbit coupled fermionic superfluids, which can be made to be topological with a proper choice of parameters. The interplay between the bosons and fermions also has an interesting effect on the former: the Bose-Fermi interaction favors the condensate to be in the stripe phase, with an interaction-dependent spatial modulation period. With realistic parameters, the spatial modulation period can be as large as several microns, making the stripe phase readily observable with the *in situ* imaging technique. This provides a significant advantage in both the realization and the observation of the stripe phase. This providing a new and unique platform to explore the physics of spin-orbit coupling.

In Section 3.2, we have presented a study of a mixture of two species of spin-1/2 Bose condensates, with only one of the species subjected to a pair of Raman laser beams which induces spin-orbit coupling in that species. Through the interspecies spin-exchange interaction, however, the other species also exhibits spin-orbit coupling. With many control parameters, such as the relative atomic numbers, interaction strengths, etc., the mixture system displays a very rich phase diagram, and many of the phases do not exist in a single-species system. Similar to the Bose-Fermi case discussed in Sec. 3.2, the Bose-Bose mixture provides a viable way of achieving spin-orbit coupling in bosonic species that suffer from severe Raman-induced heating.

In Section 4.1, we have studied the Raman spin-orbit coupling induced by one cavity photon field and one classical Raman laser beam, where all three degrees of freedom including the atomic internal pseudo-spin, the atomic external center-of-mass motion, and the cavity photon field are coupled and treated self-consistently. For the single-atom case, we show that the spin-orbit coupling stabilizes the sector which contains no photons. Furthermore, the spin-orbit coupling combined with a trapping potential gives rise to rich spin dynamics. For the many-atom case in thermodynamic limit, we focused on the physics of the Dicke superradiance phase transition. In comparison to the Tavis-Cummings model where the atomic center-of-mass motion is neglected, the spin-orbit coupling modifies the phase transition boundary by increasing the critical atom-cavity coupling strength at which the system becomes superradiant. Furthermore, the non-monotonic behavior of the critical coupling strength can lead to the reentrant of the non-superradiant normal phase as the temperature varies.

In Section 4.2, we have studied spin-orbit coupled cold atoms inside a dissipative ring cavity system, through adding dissipative terms into the model shown in Sec. 4.1) and employing both the mean-field theory and the full quantum mechanical Master equation approach. By treating both light and atom on equal footing and seeking the self-consistent solution in both approaches, we have found: (1) cavity-assisted spin-orbit coupling dramatically modifies atomic dispersion relation, (2) intriguing dynamical instabilities exist in the system, (3) atom's back-action onto cavity field also leads to non-trivial atom-photon coupling that is fundamentally different from either the system with classical-laser induced spin-orbit coupling in the absence of the cavity or the Jaynes-Cummings model where the atomic center-of-mass motion is neglected. We have also explored correspondence and discussed the connection between the mean-field and the quantum approaches. The two distinctively different approaches provide us with a deeper understanding and complementary insights into this system.

Bibliography

[1] Y. K. Kato, R. C. Myers, A. C. Gossard, and D. D. Awschalom, "Observation of the spin hall effect in semiconductors," *Science*, vol. 306, 2004.

[2] B. A. Bernevig, T. L. Hughes, and S.-C. Zhang, "Quantum spin hall effect and topological phase transition in hgte quantum wells," *Science*, vol. 314, 2006.

[3] Y.-J. Lin, K. Jimenez-Garcia, and I. B. Spielman, "Spin-orbit-coupled bose-einstein condensates," *Nature*, vol. 471, 2011.

[4] Y. Li, L. P. Pitaevskii, and S. Stringari, "Quantum tricriticality and phase transitions in spin-orbit coupled bose-einstein condensates," *Physical Review Letters*, vol. 108, 2012.

[5] J.-R. Li, J. Lee, W. Huang, S. Burchesky, B. Shteynas, F. C. Top, A. O. Jamison, and W. Ketterle, "A stripe phase with supersolid properties in spin-orbit-coupled bose-einstein condensates," *Nature*, vol. 543, 2017.

[6] T. M. Bersano, J. Hou, S. Mossman, V. Gokhroo, X.-W. Luo, K. Sun, C. Zhang, and P. Engels, "Experimental realization of a long-lived striped bose-einstein condensate induced by momentum-space hopping," *Phsical Review A*, vol. 99, 2019.

[7] Z. Wu, L. Zhang, W. Sun, X.-T. Xu, B.-Z. Wang, S.-C. Ji, Y. Deng, S. Chen, X.-J. Liu, and J.-W. Pan, "Realization of two-dimensional spin-orbit coupling

for bose-einstein condensates," *Science*, vol. 354, 2016.

[8] S.-C. Ji, J.-Y. Zhang, L. Zhang, Z.-D. Du, W. Zheng, Y.-J. Deng, H. Zhai, S. Chen, and J.-W. Pan, "Experimental determination of the finite- temperature phase diagram of a spin-orbit coupled bose gas," *Nature Physics*, vol. 10, 2014.

[9] P. Wang, Z.-Q. Yu, Z. Fu, J. Miao, L. Huang, S. Chai, H. Zhai, and J. Zhang, "Spin-orbit coupled degenerate fermi gases," *Physical Review Letters*, vol. 109, 2012.

[10] L. W. Cheuk, A. T. Sommer, Z. Hadzibabic, T. Yefsah, W. S. Bakr, and M. W. Zwierlein, "Spin-injection spectroscopy of a spin-orbit coupled fermi gas," *Physical Review Letters*, vol. 109, 2012.

[11] N. Q. Burdick, Y. Tang, and B. L. Lev, "Long-lived spin-orbit-coupled degenerate dipolar fermi gas," *Physical Review X*, vol. 6, 2016.

[12] S. L. Bromley, S. Kolkowitz, T. Bothwell, D. Kedar, A. Safavi-Naini, M. L. Wall, C. Salomon, A. M. Rey, and J. Ye, "Dynamics of interacting fermions under spin-orbit coupling in an optical lattice clock," *Nature Physics*, vol. 14, 2018.

[13] H. Zhai, "Degenerate quantum gases with spin-orbit coupling: a review," *Reports on Progress in Physics*, vol. 78, 2015.

[14] N. Goldman, G. Juzeliunas, P. Ohberg, and I. B. Spielman, "Light-induced gauge fields for ultracold atoms," *Reports on Progress in Physics*, vol. 77, 2014.

[15] X.-J. Liu and H. Hu, "Topological superfluid in one-dimensional spin-orbit-coupled atomic fermi gases," *Physical Review A*, vol. 85, 2012.

[16] C. Gerry and P. Knight, “Introductory quantum optics,” *Cambridge*, 2004.

[17] C. Zhu, L. Dong, and H. Pu, “Harmonically trapped atoms with spin-orbit coupling,” *Journal of Physics B*, vol. 49, 2016.

[18] C. Zhu, L. Chen, H. Hu, X.-J. Liu, and H. Pu, “Spin-exchange-induced exotic superfluids in a bose-fermi spinor mixture,” *Physical Review A*, vol. 100, 2019.

[19] L. Chen, C. Zhu, Y. Zhang, and H. Pu, “Spin-exchange-induced spin-orbit coupling in a superfluid mixture,” *Physical Review A*, vol. 97, 2018.

[20] C. Zhu, L. Dong, and H. Pu, “Effects of spin-orbit coupling on jaynes-cummings and tavis-cummings models,” *Physical Review A*, vol. 94, 2016.

[21] L. Dong, C. Zhu, and H. Pu, “Photon-induced spin-orbit coupling in ultracold atoms inside optical cavity,” *Atoms*, vol. 3, 2015.

[22] L. Zhang, Y. Deng, and P. Zhang, “Scattering and effective interactions of ultracold atoms with spin-orbit coupling,” *Physical Review A*, vol. 87, 2013.

[23] L. Dong, L. Jiang, H. Hu, and H. Pu, “Finite-momentum dimer bound state in a spin-orbit-coupled fermi gas,” *Physical Review A*, vol. 87, 2013.

[24] Y. Kagan, E. L. Surkov, and G. V. Shlyapnikov, “Evolution of a bose gas in anisotropic time-dependent traps,” *Physical Review A*, vol. 55, 1997.

[25] Y. Castin and R. Dum, “Bose-einstein condensates in time dependent traps,” *Physical Review Letters*, vol. 77, 1996.

[26] S. kar and R. R. Parwani, “Can degenerate bound states occur in one-dimensional quantum mechanics?,” *Europhysics Letters*, vol. 80, 2007.

[27] Q. Guan and D. Blume, “Spin structure of harmonically trapped one-dimensional atoms with spin-orbit coupling,” *Physical Review A*, vol. 92, 2015.

[28] Q. Guan, X. Y. Yin, S. E. Gharashi, and D. Blume, “Energy spectrum of a harmonically trapped two-atom system with spin-orbit coupling,” *Journal of Physics B*, vol. 47, 2014.

[29] M. Olshanii, “Atomic scattering in the presence of an external confinement and a gas of impenetrable bosons,” *Physical Review Letters*, vol. 81, 1998.

[30] E. J. Mueller, T.-L. Ho, M. Ueda, and G. Baym, “Fragmentation of bose-einstein condensates,” *Physical Review A*, vol. 74, 2006.

[31] R. Kanamoto, H. Saito, and M. Ueda, “Quantum phase transition in one-dimensional bose-einstein condensates with attractive interactions,” *Physical Review A*, vol. 67, 2003.

[32] F. Serwane, G. Zürn, T. Lompe, T. B. Ottenstein, A. N. Wenz, and S. Jochim, “Deterministic preparation of a tunable few-fermion system,” *Science*, vol. 332, 2011.

[33] C. Wang, C. Gao, C.-M. Jian, and H. Zhai, “Spin-orbit coupled spinor bose-einstein condensates,” *Physical Review Letters*, vol. 105, 2010.

[34] T.-L. Ho and S. Zhang, “Bose-einstein condensates with spin-orbit interaction,” *Physical Review Letters*, vol. 107, 2011.

[35] Y. Li, G. I. Martone, L. P. Pitaevskii, and S. Stringari, “Superstripes and the excitation spectrum of a spin-orbit-coupled bose-einstein condensate,” *Physical Review Letters*, vol. 110, 2013.

[36] R. Sakamoto, Y. Ono, E. Arahata, and H. Mori, “Ground state of bose-fermi mixture with spin-orbit coupling,” *Journal of the Physical Society of Japan*, vol. 85, 2016.

[37] R. Sakamoto, Y. Ono, R. Hatsuda, K. Shiina, E. Arahata, and H. Mori, “Ground state of bosons in bose-fermi mixture with spin-orbit coupling,” *Journal of the Physical Society of Japan*, vol. 86, 2017.

[38] R. Liao, “Searching for supersolidity in ultracold atomic bose condensates with rashba spin-orbit coupling,” *Physical Review Letters*, vol. 120, 2018.

[39] B. Song, L. Zhang, C. He, T. F. J. Poon, E. Hajiyev, S. Zhang, X.-J. Liu, and G.-B. Jo, “Observation of symmetry-protected topological band with ultracold fermions,” *Science Advances*, vol. 4, 2018.

[40] G. Jotzu, M. Messer, R. Desbuquois, M. Lebrat, T. Uehlinger, D. Greif, and T. Esslinger, “Experimental realization of the topological haldane model with ultracold fermions,” *Nature*, vol. 515, (2014.

[41] Z. Meng, L. Huang, P. Peng, D. Li, L. Chen, Y. Xu, C. Zhang, P. Wang, and J. Zhang, “Experimental observation of a topological band gap opening in ultracold fermi gases with two-dimensional spin-orbit coupling,” *Physical Review Letters*, vol. 117, 2016.

[42] M. Gong, S. Tewari, and C. Zhang, “Bcs-bec crossover and topological phase transition in 3d spin-orbit coupled degenerate fermi gases,” *Physical Review Letters*, vol. 107, 2011.

[43] K. Sun, Z. Gu, H. Katsura, and S. D. Sarma, “Nearly flatbands with nontrivial topology,” *Physical Review Letters*, vol. 106, 2011.

[44] X.-J. Liu and H. Hu, "Topological fulde-ferrell superfluid in spin-orbit-coupled atomic fermi gases," *Physical Review A*, vol. 88, 2013.

[45] X.-J. Liu, "Momentum-resolved radio-frequency spectroscopy of ultracold atomic fermi gases in a spin-orbit-coupled lattice," *Physical Review A*, vol. 86, 2012.

[46] X.-J. Liu, Z.-X. Liu, and M. Cheng, "Manipulating topological edge spins in a one-dimensional optical lattice," *Physical Review Letters*, vol. 110, 2013.

[47] Y. Oreg, G. Refael, and F. v. Oppen, "Helical liquids and majorana bound states in quantum wires," *Physical Review Letters*, vol. 105, 2010.

[48] X.-J. Liu, "Impurity probe of topological superfluids in one-dimensional spin-orbit-coupled atomic fermi gases," *Physical Review A*, vol. 87, 2013.

[49] R. Wei and E. J. Mueller, "Majorana fermions in one-dimensional spin-orbit-coupled fermi gases," *Physical Review A*, vol. 86, 2012.

[50] X.-J. Liu and H. Hu, "Topological superfluid in one-dimensional spin-orbit-coupled atomic fermi gases," *Physical Review A*, vol. 85, 2012.

[51] S.-C. Ji, J.-Y. Zhang, L. Zhang, Z.-D. Du, W. Zheng, Y.-J. Deng, H. Zhai, S. Chen, and J.-W. Pan, "Experimental determination of the finite-temperature phase diagram of a spin-orbit coupled bose gas," *Nature Physics*, vol. 10, 2014.

[52] R. Wei and E. J. Mueller, "Magnetic-field dependence of raman coupling in alkali-metal atoms," *Physical Review A*, vol. 87, 2013.

[53] X. Li, B. Zhu, X. He, F. Wang, M. Guo, Z.-F. Xu, S. Zhang, and D. Wang, "Coherent heteronuclear spin dynamics in an ultracold spinor mixture," *Physical*

Review Letters, vol. 114, 2015.

[54] I. Ferrier-Barbut, M. Delehaye, S. Laurent, A. T. Grier, M. Pierce, B. S. Rem, F. Chevy, and C. Salomon, "A mixture of bose and fermi superfluids," *Science*, vol. 345, 2014.

[55] R. Roy, A. Green, R. Bowler, and S. Gupta, "Two-element mixture of bose and fermi superfluids," *Physical Review Letters*, vol. 118, 2017.

[56] X.-C. Yao, H.-Z. Chen, Y.-P. Wu, X.-P. Liu, X.-Q. Wang, X. Jiang, Y. Deng, Y.-A. Chen, and J.-W. Pan, "Observation of coupled vortex lattices in a mass-imbalance bose and fermi superfluid mixture," *Physical Review Letters*, vol. 117, 2016.

[57] J. M. McNamara, T. Jeltes, A. S. Tychkov, W. Hogervorst, and W. Vassen, "Degenerate bose-fermi mixture of metastable atoms," *Physical Review Letters*, vol. 97, 2006.

[58] W. Clark, B. M. Anderson, L. Feng, A. Gaj, K. Levin, and C. Chin, "Observation of density-dependent gauge fields in a bose-einstein condensate based on micromotion control in a shaken two-dimensional lattice," *Physical Review Letters*, vol. 121, 2018.

[59] F. Görg, K. Sandholzer, J. Minguzzi, R. Desbuquois, M. Messer, and T. Esslinger, "Realization of density-dependent peierls phases to engineer quantized gauge fields coupled to ultracold matter," *Nature Physics*, vol. 15, 2019.

[60] C. Schweizer, F. Grusdt, M. Berngruber, L. Barbiero, E. Demler, N. Goldman, I. Bloch, and M. Aidelsburger, "Floquet approach to z2 lattice gauge theories with ultracold atoms in optical lattices," *Nature Physics*, vol. 15, 2019.

[61] X.-J. Liu, K. T. Law, and T. K. Ng, “Realization of 2d spin-orbit interaction and exotic topological orders in cold atoms,” *Physical Review Letters*, vol. 112, 2014.

[62] J. Zak, “Berrys phase for energy bands in solids,” *Physical Review Letters*, vol. 62, 1989.

[63] M. Atala, M. Aidelsburger, J. T. Barreiro, D. Abanin, T. Kitagawa, E. Demler, and I. Bloch, “Direct measurement of the zak phase in topological bloch bands,” *Natuer Physics*, vol. 9, 2013.

[64] C. Pethick and H. Smith, “Bose-einstein condensation in dilute gases,” 2008.

[65] S. Haroche and J.-M. Raimond, “Exploring the quantum,” *Oxford*, 2006.

[66] F. Brennecke, T. Donner, S. Ritter, T. Bourdel, M. Kohl, and T. Esslinger, “Cavity qed with a bose-einstein condensate,” *Nature*, vol. 450, 2007.

[67] Y. Colombe, T. Steinmetz, G. Dubois, F. Linke, D. Hunger, and J. Reichel, “Strong atom-field coupling for bose-einstein condensates in an optical cavity on a chip,” *Nature*, vol. 450, 2007.

[68] S. Gupta, K. L. Moore, K. W. Murch, and D. M. Stamper-Kurn, “Cavity nonlinear optics at low photon numbers from collective atomic motion,” *Physical Review Letter*, vol. 99, 2007.

[69] T. Botter, D. W. C. Brooks, S. Schreppler, N. Brahms, and D. M. Stamper-Kurn, “Optical readout of the quantum collective motion of an array of atomic ensembles,” *Physical Review Letters*, vol. 110, 2013.

[70] J. M. Zhang, S. Cui, H. Jing, D. L. Zhou, and W. M. Liu, "Probing the quantum ground state of a spin-1 bose-einstein condensate with cavity transmission spectra," *Physical Review A*, vol. 80, 2009.

[71] L. Zhou, H. Pu, H. Y. Ling, and W. Zhang, "Cavity-mediated strong matter wave bistability in a spin-1 condensate," *Physical Review Letters*, vol. 103, 2009.

[72] Y. Dong, J. Ye, and H. Pu, "Multistability in an optomechanical system with a two-component bose-einstein condensate," *Physical Review A*, vol. 83, 2011.

[73] D. Rosseau, Q. Ha, and T. Byrnes, "Entanglement generation between two spinor bose-einstein condensates with cavity qed," *Physical Review A*, vol. 90, 2014.

[74] K. Baumann, C. Guerlin, F. Brennecke, and T. Esslinger, "Dicke quantum phase transition with a superfluid gas in an optical cavity," *Nature*, vol. 464, 1301.

[75] J. Klinder, H. Keler, M. Wolke, L. Mathey, and A. Hemmerich, "Dynamical phase transition in the open dicke model," *PNAS*, vol. 112, 2015.

[76] E. Jaynes and F. Cummings, "Comparison of quantum and semiclassical radiation theories with application to the beam maser," *Proceedings of the IEEE*, vol. 51, 1963.

[77] K. M. Birnbaum, A. Boca, R. Miller, A. D. Boozer, T. E. Northup, and H. J. Kimble, "Photon blockade in an optical cavity with one trapped atom," *Nature*, vol. 436, 2005.

[78] G. Rempe, H. Walther, and N. Klein, "Observation of quantum collapse and revival in a one-atom maser," *Physical Review Letter*, vol. 58, 1987.

[79] J. Ye, D. W. Vernooy, and H. J. Kimble, "Trapping of single atoms in cavity qed," *Physical Review Letters*, vol. 83, 1999.

[80] R. Miller, T. E. Northup, K. M. Birnbaum, A. Boca, A. D. Boozer, and H. J. Kimble, "Trapped atoms in cavity qed: coupling quantized light and matter," *Journal of Physics B*, vol. 38, 2005.

[81] P. W. H. Pinkse, T. Fischer, P. Maunz, and G. Rempe, "Trapping an atom with single photons," *Nature*, vol. 404, 2000.

[82] H. J. Kimble, "Strong interactions of single atoms and photons in cavity qed," *Physica Scripta*, vol. 76, 1998.

[83] H. Mabuchi, J. Ye, and H. J. Kimble, "Full observation of single-atom dynamics in cavity qed," *Applied Physics B*, vol. 68, 1999.

[84] J. M. Raimond, M. Brune, and S. Haroche, "Manipulating quantum entanglement with atoms and photons in a cavity," *Reviews of Modern Physics*, vol. 73, 2001.

[85] P. Maunz, T. Puppe, I. Schuster, N. Syassen, P. W. H. Pinkse, and G. Rempe, "Cavity cooling of a single atom," *Nature*, vol. 428, 2004.

[86] M. Wallquist, K. Hammerer, P. Zoller, C. Genes, M. Ludwig, F. Marquardt, P. Treutlein, J. Ye, and H. J. Kimble, "Single-atom cavity qed and optomicromechanics," *Physical Review A*, vol. 81, 2010.

[87] R. H. Dicke, “Coherence in spontaneous radiation processes,” *Physical Review*, vol. 99, 1954.

[88] M. Tavis and F. Cummings, “Exact solution for an n-moleculeradiation-field hamiltonian,” *Physical Review*, vol. 170, 1968.

[89] M. P. Baden, K. J. Arnold, A. L. Grimsmo, S. Parkins, and M. D. Barrett, “Realization of the dicke model using cavity-assisted raman transitions,” *Physical Review Letters*, vol. 113, 2014.

[90] C. Emary and T. Brandes, “Chaos and the quantum phase transition in the dicke model,” *Physical Review E*, vol. 67, 2003.

[91] L. Bao, F. Pan, J. Lu, and J. P. Draayer, “The critical point entanglement and chaos in the dicke model,” *Entropy*, vol. 17, 2015.

[92] O. Tsyplyatyev and D. Loss, “Dicke model: Entanglement as a finite size effect,” *Journal of Physics: Conference Series*, vol. 193, 2009.

[93] B. M. Garraway, “The dicke model in quantum optics: Dicke model revisited,” *Philosophical Transactions of the Royal Society A*, vol. 369, 2011.

[94] Y. K. Wang and H. F. T, “Phase transition in the dicke model of superradiance,” *Physical Review A*, vol. 7, 1973.

[95] K. Debnath and A. B. Bhattacherjee, “Non-equilibrium dynamics of an optomechanical dicke model,” *Communications in Theoretical Physics*, vol. 64, 2015.

[96] M. Buchhold, P. Strack, S. Sachdev, and S. Diehl, “Dicke-model quantum spin and photon glass in optical cavities: Nonequilibrium theory and experimental

signatures," *Physical Review A*, vol. 87, 2013.

[97] V. Galitski and I. B. Spielman, "Spin-orbit coupling in quantum gases," *Nature*, vol. 494, 2013.

[98] Y.-J. Lin, R. L. Compton, K. Jimnez-Garca, W. D. Phillips, J. V. Porto, and I. B. Spielman, "A synthetic electric force acting on neutral atoms," *Nature Physics*, vol. 7, 2011.

[99] W. Zheng, Z.-Q. Yu, X. Cui, and H. Zhai, "Properties of bose gases with the raman-induced spin-orbit coupling," *Journal of Physics B*, vol. 46, 2013.

[100] E. Brion, L. H. Pedersen, and K. Mlmer, "Adiabatic elimination in a lambda system," *Journal of Physics A*, vol. 40, 2007.

[101] T. D. Stanescu, B. Anderson, and V. Galitski, "Spin-orbit coupled bose-einstein condensates," *Physical Review A*, vol. 78, 2008.

[102] H. Hu, L. Jiang, X.-J. Liu, and H. Pu, "Probing anisotropic superfluidity in atomic fermi gases with rashba spin-orbit coupling," *Physical Review Letters*, vol. 107, 2011.

[103] G. I. Martone, Y. Li, and S. Stringari, "Approach for making visible and stable stripes in a spin-orbit-coupled bose-einstein superfluid," *Physical Review A*, vol. 90, 2014.

[104] L. Zhang, J.-Y. Zhang, S.-C. Ji, Z.-D. Du, H. Zhai, Y. Deng, S. Chen, P. Zhang, and J.-W. Pan, "Stability of excited dressed states with spin-orbit coupling," *Physical Review A*, vol. 87, 2013.

[105] H. Hu and S. Chen, “Mapping trapped atomic gas with spin-orbit coupling to quantum rabi-like model,” *arXiv*, vol. 1302.5933, 2013.

[106] Y. Deng, J. Cheng, H. Jing, and S. Yi, “Bose-einstein condensates with cavity-mediated spin-orbit coupling,” *Physical Review Letters*, vol. 112, 2014.

[107] B. Padhi and S. Ghosh, “Spin-orbit-coupled bose-einstein condensates in a cavity: Route to magnetic phases through cavity transmission,” *Physical Review A*, vol. 90, 2014.

[108] F. Mivehvar and D. L. Feder, “Enhanced stripe phases in spin-orbit-coupled bose-einstein condensates in ring cavities,” *Physical Review A*, vol. 92, 2015.

[109] F. Mivehvar and D. L. Feder, “Synthetic spin-orbit interactions and magnetic fields in ring-cavity qed,” *Physical Review A*, vol. 89, 2014.

[110] L. Dong, L. Zhou, B. Wu, B. Ramachandhran, and H. Pu, “Cavity-assisted dynamical spin-orbit coupling in cold atoms,” *Physical Review A*, vol. 89, 2014.